SAPIENZA
UNIVERSITÀ DI ROMA

SAPIENZA UNIVERSITY OF ROME
AND
UNIVERSITY OF ROME TOR VERGATA

PH.D. IN ASTRONOMY, ASTROPHYSICS AND SPACE SCIENCE

CYCLE XXX

X-ray spectral variability of Active Galactic Nuclei from XMM-Newton data

Roberto Serafinelli
A.Y. 2016/2017

Supervisor: Prof. Fausto Vagnetti

Coordinator: Prof. Pasquale Mazzotta

Deputy Coordinator: Prof. Roberto Capuzzo Dolcetta

The universe is big. It's vast and complicated and ridiculous. And sometimes, very rarely, impossible things just happen and we call them miracles

Contents

ABSTRACT

Active Galactic Nuclei (AGN) are extremely luminous ($L \sim 10^{42} - 10^{48}$ erg s^{-1}) objects, powered by the accretion of material onto a supermassive ($M_{\rm BH} \sim 10^6 - 10^9\,M_\odot$) black hole, usually located at the center of their host galaxy.
In this thesis I have mainly focused on the X-ray emission from this kind of sources, studying the variations of the shape of the spectrum in such band, in response to the variations of the X-ray flux, which is commonly referred to as "spectral variability".
The X-ray spectral variability of Active Galactic Nuclei typically follows a "softer when brighter" trend (e.g., Sobolewska & Papadakis, 2009; Connolly et al., 2016), which is believed to be originated by either intrinsic variations of the continuum of the spectra, or by the superposition of different spectral components, such as absorption or reflection, varying independently from each other, although it is also possible that both effects are responsible for the observed spectral variability trend.
In this thesis I analyzed the *Multi-Epoch XMM Serendipitous AGN Sample* (MEXSAS, Vagnetti et al., 2016), made up by more than 7 800 observations from 2 700 quasars, obtained by cross-matching the fifth release of the XMM-Newton Serendipitous Source Catalogue (3XMM-SSC, Rosen et al., 2016), with two quasar catalogues, SDSS-DR7Q (Schneider et al., 2010) and SDSS-DR12Q (Pâris et al., 2017). Following Trèvese & Vagnetti (2002), I quantified the spectral variability by using $\beta = -\Delta\Gamma/\Delta \log F$. I developed a technique (Serafinelli et al., 2017b) that is able to compute estimates of the photon index from approximate spectral fits, using the fluxes in the catalogue. I found an ensemble softer when brighter trend, extending therefore this result to quasars with a larger range of bolometric luminosity ($L_{\rm bol} \sim 10^{42} - 10^{47}$ erg/s) and redshift ($z \sim 0 - 5$), and the same result is found for eight single sources with significant $\Gamma - \log F$ correlations, extracted from the catalogue, although with different extent, plus one (PG 1114+445) discarded because of the presence of prominent absorption features in the soft X-ray ($0.5 - 2$ keV) band.
Moreover, using a newer version of MEXSAS, MEXSAS2 (Vagnetti et al., 2018), I found similar results for two different spectral variability parameters, taking into account the

large measurement errors of the 3XMM-SSC fluxes, and both possible dependences of $\Delta \log F$ on $\Delta\Gamma$ and viceversa (Serafinelli et al., 2017a).

I also analyzed a sample of nearby Seyfert galaxies (Serafinelli et al., 2018a), covering nearly all type of spectral features that we expect to influence the observed spectral variability. The sample of X-ray bright sources was taken from Sobolewska & Papadakis (2009), with the addition of Low-Luminosity AGN M81, included to investigate a possible, "harder when brighter", opposite trend, as found by Connolly et al. (2016), analyzing Swift data. For these sources it is possible to obtain accurate photon indices. For all but M81 I found a softer when brighter trend, with high $\Gamma - \log F$ correlation and high confidence, while M81 mildly suggests the opposite trend, but with low correlation and high probability of finding it by chance. I computed both the accurate and approximate photon indices for this sample, and I compared the spectral variability β, as obtained with both methods.

Finally, I studied the spectra of 13 observations of PG 1114+445 (12 XMM-Newton and one ASCA), finding multiple absorbers (Serafinelli et al., 2018b), one being a warm absorber, one a low-ionization, fast ($v \sim 0.104c$, with c the speed of light) outflow in the soft ($E < 2$ keV) X-rays, and one, observable in three observations, being a highly ionized, ultra-fast outflow (UFO, Tombesi et al., 2010a,b), with velocity of about 15% of the speed of light.

This thesis is organized as follows. Chapter 1 is an introductory overview of the main AGN properties. In Chapter 2, the X-ray spectral features of Active Galactic Nuclei are reviewed. Chapter 3 will describe the instruments and the data that has been used for this work. Chapter 4 introduces the approximate method to compute the spectral variability of 2 700 quasars from tabulated data. Chapter 5 describes the spectral variability study of nearby Seyfert galaxies. Finally, Chapter 6 gives a detailed account of the analysis of the observations of PG 1114+445. The data reduction pipeline of XMM-Newton is reported in Appendix A.

Chapter 1

ACTIVE GALACTIC NUCLEI

Active Galactic Nuclei (e.g., Urry & Padovani, 1995; Peterson, 1997; Netzer, 2013) are very bright extragalactic objects, situated in the dynamical center of their host galaxies. Their extremely luminous emission, $\gtrsim 100$ times the bolometric luminosity of non-active galaxies, is powered by the accretion of matter around black holes with masses ranging in $M \sim 10^6 - 10^9 M_\odot$ (Cattaneo et al., 2009), that therefore are usually labelled as "supermassive" black holes (SMBH).

1.1 Historical background

Historically, the first track of Active Galactic Nuclei (AGN) is found in E.A.Fath's dissertation work in 1908 at Lick Observatory (Fath, 1909), where he noted the presence of resolved strong emission lines in NGC 1068, with widths of hundreds of km s^{-1}.
It wasn't until 35 years later that it was discovered that there are many galaxies with the same properties. Seyfert (1943) was able to identify emission lines (up to 8500 km s^{-1}) in five spiral galaxies, NGC 1068, NGC 3516, NGC 4051, NCG 4151 and NCG 7469. It was determined that these galaxies belonged to the same class of sources, later called *Seyfert galaxies*.
Later on, Woltjer (1959) made some remarks about these sources. First of all, the nucleus of these galaxies is not resolved, and therefore their radius cannot be larger than 100 pc. Also, assuming that every spiral galaxy undergoes through one or more Seyfert phase during its lifetime, since 1 out of 100 galaxies shows nuclear activity and the age of the Universe is of order of 10^{10} years, the duration of the active phase cannot be longer than $10^{10}/100 \simeq 10^8$ years. Finally, given the estimated 100 pc radius of the emitting region, the measured dispersion velocity of order $\sim 10^3$ km/s, with a simple virial argument one

could estimate the mass of the nucleus, by using the formula $M \simeq v^2 r/G$; with this argument the mass of the AGN can be estimated as $M \simeq 10^{9\pm1} M_\odot$.
Large radio surveys in the sixties, such as the 3C (Edge et al., 1959) and revised 3CR (Bennett, 1962) found some stellar-like objects with faint nebulosity, whose spectrum showed broad emission lines at unusual wavelengths, with an ultraviolet excess respect to emission from other stars. These objects were labelled as "quasi-stellar objects" (QSO) or simply "quasars". The nature of these QSOs was discovered by Schmidt (1963), who recognized the Balmer hydrogen series Hβ, Hγ, Hδ, and Hϵ in source 3C 273, at redshift $z \simeq 0.16$, explained as due to the Hubble expansion. With this proposed redshift, he also found the UV line of Mg II λ2798, and Oke (1963) identified the Hα line at infrared observer frame $\lambda = 7600$ Å. The least objectionable explanation (Greenstein & Schmidt, 1964) was that these lines were coming from an extragalactic source, with redshifts following the Hubble expansion. Based on light travel constrains from optical variability measures, Greenstein & Schmidt (1964) proposed a model in which a central source of mass $\sim 10^9 M_\odot$ and radius $r \sim 1$ pc is present, emitting the optical continuum, later identified with the supermassive black hole with Schwarzschild radius of $\sim 10^{-4}$ pc (see Shields, 1999, for a detailed review) and the surrounding accretion disk, enveloped by a region that is responsible for the broad emission lines, with an even larger radio emitting region.
This is the so-called *black hole paradigm* that, even with refinements, corrections and adjustments, is still accepted nowadays.

1.2 Electromagnetic emission and spectral energy distribution

The spectral emission of Active Galactic Nuclei is usually described by means of the spectral energy distribution (SED), which is described in terms of the monochromatic flux (or sometimes luminosity) per unit frequency F_ν (erg s^{-1} cm^{-2} Hz^{-1}). The SED of the majority of AGNs can be locally described as

$$F_\nu \propto \nu^\alpha, \tag{1.2.1}$$

where α is called spectral index. Depending on the convention, the spectral index can be defined with the opposite sign, so that $F_\nu \propto \nu^{-\alpha}$. In this thesis, however, we follow the definition of α according to Eq. 1.2.1. For instance, the continuum spectrum of many luminous AGNs in the $1200 - 6000$ Å band can be adequately described by $\alpha \simeq -0.46$

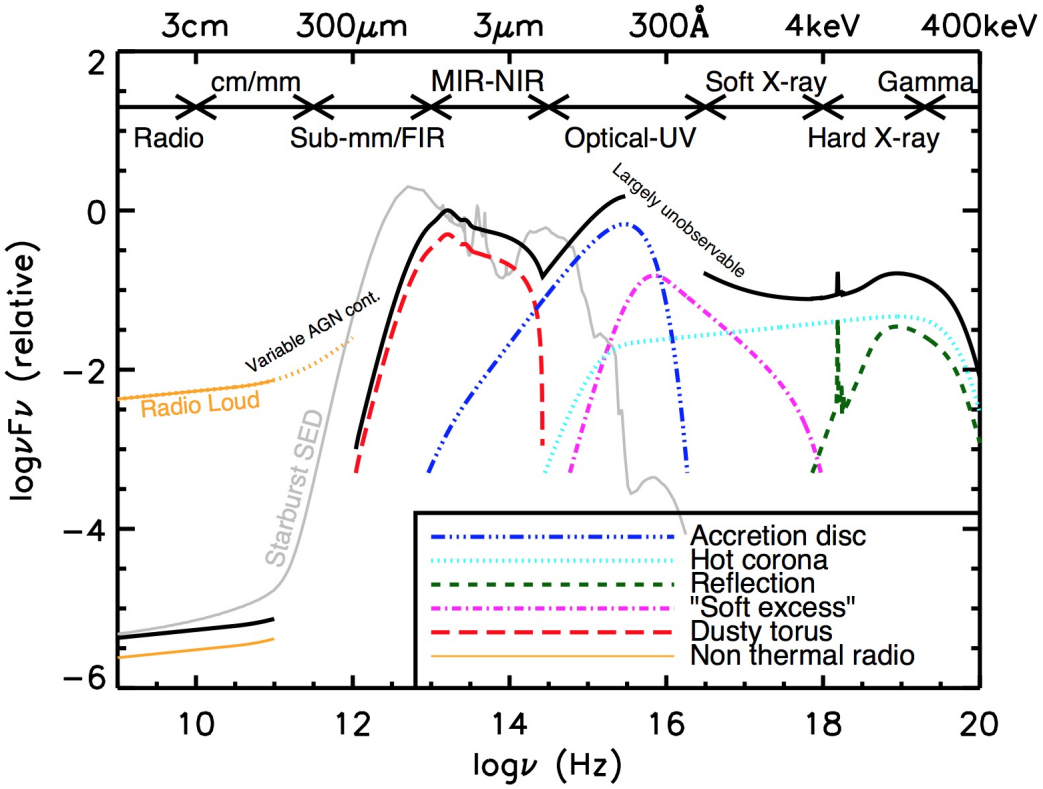

Figure 1.1: Schematic typical SED of Active Galactic Nuclei. The yellow lines at radio frequencies show the difference between radio-loud and radio-quiet sources. At sub-millimetric radio or infrared (IR) frequencies we can see the "infrared bump", due to emission from the dusty torus in the mid-IR band, or from other cold dust features from the host galaxy in the far-IR, as shown in by the grey curve. The blue curve represents the so-called "big blue bump", with emission from the accretion disk. A pink curve displays the X-ray "soft excess" emission. The cyan curve is the X-ray continuum, coming from a hot corona, very close to the supermassive black hole. Finally, the green curve is the so-called "Compton hump", due to the reflection on the disk of X-rays from the corona, which are hardened in the process. The overall SED is represented by the black line. Taken from Harrison (2016).

(Vanden Berk et al., 2001).

As we will see in Chapter 2, in the X-ray band it is custom to use the photon index $\Gamma = 1 - \alpha$, so that the monochromatic flux is locally

$$F_E \propto E^{1-\Gamma}, \tag{1.2.2}$$

with $E = h\nu$ being the energy of the photon.

A schematic broadband SED of a typical AGN is shown in Figure 1.1.

The optical images of many luminous AGN show evidence of a strong nuclear point-like source, whose surface brightness exceeds the one from the galaxy that hosts the active nucleus. Active galactic nuclei of this kind are usually called *type-1*, while AGN that do

not show this excess are usually labelled as *type-2*.

The typical optical/UV spectrum of type-1 and type-2 AGN is shown in Fig. 1.2. The first group usually shows broad emission lines, among which the most important are the Balmer sequence (the stronger lines are Hα λ6563, Hβ λ4861, and Hγ λ4341), Mg II λ2798, C IV λ1549, and the Ly α hydrogen line at $\lambda = 1216$ Å (see Table 1.1). These broad emission lines, whose Full Width Half-Maximum (FWHM), if interpreted as Doppler broadening due to the velocity dispersion of the emitting material, is usually of the order of $2000 - 10000$ km s^{-1}. Unlike type-1 sources, type-2 AGNs only show narrow emission lines instead (FWHM$\sim 400 - 800$ km s^{-1}, such as the [O III] λ5007 λ4959 doublet, the Balmer sequence, the [S II] λ6716 λ6731 doublet, or the He I λ5876 line.

One notable exception to this classification is represented by narrow-line Seyfert 1 (NLS1) galaxies, a peculiar kind of type-1 AGN, categorized as such if FWHM(Hβ) $\lesssim 2000$ km s^{-1} (Osterbrock & Pogge, 1985). Some of these sources show FWHM(Hβ) < 1000 km s^{-1}, the same order as type-2 sources. Such sources are classified as type-1 because of the presence of non-stellar continuum and for the strength of their emission lines, such as Fe II, typical of type-1 sources (e.g., Boroson, 2011).

Moreover, there are also intermediate sub-classes of AGN, introduced by Osterbrock (1981), spanning from type 1.2 to type 1.9, according by the relative intensities showed by the broad emission lines.

In the near and medium infrared (NIR and MIR, respectively) the emission is mostly due to reprocessing of the primary AGN radiation by hot (~ 2000 K), warm (~ 1000 K) or cold (~ 100 K) dust structures at ~ 1 pc. The far infrared (FIR) emission is instead believed to be originated by cold dust in the host galaxy.

The main radio feature of AGNs is the presence of single or double radio-emitting lobes, whose dimensions can be significantly higher than the dimensions of the host galaxy itself, with very strong radio jets coming from the nucleus itself. Not every AGN presents such lobes or emits strong radio waves, in fact active nuclei can be divided into "radio-loud" and "radio-quiet" sources, according to the value of the *radio loudness parameter*, defined as the ratio between the radio flux (or luminosity in some cases) and the optical/UV flux at a reference wavelength. In this thesis we used the Jiang et al. (2007) definition of such parameter

$$R = \frac{F_\nu(6 \text{ cm})}{F_\nu(2500 \text{ Å})}. \tag{1.2.3}$$

For $R \leq 10$ we have a radio-quiet AGN, while for $R > 10$ a radio-loud source.

Some sources, known as "blazars" have a strong emission in the γ-ray band. Such sources are believed to be those ones with face-on orientation and powerful jets parallel to the line

of view.

The X-ray spectrum of AGNs, which is the main focus of this thesis, will be described in detail in Chapter 2.

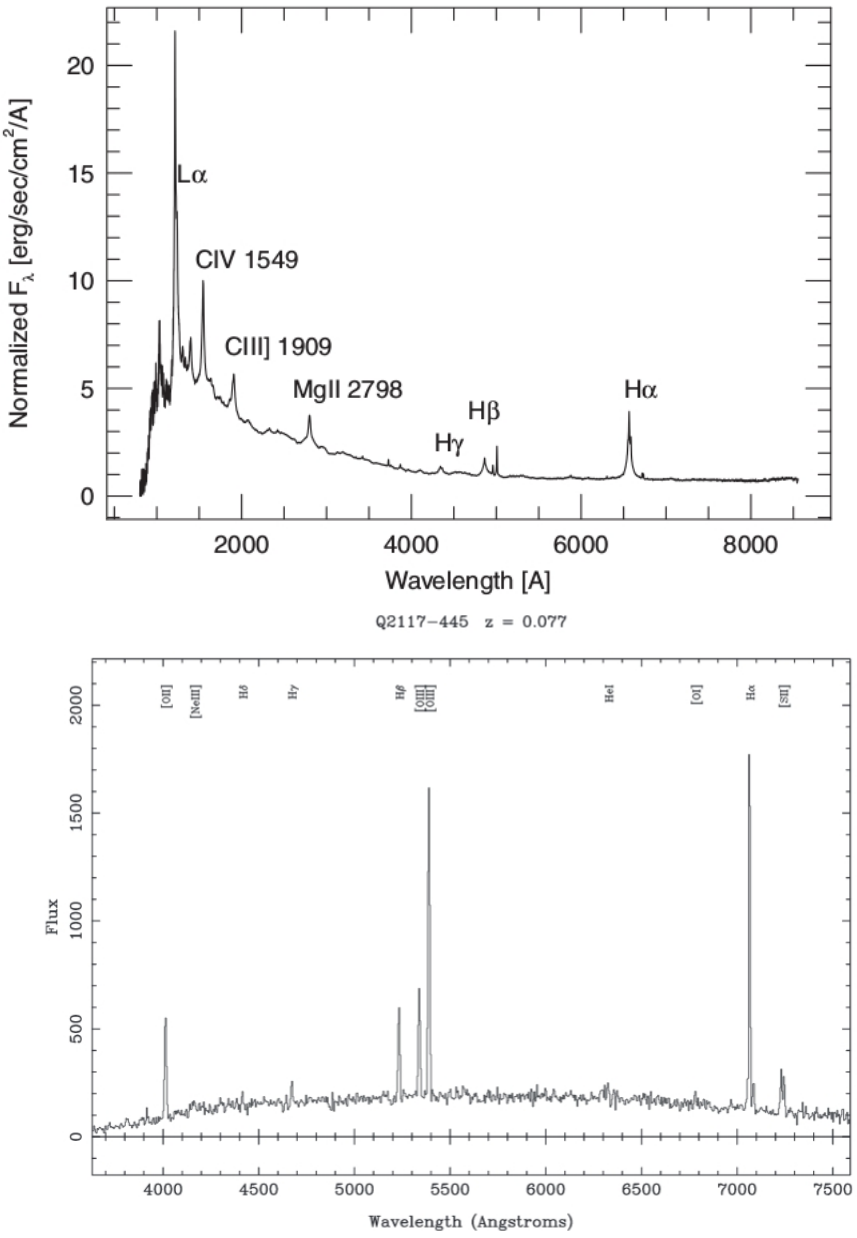

Figure 1.2: *Top.* Typical spectrum of a type-1 AGN. The Balmer sequence, a broad C IV line, the Lyman α and other broad lines are clearly visible. Taken from Netzer (2013). *Bottom.* The spectrum of a typical type-2 source, Q2117-445, at redshift $z = 0.077$ is shown. The [O III] doublet is present, as the narrow Balmer sequence and [S II] doublet. Taken from Hawkins (2004).

1.3 The structure of Active Galactic Nuclei

All the spectral features discussed in Section 1.2 are believed to be originated in different parts of the active nucleus. In fact, the optical continuum is believed to be originated from a optically thick, geometrically thin accretion disk around the central SMBH, while the broad and narrow emission lines are produced in the so-called *broad-line region* and *narrow-line region* respectively. The infrared emission is most probably reprocessed emission on a dusty torus situated around the system. The radio emission is both nuclear and jetted, although not all AGNs present a jet, which is also responsible for the γ-ray emission in BL Lac sources. The fraction of jetted AGN is still debated and affected by large uncertainty (e.g., Padovani et al., 2017), although a fraction of 0.15 is often quoted (e.g., Kellermann et al., 1989).
The X-ray emission is produced by a hot electron plasma region, very close to the SMBH, commonly known as the *corona*, which we will describe in Chapter 2. A visual representation of a typical AGN is shown in Fig. 1.5.

1.3.1 The accretion disk

It is now widely accepted that the optical/UV continuum comes from an optically thick, geometrically thin accretion disk around the SMBH. It is likely that many AGN present other kinds of disk, such as for example thick disks with toroidal shape, although they are much more difficult to describe, because of complex effects due to the shape of the disk, such as self occultation of the innermost regions of the disk or strong dependence on the disk inclination (e.g., Madau, 1988).
These structures can form over a large range of conditions, when large quantities of gas fall towards the center of the galaxy and retain most of their angular momentum (e.g., Shakura & Sunyaev, 1973; Frank et al., 1985). The friction between adjacent viscous rings is able to produce a significant transfer of angular momentum towards the external part of the disk, allowing the gas to fall towards the SMBH and lose a considerable fraction of its gravitational energy.
The key quantities that govern the properties of accretion disks are the accretion rate, i.e. the time derivative of the mass, $\dot{M}$, the black hole mass $M_{\rm BH}$ and the black hole spin a. The energy associated with the accreted mass is radiated with efficiency η, which means that the luminosity will be proportional to the accretion rate

$$L = \eta \dot{M} c^2 \tag{1.3.4}$$

This is a very efficient process, since it is able to convert gravitational energy intro electromagnetic radiation with efficiencies that range from 4% up to 42% (e.g., Netzer, 2013), depending on the size of the innermost stable circular orbit (ISCO), which depends on the black hole spin. For most practical cases, a value of $\eta \simeq 0.1$, obtained assuming a mass m falling from $r = 5R_S$, with $R_S = 2GM/c^2$ being the Schwarzschild radius, can be safely assumed.
Assuming that the accretion rate $\dot{M}$ is constant, the local emission can be approximated as a black body, which means that the energy balance is given by

$$L = \frac{GM\dot{M}}{2r} = 2\pi r^2 \sigma T^4, \tag{1.3.5}$$

where the factor 2 at the denominator of the left side of the equation is due to the fact that half of the energy goes in heating the gas, and the factor 2 on the right side is due to the fact that the disk has two sides.
Taking into account a correction due to subsonic viscosity (see Shakura & Sunyaev, 1973, for details), Eq. 1.3.5 can be inverted and rewritten as

$$T = \left[\frac{3GM\dot{M}}{8\pi\sigma r^3} \left(1 - \left(\frac{R_{\rm in}}{r} \right)^{1/2} \right) \right]^{1/4}, \tag{1.3.6}$$

where $R_{\rm in}$ is the inner border of the accretion disk. For $r >> R_{\rm in}$ this equation can be approximated with

$$T \simeq 6.3 \cdot 10^5 \left(\frac{\dot{M}}{\dot{M}_{\rm Edd}} \right)^{1/4} M_8^{-1/4} \left(\frac{r}{R_S} \right)^{-3/4} {\rm K}, \tag{1.3.7}$$

with $M_8 = M/10^8 M_\odot$, where $\dot{M}_{\rm Edd} = L_{\rm Edd}/\eta c^2$ is the maximum possible accretion rate for a mass M, called *Eddington accretion rate*. The *Eddington luminosity* $L_{\rm Edd}$ is the maximum luminosity that can be emitted by a source with mass M, in order to be balanced by the gravitational field of the source itself. It is given (e.g., Peterson, 1997) by:

$$L_{\rm Edd} = \frac{4\pi G m_p c}{\sigma_e} M \simeq 1.26 \cdot 10^{38} \frac{M}{M_\odot} {\rm erg\ s^{-1}}, \tag{1.3.8}$$

with m_p the proton mass and σ_e the Thomson cross-section.
Assuming typical values of $M \simeq 10^8 M_\odot$, $\dot{M} \simeq \dot{M}_{\rm Edd}$ and $r \simeq R_S$, the blackbody temperature of Eq. 1.3.7 gives a peak frequency of

Ion	λ (Å)
Ly β	1025.7218, 1025.7229
Ly α	1215.6682, 1215.6736
N V	1238.82, 1242.80
C II	1334.53, 1335.66, 1335.71
S IV	1393.76, 1402.77
O IV	1397.23, 1407.77
C IV	1548.20, 1550.77
He II	1640
C III]	1908.73
C II	2324.21, 2328.84
Mg II	2795.53, 2802.71
He II	4686
Hβ	4861
He I	5876
O I	6300.30, 6363.78
Hα	6563
O I	8446.5

Table 1.1: List of permitted and semiforbidden intercombination lines that are often found in broad line regions (Pradhan & Nahar, 2015).

$$\nu_{\max} = \frac{2.8kT}{h} \simeq 3.6 \cdot 10^{16}\text{Hz}, \tag{1.3.9}$$

that roughly corresponds to the "big blue bump" peak, observed in the UV band.
For practical reasons, it is usually convenient to measure the accretion rate normalized to the Eddington accretion rate $\lambda = \dot{M}/\dot{M}_{\text{Edd}} = L/L_{\text{Edd}}$, often called *Eddington ratio*.

1.3.2 The broad-line region

As we stated in Section 1.2, the optical/UV spectra of type-1 AGNs show the presence of broad emission lines. A list of common lines present in AGN spectra is reported in Table 1.1. Assuming that the line broadening is due to Doppler effect, these lines have widths ranging from FWHM $\simeq 500$ km s^{-1} up to FWHM $\gtrsim 10^4$ km s^{-1}, with the most diverse line profiles, varying from line to line. Sometimes the Doppler broadening is so prominent that the line blends with closer lines. Given these high velocities, there must be a line-emitting region, close to the black hole but farther than the accretion disk, with such high velocity dispersion, commonly known as the broad-line region (BLR, e.g., Davidson & Netzer, 1979).
Modelling the shape and the physical characteristics of the BLR is not simple. Since we

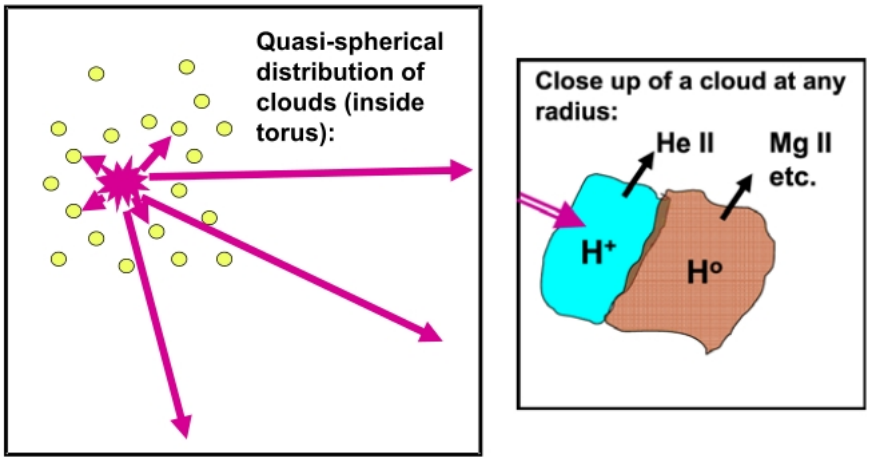

Figure 1.3: *Left.* Classical broad line region model with spherical distribution of clouds. *Right.* Simplified structure of a single cloud, with a highly ionized side facing the black hole and a moderately ionized side on the back. Taken from Gaskell (2009).

do not observe forbidden lines, that are collisionally suppressed, the electronic density must be very high. The similarity of relative intensities of the BLR with other ionized gas systems, such as the H II regions, suggests a gas temperature $T_{\rm gas} \simeq 10^4$ K, which is clearly insufficient to produce the broad AGN lines, since

$$v_{\rm gas} = \sqrt{\frac{kT_{\rm gas}}{m_p}} \simeq 10 \text{ km/s},$$

much smaller than the typical line width value of $v \sim 5000$ km s^{-1}. This clearly indicates that the origin of the Doppler broadening is not the thermal motion of the gas, otherwise we would need a temperature of $\sim 10^9$ K to produce such line widths. It is currently believed that the Doppler broadening is produced by either bulk motions of a line-emitting sperical distribution of clouds (Kaspi & Netzer, 1999), that are highly ionized on the side facing the black hole, and moderately ionized on the other side (see Fig. 1.3), or by radiation-driven winds (Murray & Chiang, 1997), or a composite of both these physical effects. Indeed, photoionization models suggest that two regions are present in the BLR, a highly ionized one with low optical depth and a moderately ionized region with higher optical depths (Collin-Souffrin et al., 1986; Gaskell, 2009), which sustains the idea that the origin of the Doppler-broadening velocity may be of multiple origin.

The broad line region reprocesses the optical/UV radiation emitted by the accretion disk by photoionization processes. The photoionization models depend on the shape of the ionizing continuum, the chemical abundances, the particle and column density of a cloud and ionization parameter, defined as

$$U = \frac{Q(H)}{4\pi r^2 c n_{\rm H}}, \tag{1.3.10}$$

where

$$Q(H) = \int_{\nu_{\rm H^+}}^{\infty} \frac{L_\nu}{h\nu} d\nu$$

is the number of photons per second, emitted by the central source, capable of ionizing hydrogen, i.e. with energy $h\nu \geq h\nu_{\rm H^+} = 13.6$ eV, and $n_{\rm H}$ is the particle density of the cloud.

Eq. 1.3.10 is not the only way of describing the ionization of the system. Another common ionization parameter, commonly used in the X-ray band, which we will use in this thesis, is ξ, defined as

$$\xi = \int_{13.6{\rm eV}}^{13.6{\rm keV}} \frac{L_E}{r^2 n_{\rm H}} dE, \tag{1.3.11}$$

integrated on the photon energy $E = h\nu$.

The size and the structure of the broad line region can be inferred by the observation of the response to the continuum variations of the structure of the emitting lines, which appear to "reverberate", following the continuum variability. This process is known as *reverberation mapping* (e.g., Peterson, 1993; Peterson & Wandel, 1999; Kaspi et al., 2000). Assuming that the continuum is produced by a single source, much smaller than the BLR, that the clouds occupy a very small percentage of the total volume of the region (it can be found, by comparing the emissivity of the C IV with the one expected by a continuous medium, that the fraction of volume filled by the clouds is of the order $\epsilon \sim 10^{-6}$, Peterson, 1997), and that the relation between the optical/UV observable continuum and the ionizing radiation responsible for the variability of the lines are simply related, one could estimate the BLR size by correlating the continuum variations to the line variations at various delays Δt. The time at which the two quantities are most correlated will be the light-travel time $\tau_{\rm LT}$, that can give an estimate of the broad-line region size $R_{\rm BLR} \propto \tau_{\rm LT}$. The method also assumes that $\tau_{\rm LT}$ is shorter than the dynamical scale of the BLR and that the time in which the clouds responds to the radiation is very small compared to $\tau_{\rm LT}$. Since different lines are often found to be correlated with the continuum at different delayed times, it is likely that the broad line region is stratified, with different elements emitting lines at different distances from the center (Dietrich et al., 1993).

Once the typical size of the broad line region for a given line, $R_{\rm BLR}$, is computed with this method, one could use the Virial Theorem to estimate the mass of the black hole (e.g., Kaspi et al., 2000), which is responsible for the cloud motion:

$$M_{\rm BH} = f\frac{R_{\rm BLR}\cdot(\Delta v)^2}{G} \tag{1.3.12}$$

with $R_{\rm BLR}$ computed with the reverberation mapping, and $(\Delta v)^2$ measured from the line we are considering. f is the form factor and depends on the geometry of the broad line region and can be estimated from various methods, such as for example requiring that the $M-\sigma_*$ relation (with σ_* being the velocity dispersion of the stars in the galaxy) of active galaxies agrees with the non-active galaxies relation (e.g., Ferrarese & Merritt, 2000; Merritt, 2013), as done with Hβ reverberation mapping by Onken et al. (2004), who found $f\sim 5.5$.
Kaspi et al. (2000) found that the size of the BLR is correlated to the luminosity of the source, roughly following the relation $R_{\rm BLR}\propto L^{0.7}$, later updated by Bentz et al. (2009) to $R_{\rm BLR}\propto L^{0.5}$. This relation can be used to estimate the black hole mass from single-epoch line width measurements (e.g., Shen et al., 2011; Kozłowski, 2017a), by using the relation

$$\log\left(\frac{M_{\rm BH}}{M_\odot}\right) = a + b\log\left(\frac{\lambda L_\lambda}{10^{44}\ {\rm erg\ s^{-1}}}\right) + 2\log\left(\frac{\rm FWHM}{\rm km\ s^{-1}}\right), \tag{1.3.13}$$

with a and b that depend on the peculiar $R_{\rm BLR}-L$ relationship considered. It is clearly less accurate than estimating $M_{\rm BH}$ from reverberation mapping estimates, but this method is able to estimate an order of magnitude of the black hole mass. Combining Eqs. 1.3.8 and 1.3.13 it is also possible to estimate the Eddington ratio, and therefore the accretion rate, of the source $\lambda = L/L_{\rm Edd}$.

1.3.3 The narrow-line region

The narrow emission lines, that we find in both type-1 and type-2 sources, are produced at distances of $\sim 10^2-10^3$ pc from the central SMBH. In this region of the AGN, known as narrow-line region (NLR), the gas is weakly irradiated and less gravitationally influenced by the central engine, which however is still the dominant ionization source.
Typical narrow lines includes forbidden transitions, such as [O I], [O II], [O III], [N II] or [N III], which are not collisionally suppressed as in the case of the broad line region, because the electronic densities are significantly lower ($N_e \gtrsim 10^3$ cm^{-3} for the NLR and $\gtrsim 10^9$ cm^{-3} for the BLR, see e.g., Peterson, 1997). Since most of these transitions involve ground configuration, lines from singly or doubly ionized atoms are closely spaced. We find lines from low ionization states, such as [O I], and high ionization states, such as [Fe VII], which means that the narrow line region is photoionized by an AGN.
The FWHM of the NLR has values is in the range 200 km s^{-1} $\lesssim$FWHM$\lesssim$ 900 km s^{-1},

with typical values around $350 - 400$ km s^{-1}. In extreme cases, such as NGC 1068, the width of some lines can reach ~ 1200 km s^{-1}.
The NLR is the only component in AGNs that can be spatially resolved in the optical band (e.g., Liu et al., 2013). That means that its radius can be in principle directly measured. The radius of the NLR is correlated with the luminosity of the [O III] line, according to $R_{\rm NLR} \propto L^k_{\rm [O\ III]}$, with k ranging from $k \simeq 0.3$ (Schmitt et al., 2003) to $k \simeq 0.5$ (Bennert et al., 2002). The increase of the NLR size saturates at ~ 7 kpc (Hainline et al., 2014).

1.3.4 The torus

The central engine and the broad line region are probably surrounded by optically thick clouds, located in a toroidal structure (Krolik & Begelman, 1988). The torus is usually depicted as a "doughnut-like" object (see Fig. 1.5), that is presumably composed by molecular clouds, accreted from the host galaxy.
This dusty torus is responsible for the infrared reprocessed emission, that can be compared with models in order to infer the dimensions of the structure. Before the advent of high resolution IR observations, Pier & Krolik (1992, 1993) speculated that the torus might have compact dimensions ($r \sim 5 - 10$ pc) and is surrounded by a larger torus with $r \sim 30 - 100$ pc. High resolution IR observations confirmed the compact dimensions of the torus. For NGC 1068, it was discovered that the $\lambda = 10$ μm emission is constrained in a $r \lesssim 1$ pc region with temperature $T \sim 800$ K, surrounded by a cooler ($T \sim 300$ K), more extended ($r \sim 2 - 3$ pc) region (e.g., Jaffe et al., 2004; Burtscher et al., 2013).
These compact dimensions might suggest an alternative scenario, in which the torus is not in a steady-state, but is rather the byproduct of hydromagnetic disk winds. According to this model (e.g., Emmering et al., 1992; Königl & Kartje, 1994; Elitzur & Shlosman, 2006), the torus would simply be a region in which the clumpy winds become optically thick, rather than a separate entity produced by inflows of dusty material from the host galaxy.

1.4 Winds

The black hole mass in Active Galactic Nuclei, $M_{\rm BH}$, is found to be correlated with the mass of the bulge $M_{\rm b}$ of the host galaxy (e.g., Häring & Rix, 2004), i.e.,

$$\frac{M_{\rm BH}}{M_{\rm b}} \sim 10^{-3}. \tag{1.4.14}$$

It is also found (e.g., Ferrarese & Merritt, 2000; Gebhardt et al., 2000) that the black hole mass and the stellar velocity dispersion σ_* are also correlated, following

$$M_{\rm BH} \propto \sigma_*^{4.4}. \tag{1.4.15}$$

The black hole gravity has a negligible impact on its host galaxy (e.g., King & Pounds, 2015), but from Eq. 1.3.4 we know that the black hole growth is due to luminous accretion of gas (see Section 1.3.1). The released energy, $E_{\rm BH} \simeq \eta M c^2 \sim 2 \cdot 10^{53} (M_{\rm BH}/M_\odot)$ erg, is much larger than the binding energy of the bulge, $E_{\rm b} \sim M_{\rm b}\sigma_*^2 \sim 8 \cdot 10^{50} (M_{\rm BH}/M_\odot)\sigma_{200}^2$ erg, where we used Eq. 1.4.14 and $\sigma_{200} = \sigma_*/(200 \text{ km s}^{-1})$. This means that the host galaxy should feel the presence of the BH through the energy emitted by the AGN, even though its gravitational effect is negligible. The black hole therefore communicates some of its great binding energy $E_{\rm BH}$ to the gas reservoir, which is "cleaned" from the bulge, potentially limiting its own growth. This process is commonly known as *feedback* (e.g., Silk & Rees, 1998; Fabian, 2012; King & Pounds, 2015).

Considering just the binding energy of the gas fraction of the bulge, $E_{\rm gas} = f_{\rm g} E_{\rm b}$, with $f_{\rm g} \simeq 0.16$, the cosmological mean value, the relation becomes

$$E_{\rm BH} \sim 2 \cdot 10^3 E_{\rm gas}. \tag{1.4.16}$$

The accretion energy is mainly released as radiation, but observations confirm that most of the light can freely escape from the AGN, and thus radiation is not particularly suited to transport the energy from the SMBH to the host. This suggests that the energy transport is mainly mechanical, carried on by near-isotropic winds that carry large momentum fluxes.

The gravitational energy produced in the accretion disk could in fact also be converted into kinetic energy via radiation pressure, producing winds of gas, that is blown away from the disk.

In the UV, winds are commonly detected through Broad Absorption Lines (BALs, Weymann & Foltz, 1983; Turnshek et al., 1988; Elvis, 2000), that appear as blueshifted troughs in the proximity of broad emission lines (see Fig. 1.4) in a peculiar sub class of sources, called BALQSOs or BAL quasars. It is believed that these troughs are produced by ionized winds outflowing along the line of sight (see Fig. 1.4) for those AGNs which are inclined of $40 - 45°$ respect to the line of sight (Elvis, 2000), or perhaps they represent an early evolutionary state of the quasar, in which the winds are blowing out the dusty cocoon, before becoming a fully exposed quasar (e.g., Becker et al., 2000; Farrah et al., 2007; Far-

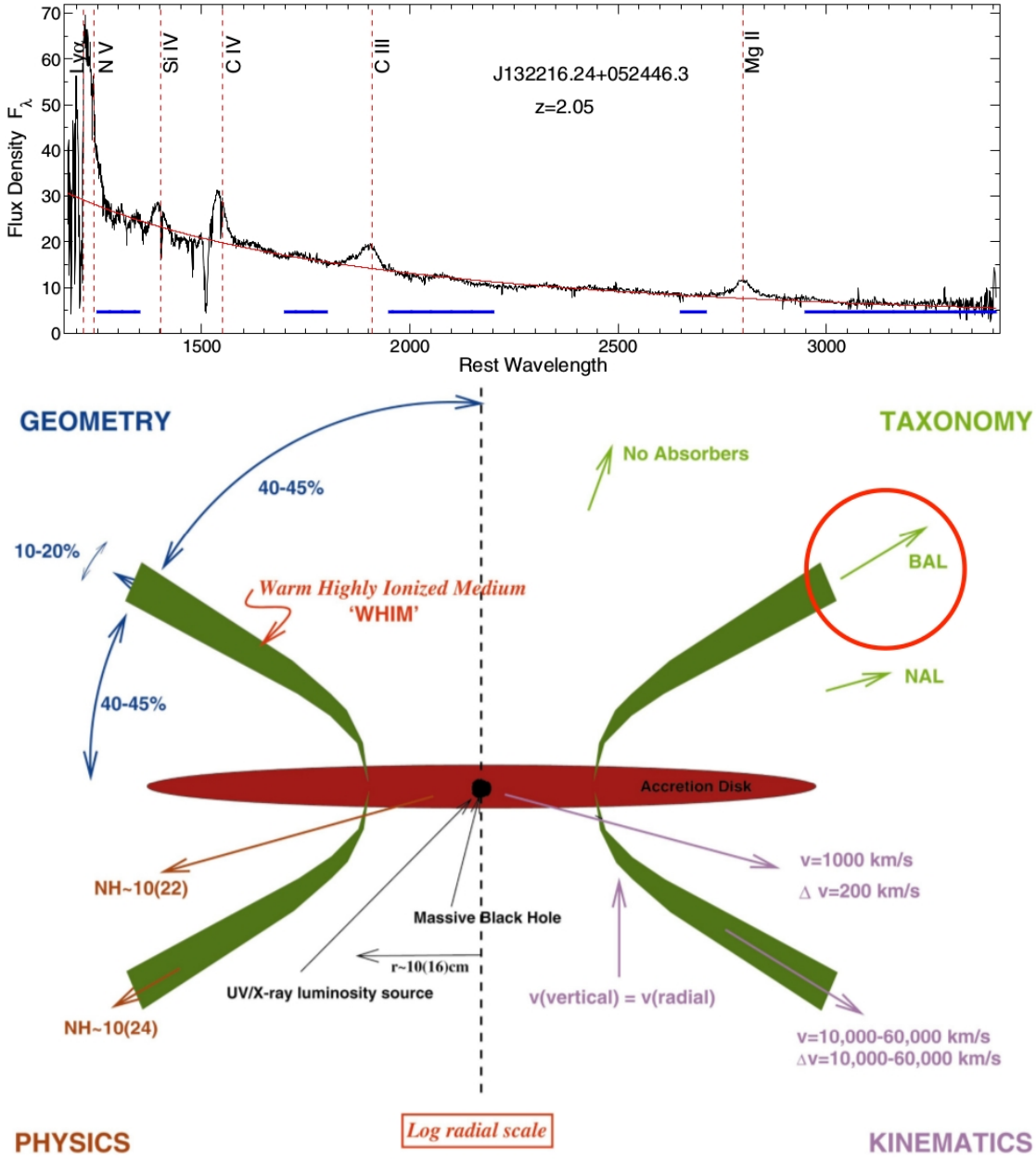

Figure 1.4: *Top.* Sloan Digital Sky Survey UV spectrum of a BAL quasar (taken from Filiz Ak et al., 2012). The blueshifted absorption trough of the C IV line is clearly visible at $\lambda_{\rm rest} \simeq 1500$ Å. *Bottom.* Schematic view of a Broad Absorption Line (BAL) Quasar. The blueshifted absorption lines are due to powerful winds with velocities in the range $v \sim 0.05 - 0.40c$, outflowing with an inclination of $\sim 40 - 45°$ with respect to the AGN plane. Image credit: Elvis (2000).

rah et al., 2012).

These ionized winds produce significant absorption in the soft X-ray band, an observational phenomenon commonly known as *warm absorber* (WA), with velocities in the range $v \sim 100 - 1000$ km s^{-1}. Moreover, more ionized winds, visible through Fe XXV and Fe

XXVI absorption lines, are usually much faster (up to $v \sim 0.1 - 0.4c$, Tombesi et al., 2010b) and are usually labelled *ultra-fast outflows* (UFOs). Both of these phenomena will be described in detail in Chapter 2.

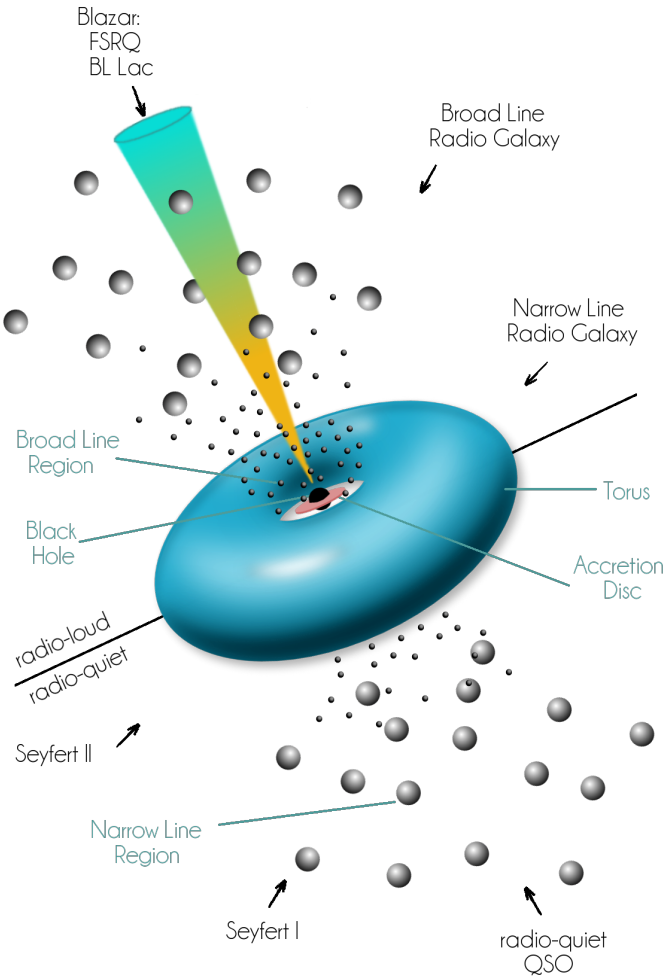

Figure 1.5: Schematical view of the structure of a typical AGN, according to the unified model (Antonucci, 1993; Urry & Padovani, 1995). Depending on the angle of view between the object and the line of sight, we see different classes of AGNs. If we look at an AGN face-on, we are able to see the broad line region and therefore we have a type-1 source. On the contrary, an edge-on source will be seen through the obscuring torus, and therefore the broad lines are mostly unobservable. In this case we observe a type-2 source. If a jet is present, and the line of sight is coincident with it, we will see a blazar, while for other lines of sight we will have radio-loud AGNs. If the jet is not present, the radio emission from the source will be lower and we will observe a radio-quiet source. The accretion disk, broad- and narrow-line regions, the torus and the jet are shown. Image credit: Krauss (2016)

1.5 The unified scheme

The AGN phenomenon is observed in a multitude of different ways, that generates a huge number of classes and sub-classes of sources. A list of the main classes of AGN can be found in Table 1.2.

The addition of the obscuring torus-like absorbing structure (see Section 1.3.4) perfectly

Class	Description
Seyfert 1	Type-1 active galaxy, typically nearby, with broad emission lines (FWHM$\gtrsim$ 1000 km s^{-1}).
Seyfert 2	Type-2 active galaxy, typically nearby, with absent broad emission lines. Only narrow lines (FWHM$\lesssim$ 1000 km s^{-1}) are observed.
Quasar/QSO	Type-1 quasi-stellar source. Similar to Seyfert 1, but more luminous (typically $\mathcal{M}_{\rm B} \lesssim -22$).
QSO2	Type-2 quasi-stellar source. Similar to Seyfert 2, but more luminous (typically $\mathcal{M}_{\rm B} \lesssim -22$).
Radio-quiet AGNs	Active Galactic Nuclei with radio loudness parameter $R \leq 10$ (see Section 1.2). Jets are typically absent.
Radio-loud AGNs	Active Galactic Nuclei with radio loudness parameter $R > 10$. Typically jetted.
BAL QSO	Quasar with broad absorption lines associated with powerful outflowing winds (see Sec. 1.4).
LLAGN	Low-luminosity AGN, with typically $L/L_{\rm Edd} \lesssim 0.01$ (e.g., Ho, 2008).
NLS1	Narrow-line Seyfert 1. Sources with with FWHM(Hβ)$\lesssim$ 2000 km s^{-1}, but typical type-1 lines, such as Fe II.
Blazar	Highly variable sources with γ-ray emission.

Table 1.2: List of main Active Galactic Nuclei classes with brief description. $\mathcal{M}_{\rm B}$ is the absolute magnitude in the blue band.

explains the differences between type-1 and type-2 radio-quiet sources (Antonucci, 1993; Urry & Padovani, 1995). The viewing angle i determines what part of the AGN can be observed from a given line of sight (Fig. 1.5). If we are looking at the source at a wide angle respect to the AGN plane, we are able to see the broad-line region, and therefore the spectrum of such source will include broad emission lines. On the contrary, for near edge-on sources, the BLR is obscured by the torus, and therefore all we can see is the narrow-line region, located farther from the black hole. In that case, only narrow lines will be present in the spectrum of the source.

The torus by itself is not able to include radio-loud and γ-ray sources in this picture. The unification of this kind of objects into a single generalized model can be done with the introduction of a relativistic jet, coming from the proximity of the black hole. According to this scheme, radio-loud sources are typically those AGNs with such jets, while radio-quiet

sources typically show no presence of the jet. Since evidence of apparent superluminal motion - usually associated with relativistic particle motion towards the observer, within the jet - is often found in blazars (Vermeulen & Cohen, 1994), it is believed that these sources are most probably jetted AGNs, with the relativistic jet aligned with the line of sight, from which the γ-ray emission comes from.
While the properties of NLS1 are probably explained with the low mass of their central black holes (Komossa, 2008), LLAGNs require another element to be added to the scheme. These sources, in fact, have extremely low accretion rates (i.e., $L/L_{\rm Edd} \lesssim 0.01$; Ho, 2008). At these low accretion rates it has been proposed (e.g., Reynolds et al., 1996) that the accretion disk emission is most probably dominated by advection of material onto the black hole (advection-dominated accretion flows, ADAF) rather than radiative efficiency as in more luminous Seyfert galaxies and quasars.

1.6 Variability

Active Galactic Nuclei are well-known to be variable in every band of the electromagnetic spectrum (e.g., Giallongo et al., 1991; Mushotzky et al., 1993; Vanden Berk et al., 2004; Barvainis et al., 2005; MacLeod et al., 2010; Kozłowski et al., 2016; Vagnetti et al., 2016; Kozłowski, 2017b; Middei et al., 2017). There is still great uncertainty about the origin of variability, although it is believed that disk instabilities are likely to generate the observed flux variations in the optical/UV band. This hypothesis is supported by the similarity of the variability patterns to simulations of accretion disk instabilities (e.g., Chen & Taam, 1995; Vanden Berk et al., 2004; Kozłowski, 2016), although other explanations, such as thermal fluctuations, have been proposed (e.g., Kelly et al., 2009).
With the exception of candidate binary sources (e.g., Graham et al., 2015a,b), for which a periodic variability is often found, the typical AGN variability is stochastic (e.g., Kelly et al., 2009; Andrae et al., 2013; Zu et al., 2013), and can be quantified by the power spectral density (PSD), by means of the Fourier transform of the time series. At low frequencies a flat, or "white noise", spectrum (f^0) is often found, while at higher frequencies the PSD appears to follow a "red noise" spectrum (f^{-2}) or even steeper dependences (f^{-3}, e.g., Mushotzky et al., 2011).
Another tool to quantify variability, often used in the X-ray band, is by means of the so-called *normalized excess variance* (NXS, e.g., Nandra et al., 1997; Turner et al., 1999), defined as

$$\sigma^2_{\rm NXS} = \frac{S^2 - \sigma^2_n}{\langle f \rangle} \tag{1.6.17}$$

where $\sigma_n^2 = \sum_{i=1}^{N} \sigma_i/N$ is the mean square photometric variance of the noise, given by the telescope, $\langle f \rangle = \sum_{i=1}^{N} f_i/N$ is the mean flux computed from all the available flux measures, and $S^2 = \frac{1}{N-1} \sum_{i=1}^{N} f_i^2 - \langle f \rangle^2$ is the variance of the light curve.
Another common method to quantify AGN variability is the *structure function* (SF, e.g., Simonetti et al., 1984, 1985; Di Clemente et al., 1996; Collier & Peterson, 2001; Vagnetti et al., 2011), defined by

$$\mathrm{SF}(\Delta t) = \sqrt{\langle [m(t + \Delta t) - m(t)]^2 \rangle - \sigma_0^2}, \tag{1.6.18}$$

with $m(t)$ being the magnitude at a given time t, while σ_0 is the contribution of the errors to variability, taking into account uncertainties at both times t and $t + \Delta t$ (see Vagnetti et al., 2016, for details).
For a given time lag Δt, all pair of points are identified, and the root mean squared of the magnitude difference is calculated. Typically, SFs can be described at short time lags as single power law with a slope of $\gamma \sim 0.5$ in the optical/IR band, which corresponds to a PSD slope of ~ -2 (e.g., Collier & Peterson, 2001; MacLeod et al., 2012; Kozłowski, 2016; Kozłowski et al., 2016), while on longer time lags it flattens to $\gamma \simeq 0$. The so-called *decorrelation timescale* τ is the transition time lag between the two trends, and it takes this name because for $\Delta t \lesssim \tau$ the data points are correlated, while for $\Delta t \gtrsim \tau$ they become uncorrelated.

1.6.1 Spectral variability

Given the uncertainty on the nature of the variability driver, one tool of high interest for understanding the relation between accretion disk and variability properties, is the spectral variability, i.e. the changes of the spectral shape of the continuum during flux variations. For example, the spectral shape is expected to change when the variations of the flux are due to local flare or a hot spot in the accretion disk, because their SEDs would be significantly different from that of the accretion disk. On the contrary, if the spectrum does not change with the flux variations, there must be a mechanism that keeps the temperature of the accretion disk constant.
Currently, there are two claims for the spectral variability of the optical/UV emission continuum. Winkler (1997) studied the relationship between fluxes at two different bands on the same night, finding a linear correlation between any combination of two bands. He interpreted the result as a constant spectral shape of the continuum during flux variations. On the contrary, Giveon et al. (1999), Webb & Malkan (2000) and Trèvese & Vagnetti (2002) found a hardening of the spectrum when the the source is brighter (so-called "bluer

when brighter", or "harder when brighter" trend).
In order to quantify the spectral variability of a source, Trèvese & Vagnetti (2002) introduced a spectral variability estimator β, defined as

$$\beta \equiv \frac{\alpha(t+\Delta t)-\alpha(t)}{\log F_{\rm B}(t+\Delta t)-\log F_{\rm B}(t)} = \frac{\Delta\alpha}{\Delta \log F_{\rm B}}, \tag{1.6.19}$$

where $\alpha(t)$ is the spectral index at a given time t, and $\log F_{\rm B}(t)$ is the flux in a given band B.
Given how easily β can be adapted to properly describe the spectral variability in the X-ray band (see Chapter 2), in terms of photon index variations over flux variations, in this thesis we extensively made use of this parameter for our analysis.

Chapter 2

X-RAY SPECTRUM AND VARIABILITY

2.1 The X-ray emission from Active Galactic Nuclei

The X-ray radiation is a part of the electromagnetic spectrum that spans from wavelengths of ~ 100 Å to ~ 0.1 Å, which correspond respectively to frequencies from $\sim 3 \cdot 10^{16}$ Hz to $\sim 3 \cdot 10^{19}$ Hz. Due to the way in which the detectors in this band work (counts of photons, each with its own energy, see Chapter 3), X-rays are usually described in terms of the photon energy $E = h\nu$. The energy of X-ray photons spans therefore from ~ 0.1 keV up to ~ 100 keV.

Non-thermal processes that can generate photons with such energies are synchrotron, fluorescence, bremmsstrahlung, and Comptonization. In the case of Active Galactic Nuclei, the most important process that generates X-ray radiation is Comptonization, although other processes might be at work. For example fluorescence transition in the case of the iron Kα line, or, as in the case of AGN jets, synchrotron radio emission could be upscattered by inverse Compton to X-rays by the same electrons that generate the radio emission, in a process known as synchrotron self-Compton.

As will be described in detail in Sect. 2.3, strong X-ray variability is observed over periods of days or even years (e.g., Markowitz & Edelson, 2004; Vagnetti et al., 2011; Shemmer et al., 2014; Vagnetti et al., 2016), but also at very short timescales, such as hours (e.g., Ponti et al., 2012). In particular, the variability observed at short timescales imply that the X-ray emission region must be very compact, because the observed variability is governed by the light-crossing time of the source.

Although AGNs have been studied at every available electromagnetic band, X-ray obser-

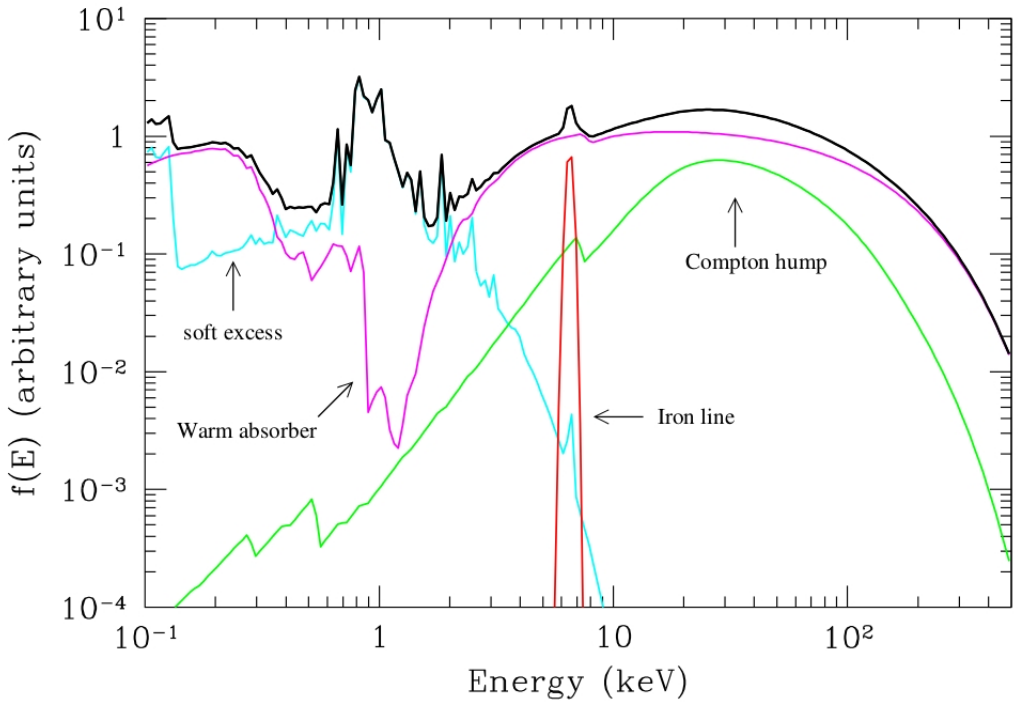

Figure 2.1: The various components of the X-ray SED are shown here. In purple, the power law with a possible warm absorber are shown. In cyan the so-called soft excess, rapidly dropping at $E > 2$ keV. The iron Kα line is marked in red, and the Compton hump, due to reflection of the coronal radiation on the surroundings, is shown in green. The overall SED is the black line. Taken from Risaliti & Elvis (2004).

vations are the most direct probes of the accretion processes responsible for the energy generation, since such radiation is able to penetrate through large columns of obscuring gas and dust, associated with the matter which is located in the surroundings of the AGN. Moreover, as already mentioned, X-rays are generated in the heart of these sources, down to distances within a few gravitational radii ($r_g \equiv GM/c^2$) from the central supermassive black hole. Emission at other wavelenghts, instead, e.g. the continuum optical radiation, is generated at much longer distances, up to 10^5 times farther from the SMBH (e.g., Netzer, 2013).

Finally, Active Galactic Nuclei are also the dominant sources of the X-Ray Background (e.g., Schmidt et al., 1998; Gilli et al., 2007).

2.2 The X-ray spectral features of AGNs

2.2.1 Overview

Many prominent features are present in the X-ray spectra of AGNs. The typical X-ray SED of Active Galactic Nuclei is shown in Fig. 2.1.

Type-1 AGNs, for which we have a direct line of sight towards the central supermassive black hole, are characterized by a power law continuum in the rest-frame band $0.5-10$ keV. The total number of counts can therefore be parametrized as power law functions of the energy of the photon, meaning $N_E \propto E^{-\Gamma}$, where Γ is called the *photon index* of the spectrum. A typical value of $\Gamma \simeq 1.9$ (e.g., Nandra & Pounds, 1994) is usually observed for AGN, although values over the wide range $1.4 \lesssim \Gamma \lesssim 2.3$ are also possible. As we will describe in detail in Sect. 2.2.2. the power law non-thermal spectrum is due to up-Comptonization of accretion disk soft photons by a hot electron plasma, located in a corona above the accretion disk itself.

At energies of $\sim 10 - 40$ keV a broad hump can be seen in many AGNs. This excess of power can be explained with the reflection of photons that are scattered from the corona in the direction of the accretion disk (e.g., Lightman & White, 1988; George & Fabian, 1991; McHardy et al., 1999; Shih et al., 2002). The size of the hump depends on the fraction of radiation that is reflected, which depends on the ionization state of the disk.

Telescopes able to detect hard X-rays, such as INTEGRAL (Clausen & Winkler, 1994), BeppoSAX (Butler & Scarsi, 1991), and more recently Swift (Gehrels et al., 2004) and NuSTAR (Harrison et al., 2013), have discovered that above several tens to hundreds of keV there is an exponential cut-off to the AGN power law extrapolated at lower energies. At very high energies, indeed, the photon energy approaches the electron rest-mass energy (512 keV), therefore photons lose more energy to the electron than they gain and therefore the spectrum becomes significantly steeper.

At energies below 10 keV the spectrum can be modified by obscuring gas by means of photoelectric absorption, if the line of sight passes through the torus, with typical column density for unobscured sources $N_{\rm H} \lesssim 10^{22}$ cm^{-2} (e.g., Turner & Miller, 2009), although some sources (called *Compton-thick*) show column densities as high as $N_{\rm H} \gtrsim 10^{24}$ cm^{-2} (e.g., Matt, 2002; Vignali et al., 2010; Panessa et al., 2016), and often represent the X-ray counterpart of type-2 sources. Sources with $N_{\rm H} \sim 10^{22} - 10^{24}$ cm^{-2} are usually labelled as *obscured Compton-thin* (e.g., Georgakakis et al., 2017). Fig. 2.2 shows how the column density modifies the X-ray spectrum of AGNs.

Some discrete quantum transition are often found in the X-ray band, primarily due to fluorescence. The most common lines that can be found the X-ray AGN spectra are the iron transitions, and in particular the iron Kα emission line at 6.4 keV, which is due to

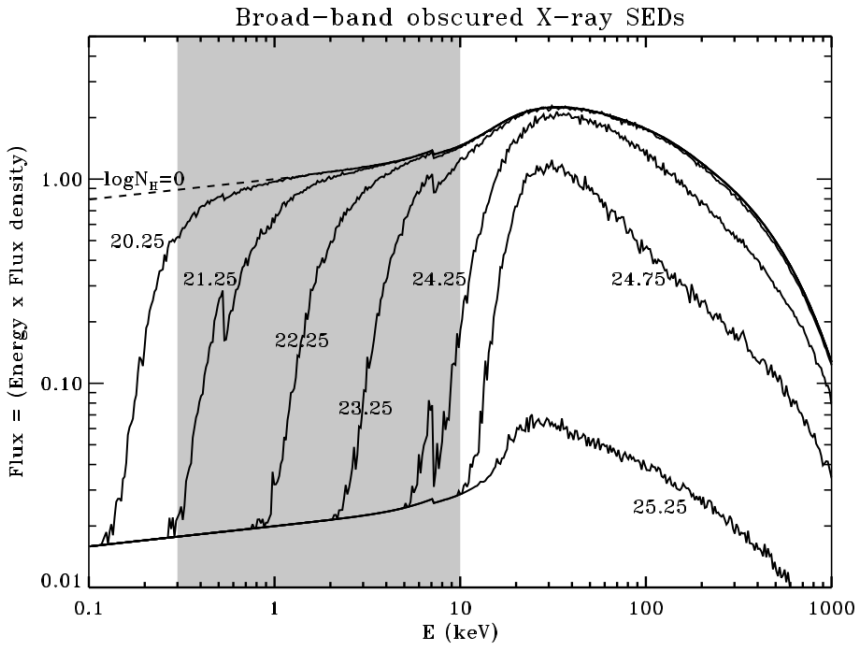

Figure 2.2: Spectral energy distrubutions of AGNs simulated with X-ray spectral analysis code `XSPEC` (Arnaud, 1996) using a typical spectral index of $\Gamma = 1.9$ and various values of $N_{\rm H}$. Taken from Gandhi (2005).

fluorescence, i.e. relaxation after a K-shell photoionization (Osterbrock & Ferland, 2006). Complex absorption features, such as warm absorbers or ultra-fast outflows, due to the presence of ionized material along the line of sight, and additional spectral component such as soft excesses may also be present in some sources.
In the following, we will describe in detail each of these spectral features.

2.2.2 X-ray continuum emission and corona

The current X-ray emission mechanism model was first discussed in the seventies and later reprised by Haardt & Maraschi (1991, 1993); Haardt et al. (1997).
In this model, first introduced to describe the hard X-ray behaviour of Cygnus X-1 (Shapiro et al., 1976), a well studied X-ray binary that involves a stellar mass black hole, and shortly after extended to quasars (Katz, 1976), unsaturated Comptonization of soft photons by a plasma of hot thermal electrons well describes the shape of the observed power law continuum spectra (e.g., Pozdniakov et al., 1976; Sunyaev & Titarchuk, 1980).
According to these pioneering works, the emitted spectrum depends on both the optical depth and the temperature of a hot plasma, and therefore the X-ray emission must happen in two phases.
Haardt & Maraschi (1991) assumed that the release of gravitational energy occurs on a

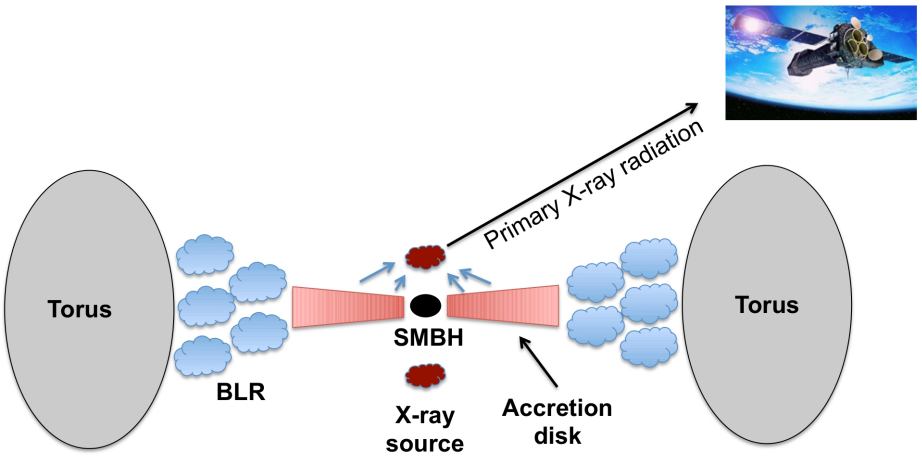

Figure 2.3: Schematic view of the primary X-ray emission. The accretion disk mainly emits optical/UV photons, some of which interact with the corona. By means of up-Comptonization, these photons gain energy, becoming X-rays. These radiation is the primary power law continuum that we detect in the large majority of sources. Image credit: http://www.isdc.unige.ch/~ricci/Website/AGN_in_the_X-ray_band.html

hot, optically thin area, located above a cold, optically thick region, associated with the accretion disk, in which the release of soft UV photons happens. The coexistence of these two phases is possible only if the binding energy is dissipated outside of the accretion disk (Begelman & de Kool, 1991), which can happen if the accretion disk dissipates mainly via magnetic viscosity, with field reconnection in a magnetic corona (Haardt & Maraschi, 1993), such as the one proposed by Liang (1979), that is located above the disk (e.g., Burm, 1986). The two phases are coupled, which means that the cool accretion disk emission provides the soft photon input for the Comptonization, while the hard emission from the corona contributes to the heating of the accretion disk itself. If the fraction of gravitational energy released in the corona is large, the backscattered radiation will be the dominant heating process of the accretion disk.

Many aspects of the corona are not yet fully understood. For example, its geometry is currently unknown, its shape can be a slab, a sphere or even a jet, although rapid variability in the $2-10$ keV band indicates that its size is relatively small (e.g, Ponti et al., 2012; Fabian, 2012). Another source of uncertainty comes from the energy source, that can be either the SMBH spin or the accretion energy. Different disk-corona models have been proposed (e.g., Sincell & Krolik, 1998; Różańska et al., 1999; Kawaguchi et al., 2001), but many problems are still open.

The resulting emission from the corona is therefore a power law, that means that $N_E \propto E^{-\Gamma}$ or, in terms of flux, $F_E \propto E^{1-\Gamma}$. The photon index is usually in the range $1.6-2$, although some sources show lower or higher Γs, which is believed to depend on the coronal

electron temperature kT_e and the optical depth τ. The power law extends to high energies up to a so-called *cut-off energy* E_c, where it does not hold anymore, which is directly related to the coronal temperature by

$$E_c \simeq akT_e, \tag{2.2.1}$$

with a between 2 and 3 (Petrucci et al., 2000, 2001). Coronal cut-offs range in a very wide energy interval, from $E_c \simeq 50$ keV (e.g., Tortosa et al., 2017) up to extreme values such as $E_c \simeq 720$ keV (e.g., Matt et al., 2015), with many different values in between (e.g., Fabian et al., 2015).

2.2.3 X-ray observations of AGN winds: warm absorbers and ultra-fast outflows

As already introduced in Chapter 1, SMBHs play a huge role in the evolution of the host galaxy, since many of its properties, such as the velocity dispersion of stars (e.g., Ferrarese & Merritt, 2000), are correlated with the black hole mass, suggesting that there is some sort of "feedback" mechanism between the black hole and the star formation process (e.g., King & Pounds, 2015, and Sect. 1.4). Since radiation and jets alone are not able to properly describe the complex accretion and outflow cycle, it appears that accretion disk winds are the most suitable candidate for such processes (e.g., Fabian, 2012; Pounds, 2014a; King & Pounds, 2015).

X-ray observations are very important to detect AGN winds, since, as already described in Sect. 2.2.2, they are produced in the innermost parts of the system, very close to the SMBH. This means that X-rays are able to pass though many layers of dense absorbing material, and may retain many information on both the active nucleus and the surrounding environment.

The first evidence of absorbing material in the X-rays was found by Halpern (1984), that reported the presence of soft X-ray absorption, possibly due to a ionized cloud in the line of sight. Such X-ray absorbing features have been commonly named *warm absorbers* (WA). With the advent of the current generation X-ray telescopes, *Chandra* and *XMM-Newton*, it was possible to observe that the WA is composed of narrow absorption lines and edges, from elements in a wide range of ionization stages (e.g., Kaastra et al., 2000; Kaspi et al., 2002; Blustin et al., 2005). These lines and edges appear to be blue-shifted with respect to the source redshift, which means that the material is likely to be outflowing from the central parts of the AGN, with velocities in the range $v \sim 100 - 1000$ km s^{-1} (e.g., McKernan et al., 2007; Gofford et al., 2011; Reeves et al., 2013; Kaastra et al., 2014). WAs are usually detected in the majority of local Seyfert galaxies (e.g., Laha et al.,

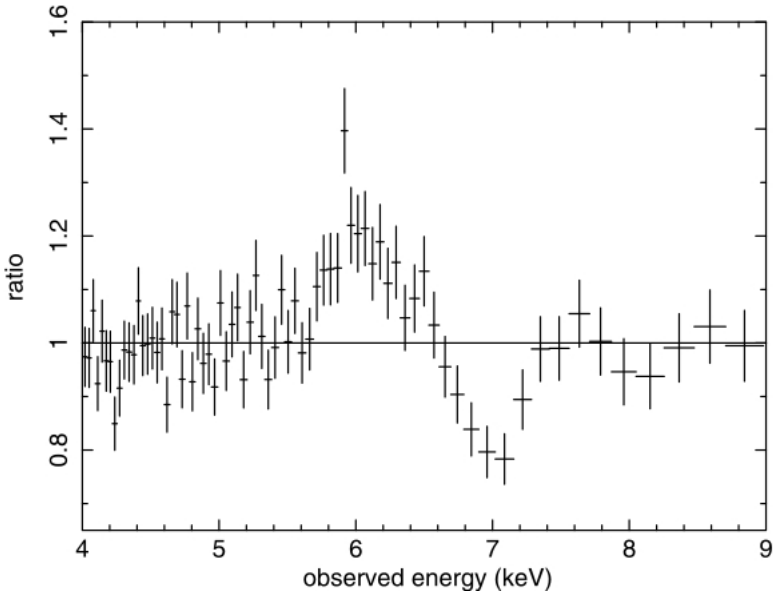

Figure 2.4: Observed P-Cygni profile of the Fe XXV line from XMM-Newton EPIC-pn stacked spectra of the archetypal outflowing source PG 1211+143. The ratio between the spectrum and the overall continuum is shown. Taken from Pounds (2014a).

2014), with ionization parameter in the range $\log \xi \sim 0-2$ erg cm s^{-1} and column density $N_{\rm H} \sim 10^{20} - 10^{22}$ cm^{-2} (e.g., Crenshaw & Kraemer, 2012). It has been suggested that that the WA might be originated in a region outside of the inner disk, likely at distances comparable with the obscuring torus (e.g., Krolik & Kriss, 2001; Blustin et al., 2005).

In addition to WAs, there is another, more extreme, type of outflows in Active Galactic Nuclei, which are commonly known as ultra-fast outflows (UFOs, e.g., Cappi et al., 2009; Tombesi et al., 2010a,b), and are commonly observed through blue-shifted Fe XXV and Fe XXVI absorption lines in the Fe Kα band (e.g., Chartas et al., 2002; Pounds et al., 2003a,b; Tombesi et al., 2010a,b; Giustini et al., 2011; Gofford et al., 2013; Tombesi et al., 2014, 2015; Nardini et al., 2015; Vignali et al., 2015), respectively at $E \simeq 6.69$ keV and $E \simeq 6.96$ keV, as shown in Fig. 2.4. UFOs are very ionized, with ionization parameter that ranges in $3 \lesssim \log \xi \lesssim 6$ erg cm s^{-1}, column densities in the range $N_{\rm H} \sim 10^{22} - 10^{24}$ cm^{-2}, and outflow velocities that can be inferred from the blueshift of Fe XXV and Fe XXVI lines to be in the range $v \sim 0.03c - 0.3c$, with c the speed of light (e.g., Tombesi et al., 2011; Gofford et al., 2013).

Moreover, there have been some detections of fast outflows in the soft X-ray band recently (e.g., Gupta et al., 2013; Pounds, 2014b; Gupta et al., 2015; Longinotti et al., 2015; Reeves et al., 2016), with O VII and O VIII highly blue-shifted lines, suggesting a much lower ionization state with respect to UFOs.

In a study of both UFOs in the Fe Kα band through the Fe XXV/XXVI absorption lines,

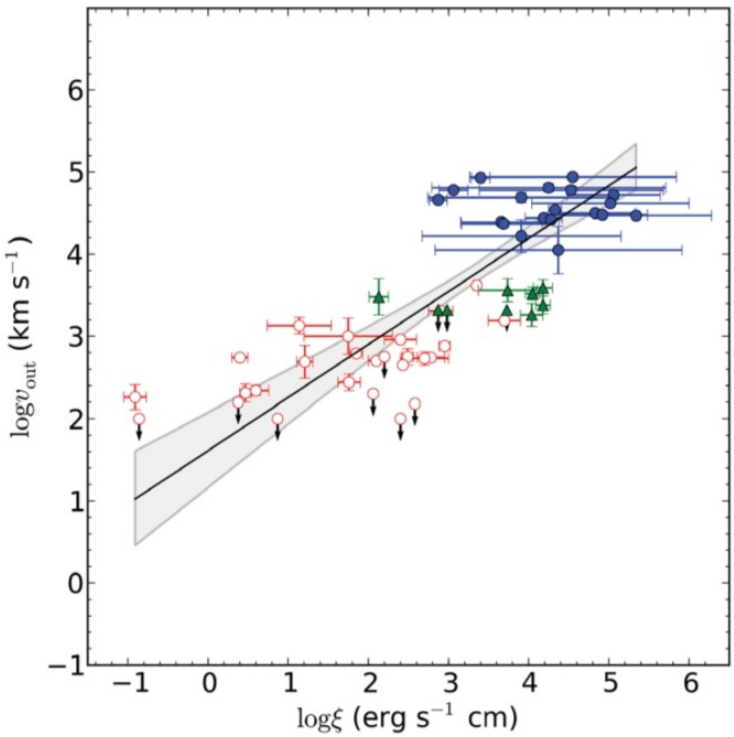

Figure 2.5: Scatter plot of ionization state ($\log \xi$) vs the outflow velocity ($\log v_{\rm out}$). The red dots represent the soft X-ray WAs, while the blue dots are UFOs detected in the Fe Kα band. Green points indicate non-UFO outflows. Arrows indicate upper or lower limits, while the grey band represents the $\pm 2\sigma$ confidence band around the best fitting black line. Taken from Tombesi et al. (2013).

and WAs in the soft X-ray band, for a sample of 35 Seyfert galaxies, Tombesi et al. (2013) found a correlation between the ionization state, column density and velocity with the distance from the black hole: a UFO is therefore closer to the SMBH than the WA. The parameters of the absorbers cover the whole parameter space in a uniform way, with UFOs and WAs always lying at opposite sides of the distribution. This means that these two kinds of absorbers are likely different states of the same large scale outflow structure, that is observed at different distances from the black hole along the line of sight. UFOs are therefore likely launched at relativistic velocities from the inner parts of the AGN, i.e. the inner accretion disk, while the WA is likely to be located at larger distances, comparable with the outer disk or the torus. The correlation between the ionization state $\log \xi$ and the outflow velocity $v_{\rm out}$ is shown in Fig. 2.5.

2.2.4 The Fe Kα line and Compton reflection

As we briefly introduced in Sect. 2.2.1, not all of the detected X-ray radiation is primary radiation coming directly from the corona (Fig. 2.6, left panel).

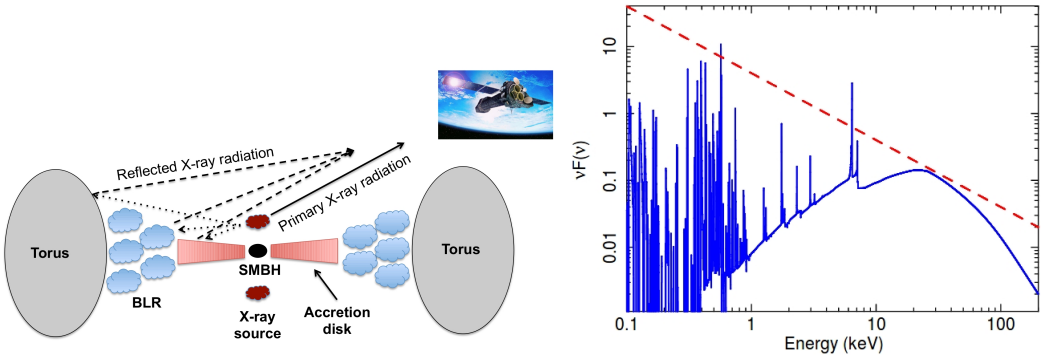

Figure 2.6: *Left.* Schematic view of the superposition of both primary X-ray emission and its reflection on the other parts of the AGN (torus, accretion disk, broad line region etc.) towards the line of sight. Image credit: `http://www.isdc.unige.ch/~ricci/Website/AGN_in_the_X-ray_band.html`. *Right.* Simulated typical reflection spectrum, with a continuum peaking at ~ 30 keV and many lines below 8 keV, the most important of which is the neutral iron Fe Kα emission line at 6.4 keV. Taken from Reynolds et al. (2014)

As a matter of fact, in principle the corona emits isotropically, and any optically thick structure of the active nucleus will be irradiated by the primary emission, which in turn will reflect the radiation, giving rise to a characteristic reflection spectrum, mainly due to Comptonization and photoelectric excitation, followed by Auger de-excitation and fluorescent emission (e.g., Guilbert & Rees, 1988; George & Fabian, 1991; Matt et al., 1991; Fabian et al., 2000).

One of the main features of the reflection spectrum is a prominent continuum, peaking at $\sim 30-40$ keV and a series of emission lines at $E \lesssim 8$ keV, including the most important in AGN X-ray spectroscopy, the Fe Kα emission line at 6.4 keV (Fig. 2.6, right panel), which is the strongest due to the fact that iron is the most abundant metal in the universe, and to the high fluorescence yield, i.e. the number of times an emission event can happen per absorbed photon.

A reflection fraction $\mathcal{R}$ can be defined, as the fraction of reflected flux over the incident one, and can be used as a reliable estimation of the incident angle of the radiation on the reflector ($\mathcal{R} = \Omega/2\pi$, Magdziarz & Zdziarski, 1995).

In addition, the incident radiation is also able to ionize the reflector. For high values of ξ (see Eq. 1.3.11), several elements can produce fluorescence emission lines, especially K emission from iron and its ions at $6.4 \lesssim E \lesssim 7$ keV (e.g., Matt et al., 1997).

Normally, the Fe Kα line is narrow, even though its profile might be broadened by relativistic effects. For instance, the iron line might be produced in the inner parts of the accretion disk, where relativistic Doppler effect and gravitational redshift are important, and alter the shape of the line. In particular, in such cases, the line assumes a double-peaked shape, with a "blue" (more energetic) peak, corresponding to the line being emitted by material from the approaching side of the disk, and a "red" peak, associated with the receding part of the disk. The gravitational redshift broadening is usually called "red wing" (see

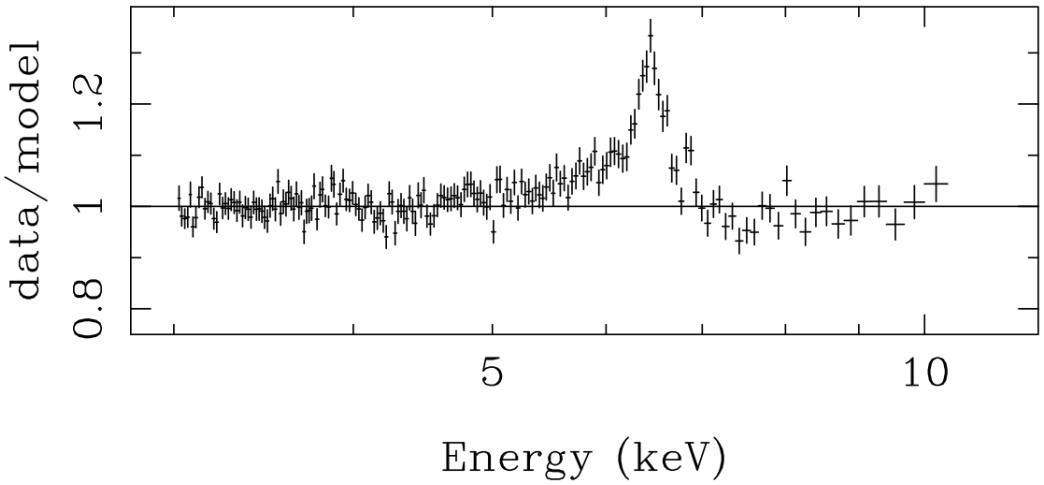

Figure 2.7: XMM-Newton spectrum of MCG-6-30-15, well known for the presence of a prominent red wing. The broadening at lower energies is clearly visible at $E \sim 5 - 6.4$ keV, and it is likely due to gravitational redshift in the innermost parts of the disk, that are closer to the black hole because the BH spin is very high ($a \simeq 0.99$, Brenneman & Reynolds, 2006). Image taken from Vaughan & Fabian (2004).

Fig, 2.7). If the SMBH spin is high, and spinning in the same direction as the accretion disk ($a \sim +0.99$), it is believed that the innermost stable orbit (ISCO) of the accretion disk is smaller and makes these effects larger (Brenneman & Reynolds, 2006).

2.2.5 Soft excess

Below 1 keV, the soft X-ray spectra of Active Galactic Nuclei often show a marked rise in flux, with respect to the flux extrapolated from the higher energy spectrum, the so-called *soft excess* (e.g., Turner & Pounds, 1989), particularly frequent in Seyfert 1 galaxies (Boller et al., 1996).

The soft excess is often modelled with black body models, with best fits in the range $kT \sim 0.01 - 0.20$ keV (e.g., Czerny et al., 2003; Piconcelli et al., 2005). Even though this temperature is too high and cannot be from the inner disk, it might represent Compton-scattered disk photons (e.g., Czerny & Elvis, 1987). Gierliński & Done (2004), however, found that the temperature range is too narrow for such a large range of black hole masses ($\log M/M_{\odot} \sim 6 - 8$).

Many possible explanations have been proposed in the past, including relativistic blurring of absorption features that are less opaque in the soft X-ray band (Gierliński & Done, 2004), several layers of unblurred absorption (Miller et al., 2008), or, for obscured AGN, radiative recombination continuum with higher order resonant scattering transitions (Guainazzi & Bianchi, 2007), but at present no clear physical explanation of the soft excess is widely accepted.

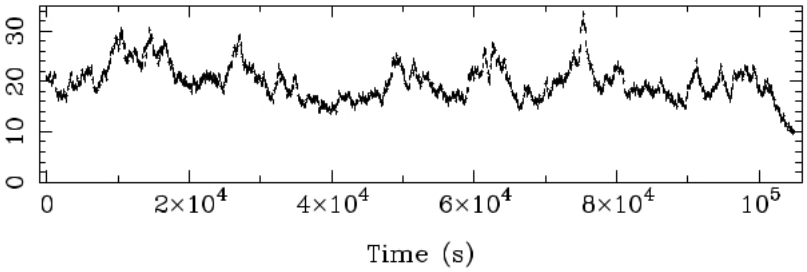

Figure 2.8: EPIC-pn full band ($0.2 - 10$ keV) light curve of Mrk 766. Taken from Vaughan & Fabian (2003).

2.3 Amplitude variability

As discussed in Sect. 1.6, Active Galactic Nuclei are variable in nearly every electromagnetic band.

In the X-ray band, variability may occur at shorter timescales than the optical or any other band (e.g., Ponti et al., 2012), which means that the emitting corona must be much smaller than the emitting region of other kinds of radiation.

Many studies on light curves (see Fig. 2.8) of nearby single sources have been made (e.g., Uttley et al., 2002; Uttley & McHardy, 2005). Usually, low-luminosity AGNs appear to be more variable than high-luminosity sources (e.g., Barr & Mushotzky, 1986; Lawrence & Papadakis, 1993; Green et al., 1993; Nandra et al., 1997). The variability amplitude, moreover, is larger at longer timescales than at shorter ones (e.g., Markowitz & Edelson, 2004) and it has been suggested by Paolillo et al. (2004) that it might increase with redshift, although recent results by Shemmer et al. (2017) indicate no increasing X-ray variability with redshift.

Some works have extended these kind of study to larger samples with wider ranges of luminosity and redshift (e.g., Almaini et al., 2000; Manners et al., 2002; Paolillo et al., 2004) or ensemble analyses based on the structure function (e.g., Vagnetti et al., 2011, 2016), confirming a strong anti-correlation of the variability with the X-ray luminosity L_{X}. Recent surveys (e.g., Shemmer et al., 2017; Zheng et al., 2017) confirm this trend.

Many variability models have been proposed in the past, including a single coherent oscillator (e.g., Almaini et al., 2000), a flare or hot spot-related origin (e.g., Lehto, 1989; Abramowicz et al., 1991; Czerny et al., 2004), or variability due to the superposition of absorbing or reflecting material along the line of sight (e.g., Abrassart & Czerny, 2000; Miniutti & Fabian, 2004; Chevallier et al., 2006).

Moreover, X-ray variability is related to UV variability, with the UV trailing the X-rays (e.g., Shemmer et al., 2001; Mason et al., 2002), or viceversa the X-ray variability trailing UV (e.g., Arévalo et al., 2005) with time delays of the order of days. In the first case

the relation might be due to the disk-corona relationship, in which the UV photons are up-Comptonized by the corona (see Sect. 2.2.2 and Haardt & Maraschi, 1991). In the latter case, the corona might irradiate X-rays on the accretion disk, that are reprocessed into thermal optical emission (Collin-Souffrin, 1991). A useful instrument to investigate on this topic is the X-ray/UV ratio $\alpha_{\rm ox}$ (e.g., Sobolewska et al., 2009; Vagnetti et al., 2010; Lusso & Risaliti, 2016), defined as

$$\alpha_{\rm ox} = 0.3838 \log \left[\frac{L_{\rm X}(2\ {\rm keV})}{L_{\rm UV}(2500\text{Å})} \right], \tag{2.3.2}$$

whose variability is found to increase as a function of time lag (e.g., Vagnetti et al., 2010). This means that, while both optical and X-ray amplitude variability both increase with the time lag, so does their ratio, which means that, on longer timescales, variability is dominated by the optical disk emission.

2.4 Spectral variability

In addition to amplitude variability, it is also interesting to study the spectral variability as well, i.e. the variations of the spectral shape.
As already discussed in Sect. 1.6.1, many authors have studied the spectral variability in the UV/optical band (e.g., Giveon et al., 1999; Trèvese & Vagnetti, 2002; Vagnetti et al., 2003), where a hardening of the spectrum is usually observed for brighter phases of the AGN ("harder when brighter" behaviour).
In the X-ray band, spectral variability has been mostly analyzed for single sources (e.g., Magdziarz et al., 1998; McHardy, 2001; Zdziarski et al., 2003), often during a single observation (e.g., Ursini et al., 2016) while not many ensemble studies have been made on the topic, such as Sobolewska & Papadakis (2009).
These studies have found that the X-ray spectrum has quite the opposite, "softer when brighter", behaviour, in individual and ensemble studies, at both softer and higher (Soldi et al., 2014) energies. The opposite "harder when brighter" behaviour was instead found by Emmanoulopoulos et al. (2012) and Connolly et al. (2016). The authors found that LLAGNs with extremely low Eddington ratio ($L/L_{\rm bol} \lesssim 0.01$) behave differently from their high-luminosity counterparts, in similarity with the hard state of X-ray binaries (XRB). According to Connolly et al. (2016), at such low luminosities, the accretion flow is "advection-dominated" (ADAF) and the UV radiation from the disk is too faint to be the dominant seed photon source for the corona, and this role is taken over by higher-energy cyclo-synchrotron seed photons, produced by the corona itself, which result in a harder

Compton-scattered spectrum when the flux is larger (Esin et al., 1997).
These studies are mainly focused on nearby Seyfert galaxies, and few studies have dealt with the X-ray spectral variability of type 1 quasars in a larger luminosity and redshift range, with the notable exceptions of the already mentioned work by Paolillo et al. (2004), and Gibson & Brandt (2012), who both found softer spectra at brighter phases.
The observed X-ray spectral variability might have several possible origins, that have been proposed in the past. The simplest possible explanation is that the observed variations of the photon index Γ are due to intrinsic variations of the continuum slope (e.g., Haardt et al., 1997; Coppi, 1999). According to this thermal Comptonization model, intrinsic X-ray spectral changes respond to the variations of UV seed photons. There has been evidence, though, that the observed photon index $\Gamma_{\rm obs}$ may be due to the superposition of different spectral features varying in different ways. For instance, the spectrum may be composed by a power law continuum, variable in amplitude only, and by reflection component, which is constant (e.g., McHardy et al., 1999; Shih et al., 2002; Taylor et al., 2003; Ponti et al., 2006; Miniutti et al., 2007). It is not excluded that a variable power law slope, combined with a constant reflection, are present. A third possibility is that the power law has constant slope, but complex variations of some absorbers (column density, ionization state, covering factor...) generate the observed spectral variations (e.g., Turner & Miller, 2009).
Since the softer when brighter behaviour is seen in most of the sources with $L/L_{\rm Edd} > 0.01$, it is believed that the mechanism responsible, whichever it is, is the same for all the sources.

Chapter 3

DATA

3.1 XMM-Newton

3.1.1 The satellite

XMM-Newton is an X-ray space observatory, that was launched on December 10, 1999, following a proposal originally made in 1982.
The spacecraft weights 4 tons, it is 10 m long and it is composed by two payload modules, connected by a long carbon fibre tube (see Fig. 3.1). One of these modules is the Focal Plane Assembly, which contains the two high-resolution Reflection Grating Spectrometers (RGS, Den Herder et al., 2001), the EPIC (European Photon Imaging Camera) pn-CCD camera (Strüder et al., 2001), with angular resolution of 15″ half-energy width (HEW) at 1.5 and 8 keV, and energy resolution of $\sim$ 100 eV at $E = 2$ keV, depending on window mode and distance from the focal point, and two EPIC MOS imaging detectors (Turner et al., 2001), with same angular resolution as the pn camera, but slightly better energy resolution ($\sim$ 80 eV at $E = 2$ keV). The other one is the Service Module and it contains the majority of the spacecraft sub-systems, the Optical Monitor (OM) instrument (Mason et al., 2001), astrometry equipment capable of absolute measurement accuracy of 4 arcsec half-cone angle, and the three X-ray Mirror Modules.
The most important improvement of XMM-Newton with respect of the previous X-ray detectors is the large collecting area (grazing angle ranging between 17 and 42 arcmin), which is made possible by the peculiar design of the three X-ray modules, consisting of 58 coaxial and confocal (Aschenbach et al., 1986) mirrors.
In order to allow a simpler way to cool down the X-ray cameras (see Jansen et al., 2001, for further details), the satellite was placed in a very eccentric orbit, with perigee at

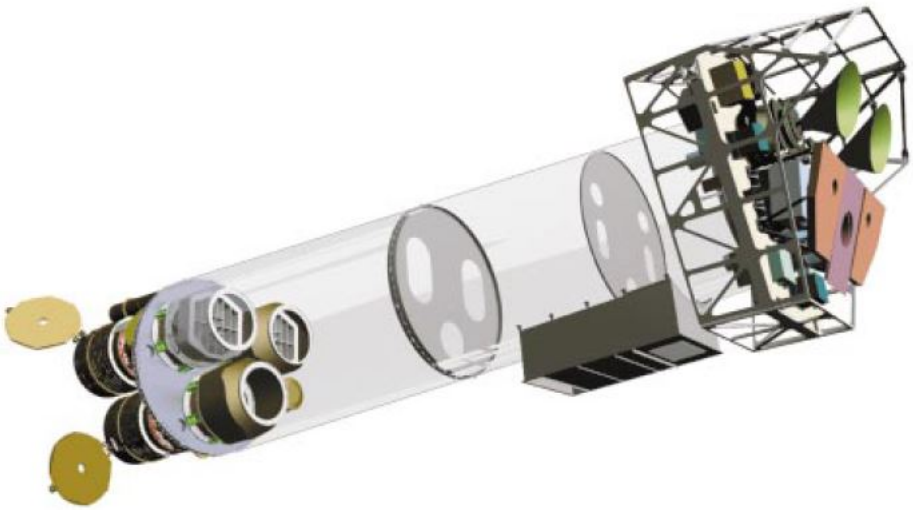

Figure 3.1: Rough schematics of the XMM-Newton observatory. On the left the three mirror X-ray telescopes are visible. Taken from Jansen et al. (2001).

7 000 km and apogee at 114 000 km. The orbital period is approximately 48 hours. Given the fact that the orbit is so eccentric, some parts of it are cointained within the radiation belt, giving rise to high background periods when the altitude is $\lesssim 60\,000$ km. Therefore, operations are limited above this altitude. However, all the elements of the observatory are designed to prevent a significant amount of damaging photons to reach the instruments, even during periods with the highest background.

3.1.2 The XMM-Newton Serendipitous Source Catalogue

The large collecting area of the EPIC X-ray cameras aboard XMM-Newton (~ 1500 cm^2 at 1.5 keV for each camera), and especially the very large field of view ($30'$ in full window mode), upt to hundreds of X-ray sources can be detected with a single pointing (serendipitous detections), most of which may be newly discovered objects.
The XMM-Newton Serendipitous Source Catalogue (XMMSSC) is a catalogue that lists each of these detections.
Since the energy of the photons detectable by XMM-Newton is in $0.2 - 12$ keV, the XMMSSC provides its data in several sections of this band. The small bands are:

- Band 1: $0.2 - 0.5$ keV
- Band 2: $0.5 - 1$ keV
- Band 3: $1 - 2$ keV

- Band 4: $2 - 4.5$ keV
- Band 5: $4.5 - 12$ keV

but wide bands, compositions of these small ones, are also used:

- Band 6 (soft band): $0.2 - 2$ keV
- Band 7 (hard band): $2 - 12$ keV
- Band 8 (full band): $0.2 - 12$ keV
- Band 9 (XID band): $0.5 - 4.5$ keV

Among the various quantities contained in the catalogue, XMMSSC lists coordinates, observation information (OBSIDs, window mode, source number in the observation etc.), hardness ratios between small bands, and most importantly count rates and fluxes at each desired band (except bands 6 and 7).
The catalogue also makes distinction between extended and point-like sources.
Detailed information on the data analysis tools and calibration procedure used to create the catalogue can be found in Watson et al. (2009).
The versions of the XMMSSC that are used in this thesis are the 3XMM-DR5[1] (Rosen et al., 2016), that is made up of 565 962 observations of 396 910 unique sources, and its update 3XMM-DR6[2], with 678 680 observations of 468 440 unique sources. During the writing of this dissertation, 3XMM-DR7[3] was released.

3.2 Sloan Digital Sky Survey

The Sloan Digital Sky Survey (SDSS, Stoughton et al., 2002) is a multi-filtering spectroscopic and imaging survey. A large 2.5 m telescope is dedicated to it, located at the Apache Point Observatory in New Mexico (USA). Five filters are used by this telescope, in bands U, G, R, I, and Z (*ugriz*, Fukugita et al., 1996). This mission is able to cover a very large fraction of the whole sky.
The SDSS-I and SDSS-II projects (York et al., 2000) took extensive data that was collected in several data release, including the last, SDSS-DR7 (Abazajian et al., 2009), taken during three huge observational campaigns: the *Sloan Legacy Survey*, that stored information

[1] http://xmmssc.irap.omp.eu/Catalogue/3XMM-DR5/3XMM_DR5.html
[2] http://xmmssc.irap.omp.eu/Catalogue/3XMM-DR6/3XMM_DR6.html
[3] http://xmmssc.irap.omp.eu/Catalogue/3XMM-DR7/3XMM_DR7.html

on $\sim$ 930 000 galaxies, 120 000 quasars and 225 000 stars, the *Sloan Extention for Galactic Understanding and Extrapolation* (SEGUE-1), with new spectra of $\sim$ 240 000 stars, and the *Sloan Supernova Survey*, that discovered about 500 type Ia supernovae in about three months.
The following mission, SDSS-III (Eisenstein et al., 2011) started observations in 2008 and all its data are available in the twelfth data release, SDSS-DR12 (Alam et al., 2015). SDSS-III carried out four main observational campaigns: the *Baryon Oscillation Spectroscopic Survey* (BOSS), that mapped the spatial distribution of luminous red galaxies and quasars (Dawson et al., 2013), SEGUE-2, the *APO Galactic Evolution Experiment* (APOGEE), aimed at understanding the structure of the Milky Way with high-resolution infrared spectroscopy, and the *Multi-object APO Radial Velocity Exoplanet Large-area Survey* (MARVELS), pointed at nearby stars to look for evidence of the presence of exoplanets.
Starting in 2014, the fourth Sloan campaign, SDSS-IV[4], started taking data with four main campaings: APOGEE-2, eBOSS, dedicated to the survey of galaxy and quasars at cosmological distances, and *Mapping Nearby Galaxies at APO* (MaNGA), aimed at obtaining resolved spectroscopy for 10 000 nearby galaxies.
The data concerning quasars is collected into dedicated data releases: SDSS-DR7Q[5] (Schneider et al., 2010), containing all quasars detected by SDSS-I and SDSS-II, and SDSS-DR12Q[6] (Pâris et al., 2017), with all the quasars from SDSS-III. The two catalogues are complementary, although some superposition is present, due to multiple detection of some sources in both SDSS-I/II and SDSS-III.

3.3 The MEXSAS catalogues

The XMMSSC contains all types of astronomical sources (Lin et al., 2012), both extragalactic and galactic, from isolated neutron stars, magnetars, to microquasars, X-ray binaries and AGNs.
In order to select quasars we created the *Multi-Epoch XMM Serendipitous AGN Sample* (MEXSAS, Vagnetti et al., 2016). This sample was created by cross-matching the 3XMM-DR5 with the two latest Sloan Digital Sky Survey catalogs, SDSS-DR7Q and DR12Q (see Sect. 3.1.2 and 3.2). These two optical/UV catalogues list respectively 105 783 and 297 301 quasars, according to slightly different definitions. Indeed, DR7Q defines a quasar as an object with absolute magnitude in the I-band $\mathcal{M}_I \leq -22$ (Schneider et al., 2010), while

[4] http://www.sdss3.org/future
[5] http://classic.sdss.org/dr7/products/value_added/qsocat_dr7.html
[6] http://www.sdss.org/dr12/algorithms/boss-dr12-quasar-catalog/

in the DR12Q all sources with $\mathcal{M}_I \leq -20.5$ are selected (Pâris et al., 2017), therefore including some low-z Seyfert galaxies. Moreover, radio-loud AGNs and BALQSOs are also found in the sample. (see Sect. 4.4.3). Sources in both DR7Q and DR12Q were counted only once, in such cases we adopted the more recent redshift measurements from DR12Q. A second version of MEXSAS (MEXSAS2, Vagnetti et al., 2018) was created when 3XMM-DR6 was released. It contains 9 735 X-ray observations of 3 366 quasars. Thanks to the release of virial mass estimates for SDSS-DR12Q sources (Kozłowski, 2017a), and the already available catalogue for the SDSS-DR7Q catalogues (Shen et al., 2011), we were able to include a mass and luminosity estimate for each source. We used homogeneous criteria to determine M and $L_{\rm bol}$ from the two catalogs. In fact, Shen et al. (2011) used Hβ for $z \leq 0.7$, Mg II for $z \leq 1.9$ and C IV at higher redshifts, with similar options for bolometric luminosities. Kozłowski (2017a), instead, preferred the use of Mg II black hole mass when available, since the C IV is biased from various effects.
To apply the same criteria for both DR7Q and DR12Q we took the estimates of Kozłowski (2017a) for quasars included only in DR12Q and not in DR7Q (2 178 objects), while for quasars included in DR7Q, regardless of their presence in DR12Q, we adopted the masses by Shen et al. (2011) in case only one broad line is present (442 objects). In case the quasar is included in DR7Q and two broad lines are present, we applied the Kozłowski (2017a) criteria to the DR7Q data, deriving new estimates (518 objects).

3.4 Single sources

As we will show in Chapter 4, the spectral variability analysis of the MEXSAS catalogue entries is based on an approximate derivation of the photon index. We also derived photon indices for a selection of 9 sources, by performing accurate spectral fits, in order to apply the same analysis method by using both approximate and accurate Γs, and then compare the results (Serafinelli et al., 2018a and Chapter 5). We extracted a sample of 94 archival XMM-Newton EPIC-pn spectra, publicly available from the satellite science archive (XSA[7]).
We chose the same sources that were studied by Sobolewska & Papadakis (2009) in *Rossi X-ray Timing Explorer* (RXTE) data, selecting only those for which more than 4 observations are available in the XMM-Newton archive, in order to avoid meaningless correlations due to scarsity of points. This excludes NGC 3227 (2 observations) and NGC 3783 (3) and includes Ark 564 (11), Fairall 9 (5), MCG-6-30-15 (8), Mrk 766 (8), NGC 3516 (6), NGC 4051 (17), NGC 5506 (8) and NGC 5548 (17). We only take into account observations that are longer than ~ 10 ks, excluding calibration observations with low S/N spectra.

[7] http://nxsa.esac.esa.int/nxsa-web

Source	$N_{\rm obs}$	$\log M_{\rm BH}/M_\odot$	$\log L_{\rm bol}$ (erg s^{-1})	$\log L_{\rm bol}/L_{\rm Edd}$	z
Ark 564	11	6.41^a	44.69^b	-0.13	0.025
Fairall 9	5	8.41^c	45.23^d	-1.29	0.047
M81	13	7.80^e	41.74^e	-4.17	$7 \cdot 10^{-4*}$
MCG-6-30-15	8	6.65^f	44.28^f	-0.48	0.008
Mrk 766	8	6.82^g	43.60^h	-1.33	0.013
NGC 3516	6	7.50^i	44.16^j	-1.45	0.009
NGC 4051	17	6.11^e	42.80^e	-1.42	0.002
NGC 5506	9	7.94^k	44.52^l	-1.53	0.006
NCG 5548	17	7.59^m	44.45^n	-1.25	0.017
PG 1114+445	12	8.77^o	45.74^o	-1.14	0.144

Table 3.1: List of sources studied in this thesis, in alphabetical order. For each source we list the number of epochs, the black hole mass $M_{\rm BH}$, the bolometric luminosity $L_{\rm bol}$, the Eddington ratio $L_{\rm bol}/L_{\rm Edd}$ and the redshift z. The reference for the source parameters are: (*a*) Botte et al. (2004), (*b*) Romano et al. (2002), (*c*) Peterson et al. (2004), (*d*) Woo & Urry (2002), (*e*) Xu (2011), (*f*) McHardy et al. (2005), (*g*) from the reverberation mapping catalogue in Bentz & Katz (2015), using $f \sim 4.3$, (*h*) Winter et al. (2012), (*i*) Denney et al. (2010), (*j*) Crenshaw & Kraemer (2012), (*k*) Papadakis (2004), (*l*) Uttley & McHardy (2005), (*m*) Pancoast et al. (2014), (*n*) Vasudevan et al. (2010), (*o*) Shen et al. (2011). All Eddington ratios were computed from black hole masses and bolometric luminosities using $L_{\rm Edd} \simeq 1.26 \cdot 10^{38}\, M/M_\odot$. All redshifts are taken from the NASA/Ipac Extragalactic Database (NED). * This redshift is not actually measured, because the measure of the Doppler shift is dominated by blueshift due to the local motion of the galaxy, deviating from the Hubble flow; it was computed using $z = H_0 D/c$, with $D \simeq 3.6$ Mpc.

In addition, we also selected 13 observations of nearby LLAGN M81, which spectrum was found to follow a harder when brighter trend (Connolly et al., 2016), possibly due to a change in dominant seed photon source.

We also studied type-1 quasar PG 1114+445 (Serafinelli et al., 2018b and Chapter 6), for which we retrieved 12 observations.

The complete list of sources is found in Table 3.1, with references for masses and luminosities, with redshifts taken from the NASA/Ipac Extragalactic Database (NED[8]).

[8] https://ned.ipac.caltech.edu/

Chapter 4

ENSEMBLE X-RAY SPECTRAL VARIABILITY OF QUASARS

The spectral variability parameter β in Eq. 1.6.19 is easily adaptable to describe the spectral variability in the X-ray band. Since the photon index Γ is related to the spectral index α by $\Gamma = 1 - \alpha$ it can be redefined as

$$\beta = -\frac{\Delta\Gamma}{\Delta \log F_{\rm X}}, \tag{4.0.1}$$

in a given X-ray band X.
We want to compute an ensemble β for the MEXSAS sample, but it is a subsample of the XMM-Newton serendipitous catalogue, that does not include the photon index Γ. In order to compute Eq. 4.0.1 we can either estimate β by means of the hardness ratios (Serafinelli et al., 2016), as described in the Sect. 4.1, or estimate the value of Γ from the flux values in the catalogue and then use it to compute β in Eq. 4.0.1 (Serafinelli et al., 2017b), as shown in Sect. 4.2.

4.1 Hardness ratios analysis

Given a "hard" band H and a "soft" band S, the *hardness ratio* HR is usually defined as

$$\mathrm{HR} = \frac{\mathrm{CR_H} - \mathrm{CR_S}}{\mathrm{CR_H} + \mathrm{CR_S}}, \tag{4.1.2}$$

where CR_i is the count-rate in the band i.

	Slope	r
$\Delta\mathrm{HR}_1$ vs $\Delta \log F_1$	-0.380 ± 0.008	-0.508
$\Delta\mathrm{HR}_2$ vs $\Delta \log F_2$	-0.409 ± 0.008	-0.507
$\Delta\mathrm{HR}_3$ vs $\Delta \log F_3$	-0.388 ± 0.011	-0.384

Table 4.1: Results of the HR$-\log F$ fits in bands $1-3$. r is the Pearson correlation coefficient.

The XMM-Newton Serendipitous Source Catalogue lists four hardness ratios: HR_1 is computed between the count-rates in bands 1 and 2, HR_2 is computed between bands 2 and 3, HR_3 between bands 3 and 4, while HR_4 is computed between bands 4 and 5.
The hardness ratios can be related to β:

$$\frac{\Delta \mathrm{HR}}{\Delta \log F} \simeq \frac{d\mathrm{HR}}{d\Gamma}\frac{\Delta\Gamma}{\Delta \log F} = -\beta\frac{d\mathrm{HR}}{d\Gamma}, \tag{4.1.3}$$

where we have used Eq. 4.0.1. Therefore the spectral variability parameter can be expressed as:

$$\beta = -\left(\frac{\Delta \mathrm{HR}}{\Delta \log F}\right)\left(\frac{d\mathrm{HR}}{d\Gamma}\right)^{-1}. \tag{4.1.4}$$

The numerator of Eq. 4.1.4 can be easily approximated with a linear fit between HR and $\log F$ in the chosen band. Since the band 4 is affected by great errors, we only report such fits in bands $1-3$ (see Fig. 4.1). Given the fact that we are studying an ensemble, we perform the fits between the deviations from the source mean value of both HR and $\log F$. The numerical values of such fits are reported in Table 4.1.
The denominator can be computed analytically in case of a pure power law spectrum, in which case we will have $F_\nu = F_0\nu^{1-\Gamma}$. Given two bands, a hard band H defined between ν_{H_1} and ν_{H_2}, and a soft band S defined between ν_{S_1} and ν_{S_2}, the two integrated fluxes will be

$$F_\mathrm{H} = F_0\int_{\nu_{\mathrm{H}_1}}^{\nu_{\mathrm{H}_2}} \nu^{1-\Gamma}d\nu = \frac{F_0}{2-\Gamma}\left(\nu_{\mathrm{H}_2}^{2-\Gamma} - \nu_{\mathrm{H}_1}^{2-\Gamma}\right),$$

$$F_\mathrm{S} = F_0\int_{\nu_{\mathrm{S}_1}}^{\nu_{\mathrm{S}_2}} \nu^{1-\Gamma}d\nu = \frac{F_0}{2-\Gamma}\left(\nu_{\mathrm{S}_2}^{2-\Gamma} - \nu_{\mathrm{S}_1}^{2-\Gamma}\right),$$

for $\Gamma \neq 2$. If $\Gamma = 2$ we have $F_{\mathrm{H,S}} = F_0 \ln\frac{\nu_{\mathrm{H,S}_2}}{\nu_{\mathrm{H,S}_1}}$.
The count-rate is related to the flux by $\mathrm{CR}_i = k_i F_i$, in a given band i. This coefficients k_i depend on the band and the camera of the telescope, and can be retrieved online by using the `WebPIMMS`[1] tool. Since the count-rate of the pn camera is dominant (i.e. k_i of

[1] https://heasarc.gsfc.nasa.gov/cgi-bin/Tools/w3pimms/w3pimms.pl

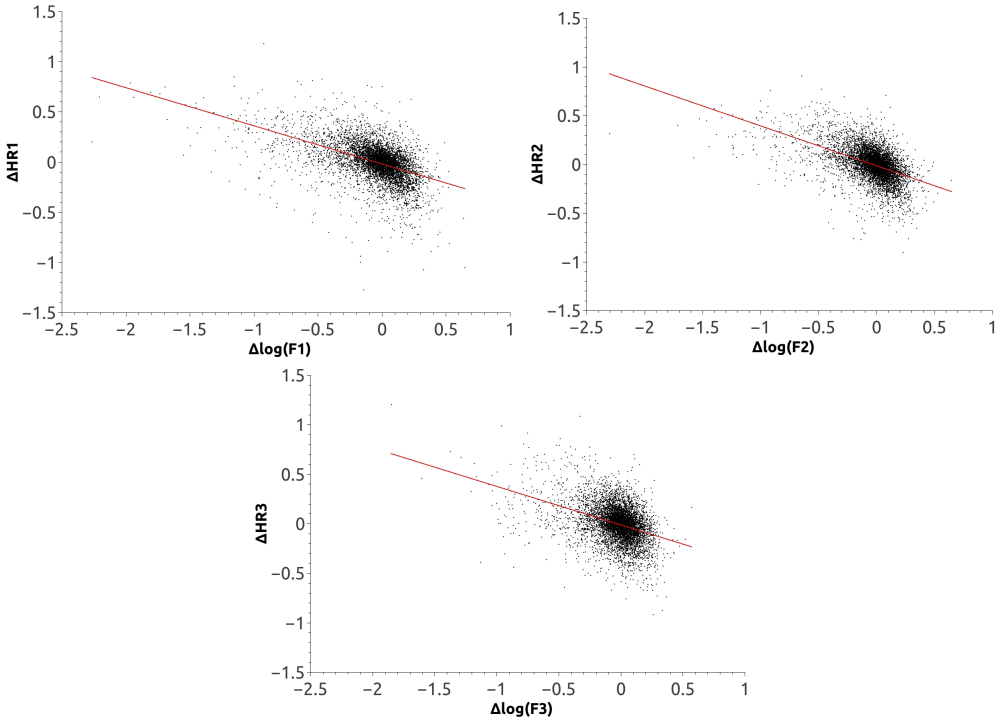

Figure 4.1: The three linear fits of $\Delta\mathrm{HR}_1$ vs $\Delta \log F_1$ (top left), $\Delta\mathrm{HR}_2$ vs $\Delta \log F_2$ (top right), and $\Delta\mathrm{HR}_3$ vs $\Delta \log F_3$ (bottom) are shown. All three bands show an anticorrelation between $\Delta\mathrm{HR}_i$ and $\Delta \log F_i$.

the pn camera is much larger than the k_i of the two MOS cameras, by a factor of ~ 6, Rosen et al., 2016), we approximated the EPIC k_i with the pn k_i. The hardness ratio will then be

$$\mathrm{HR} = \frac{k_\mathrm{H}\left(\nu_{\mathrm{H}_2}^{2-\Gamma} - \nu_{\mathrm{H}_1}^{2-\Gamma}\right) - k_\mathrm{S}\left(\nu_{\mathrm{S}_2}^{2-\Gamma} - \nu_{\mathrm{S}_1}^{2-\Gamma}\right)}{k_\mathrm{H}\left(\nu_{\mathrm{H}_2}^{2-\Gamma} - \nu_{\mathrm{H}_1}^{2-\Gamma}\right) + k_\mathrm{S}\left(\nu_{\mathrm{S}_2}^{2-\Gamma} - \nu_{\mathrm{S}_1}^{2-\Gamma}\right)},$$

and therefore

$$\frac{d\mathrm{HR}}{d\Gamma} = 2k_\mathrm{H}k_\mathrm{S}\frac{\nu_{\mathrm{H}_2}^{2-\Gamma}\nu_{\mathrm{S}_2}^{2-\Gamma}\ln\frac{\nu_{\mathrm{S}_2}}{\nu_{\mathrm{H}_2}} + \nu_{\mathrm{H}_2}^{2-\Gamma}\nu_{\mathrm{S}_1}^{2-\Gamma}\ln\frac{\nu_{\mathrm{H}_2}}{\nu_{\mathrm{S}_1}} + \nu_{\mathrm{H}_1}^{2-\Gamma}\nu_{\mathrm{S}_2}^{2-\Gamma}\ln\frac{\nu_{\mathrm{H}_1}}{\nu_{\mathrm{S}_2}} + \nu_{\mathrm{H}_1}^{2-\Gamma}\nu_{\mathrm{S}_1}^{2-\Gamma}\ln\frac{\nu_{\mathrm{S}_1}}{\nu_{\mathrm{H}_1}}}{\left[k_\mathrm{H}\left(\nu_{\mathrm{H}_2}^{2-\Gamma} - \nu_{\mathrm{H}_1}^{2-\Gamma}\right) + k_\mathrm{S}\left(\nu_{\mathrm{S}_2}^{2-\Gamma} - \nu_{\mathrm{S}_1}^{2-\Gamma}\right)\right]^2}. \tag{4.1.5}$$

This quantity is strictly positive. Given that the linear fits between $\Delta\mathrm{HR}$ and $\Delta \log F$ are all negative, Eq. 4.1.4 will return a negative value of β. This means that, in case of power law spectrum, the trend will be softer when brighter.

If one wants to take absorption into account, some spectra can be generated for various

values of the neutral column density $N_{\rm H}$ and the photon index Γ, using the software `XSPEC` (Arnaud, 1996). Also in the presence of absorption, we find $d\mathrm{HR}/d\Gamma > 0$, which means that the sample follows a softer when brighter trend also in the presence of possible undetected neutral absorbers.
This method, though, is only able to give an estimate on the sign of β, since it is dependent on the photon index. Since we are trying to quantify the spectral variability and not only assess its trend, we need a way to estimate Γ from the catalogue, as described in the next section.

4.2 Photon index estimation

In the following, we will give an estimate of the photon index Γ. Since the XMMSSC sample lists five fluxes, the idea is to assume a pure power law X-ray spectrum and perform linear spectral fits between $\log F_E$ and $\log E$ for each observation, in order to have one value of Γ for every epoch.
The available fluxes in the serendipitous catalogue are not monochromatic, though, since they are integrated fluxes in the five XMM bands: F_1 is integrated between 0.2 and 0.5 keV, F_2 between 0.5 and 1 keV, F_3 in $1-2$ keV, F_4 in $2-4.5$ keV and finally F_5 in the band $4.5-12$ keV. Such fluxes are derived assuming $\Gamma = 1.7$ as described in detail in Rosen et al. (2016).
In the reasonable scenario in which the spectrum has a pure power law shape within the band, the integrated flux in a band $\nu_1 - \nu_2$, that we will call $F_{\rm X}$, can be calculated as a function of the monochromatic flux in ν_1, the two frequencies and the photon index, as follows:

$$F_{\rm X} = \int_{\nu_1}^{\nu_2} F_{\nu_1} \left(\frac{\nu}{\nu_1}\right)^{1-\Gamma} d\nu = \frac{F_{\nu_1}\nu_1}{2-\Gamma}\left[\left(\frac{\nu_2}{\nu_1}\right)^{2-\Gamma} - 1\right], \tag{4.2.6}$$

for $\Gamma \neq 2$. If we convert frequencies in energies, $E = h\nu$, we can invert Eq. 4.2.6 and obtain the expression of the monochromatic flux in the left extreme E_1 of the band X:

$$F_{E_1} = \frac{hF_{\rm X}\,(2-\Gamma)}{E_1\left[\left(\frac{E_2}{E_1}\right)^{2-\Gamma} - 1\right]}, \tag{4.2.7}$$

where h is the Planck constant, that in useful units becomes $h = 4.14 \cdot 10^{-18}$ keV Hz^{-1}, if E_1 is expressed in keV.
To compute F_{E_1} in Eq. 4.2.7 we assumed a typical photon index $\Gamma_0 = 1.7$, which best

represents the bulk of the sources in the XMM-Newton Serendipitous Source Catalogue (see Rosen et al., 2016 and Mateos et al., 2009).

Once we have F_{E_1}, we are able to compute the linear fits between $\log F_{E_1}$ and $\log E_1$ for $E_1 = 0.2, 0.5, 1, 2, 4.5$ keV, to obtain the actual photon index Γ and its error $\sigma(\Gamma)$. In order to gain precision, we used these Γs to compute F_{E_1} again, this time using a more accurate photon index than Γ_0 in Eq. 4.2.7. Another iteration does not substantially change the values of Γ, and therefore we stop iterating.

We stress that the flux errors differ substantially from band to band and from epoch to epoch. Also, considering that the fits are performed in a small number of spectral points, it is crucial that we weight the fits by using

$$w_{E_1} = \frac{1}{\sigma^2 \left(\log F_{E_1}\right)}$$

as weights, where $\sigma\left(\log F_{E_1}\right)$ is the error associated with $\log F_{E_1}$. In this way, we give less significance to the points that deviate from the pure power law with remarkable errors.

The MEXSAS sample is mainly composed by type-1 objects, but a moderate neutral absorption could still be present. This absorption, however, cannot be taken into account in this analysis, because our computation of Γ is only possible assuming a pure power law spectrum. However, this absorption only affects the softest XMM band for $\log N_{\rm H} \lesssim 21.5$ (see Fig. 2.2) at low redshifts. If we exclude the lowest energy point from our calculation, performing therefore linear fits on the remaining four points ($E_1 = 0.5, 1, 2, 4.5$ keV), we remove any systematic effect due to deviation from power law, from absorption with $\log N_{\rm H} \lesssim 21.5$ at zero redshift, and even with higher values of the column density at higher redshifts. At relatively high redshifts, this approximation works better, since we do not expect extremely high values of the column density in type-1 sources, while at low redshifts some absorption due to column densities higher than $10^{21.5}$ cm^{-2} might still be present. However, the effect is heavily reduced and we are mainly interested in the variations of Γ more than its absolute value, and therefore we neglect any possible residual systematic effect due to absorption.

In order to check the validity of this method, we checked our Γs against the XMMFITCAT spectral catalogue[2] by Corral et al. (2015), in which the authors computed Γ from full spectra, with various models, including absorbed powerlaw, for a limited subset of the 3XMM-DR5 catalogue, made up by observations with a high number of EPIC net counts ($N \geq 50$). We created a subsample of coincident data between MEXSAS and XMMFITCAT, consisting of 2 002 observations of 707 sources. Not every observation is well fitted by a simple absorbed power law model. Corral et al. (2015) flag each spectral

[2] http://xraygroup.astro.noa.gr/Webpage-prodec/thecatalog.html, recently updated to include data from 3XMM-DR5.

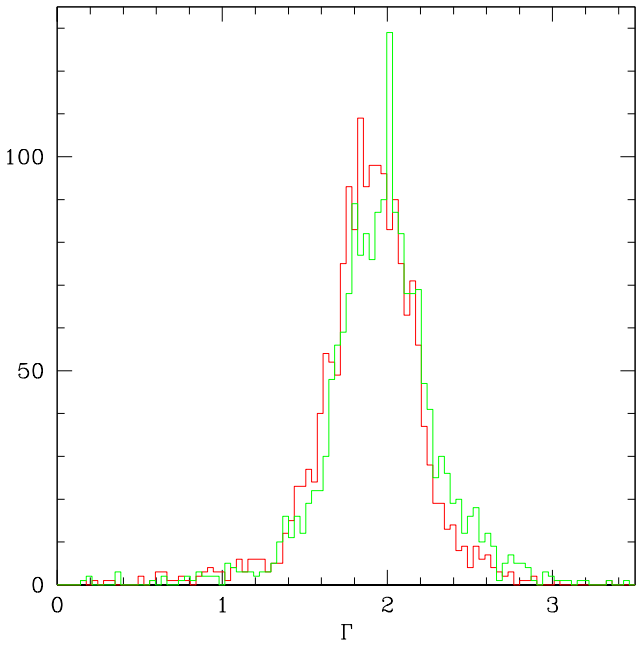

Figure 4.2: Comparison between the values we obtained for the photon index and the ones obtained by Corral et al. (2015) on the coincident data subset. The green histogram is the distribution of `WAPO_GAMMA` in the XMMFITCAT sample, while the red histogram is the distribution of Γ computed with our method.

fit: a spectral fit is considered "good" if the `goodness` function in `XSPEC` returns a value lower than 50%. 90% of the observations satisfy this condition for the absorbed power law spectral fit (labelled `WAPO`). Therefore we only select this subsample, consisting of 1 771 observations of 630 unique sources, and we compared our Γs with the `WAPO_GAMMA` entry of XMMFITCAT, which is the value of Γ obtained assuming a simple model with pure power law with intrinsic absorption. In this coincident subsample, the average number of EPIC net counts is $N \simeq 100$. The comparison between the two distribution can be seen in Fig. 4.2, and as can be seen, the two distributions of photon indices are quite similar, with a very small difference between the mean values ($\langle \texttt{WAPO\_GAMMA} \rangle - \langle \Gamma \rangle \simeq 0.07$), suggesting that our method is robust, even computing Γ from four spectral points instead of computing them with proper spectral fits.

Our pure power law approximation does not represent the actual spectral shape of the sources. Additional components, such as soft excess, the possible presence of a relativistic red wing on the Fe Kα line, or photoionized absorbers might have a role in the calculation of Γ. However, we do not have any reason to believe that the percentage of sources with such spectral features on the whole MEXSAS sample is any different from the subsample of coincident data between MEXSAS itself and XMMFITCAT. Therefore the incidence of these cases is estimated to be around 10% of the total. We also assume that the effect of these phenomena is statistically negligible for the ensemble analysis, since we are mainly

interested in Γ variations. This is clearly not valid for single sources, though, since the presence of such spectral features is crucial in the computation of β (see Sect. 4.5).

4.3 Ensemble result

Once the photon index is computed, in principle, one does not need to compute the hardness ratio to calculate β, but it can be computed directly using Eq. 4.0.1, by performing linear fits between Γ and $\log F$.

We need to decide which flux band best represents the spectral variability. Many authors (e.g., Paolillo et al., 2004) use typical soft ($0.5-2$ keV) and hard ($2-10$ keV) bands. The ideal choice for spectral variability studies would be the hard band $F_{\rm H}$, since it is not affected by soft excesses and warm absorbers. Unfortunately, this band is highly affected by large errors (Rosen et al., 2016), especially for faint sources, and it is suitable only for nearby bright sources (see Chapter 5). Therefore, we computed the soft flux $F_{\rm S}$ in the band $0.5-2$ keV, which is the sum of bands EP2 and EP3. Following the procedure explained in Watson et al. (2009), $F_{\rm S}$ is given by:

$$F_{\rm S} = W_{\rm pn,S}F_{\rm pn,S} + W_{\rm m1,S}F_{\rm m1,S} + W_{\rm m2,S}F_{\rm m2,S}, \tag{4.3.8}$$

where $F_{\rm cam,S} = F_{\rm cam,2} + F_{\rm cam,2}$ is the sum of the fluxes in bands EP2 and EP3 received by a given camera cam=pn,m1,m2. The weights are given by

$$W_{\rm cam,S} = \frac{\sigma^{-2}\left(F_{\rm cam,S}\right)}{\sigma^{-2}\left(F_{\rm pn,S}\right) + \sigma^{-2}\left(F_{\rm m1,S}\right) + \sigma^{-2}\left(F_{\rm m2,S}\right)}, \tag{4.3.9}$$

where $\sigma(F_i)$ is the error associated to a given flux F_i. With analogous calculations, we are also able to compute the hard ($2-12$ keV) flux $F_{\rm H}$ as the sum of bands 4 and 5. We will use the hard band in Chapter 5.

For a given individual source, the spectral variability parameter β can be obtained with good approximation by a linear fit between Γ and $\log F_{\rm S}$. That is not true for the ensemble case, in which we are comparing sources with different average photon indices and X-ray fluxes. In the ensemble case, thus, instead of computing the $\Gamma - \log F_{\rm S}$ linear fits, we compute the linear fit between the deviations of Γ from the mean value of the source ($\Delta\Gamma = \Gamma - \overline{\Gamma}$), and the deviations of the flux logarithm from its mean value ($\Delta \log F_{\rm s} = \log F_{\rm S} - \overline{\log F_{\rm S}}$). Changing the sign of the linear fit slope, according to Eq. 4.0.1, this gives:

$$\beta = -0.69 \pm 0.03. \tag{4.3.10}$$

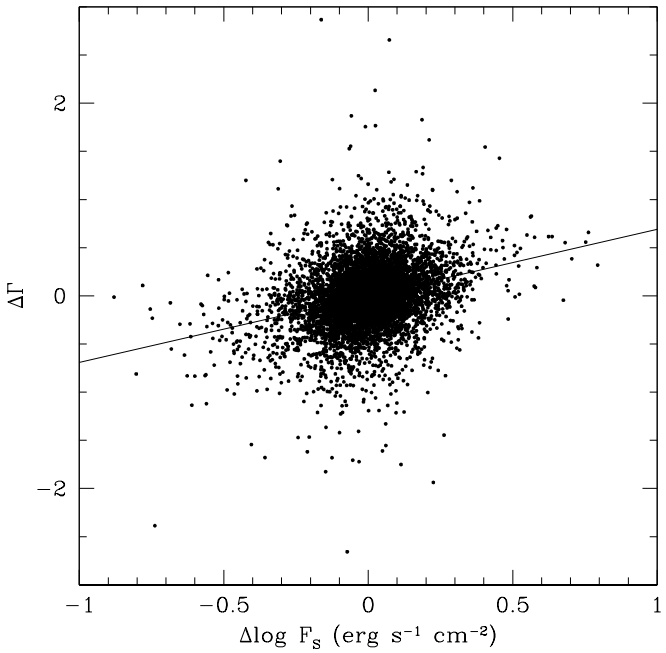

Figure 4.3: Ensemble correlation between $\Delta\Gamma$ and $\Delta \log F_S$ for the whole MEXSAS sample. The line represents the best fit. The positive correlation indicates a negative β according to Eq. 4.0.1 and therefore the softer when brighter trend already found with the hardness ratios is confirmed.

The Pearson correlation coefficient is $r_0 = 0.293$. We also compute the probability of finding such correlation by chance, which, for a high number of points (we tested its validity for $N \gtrsim 50$, see Sect. 4.5), is given by (Press et al., 1986)

$$p(r > r_0) = \mathrm{erfc}\left(\frac{|r_0|\sqrt{N}}{\sqrt{2}}\right), \tag{4.3.11}$$

where $\mathrm{erfc}(x)$ is the complementary error function of x, N is the number of points in the sample, and r_0 the computed correlation coefficient. For $N \lesssim 50$ another expression for the probability is needed (see Sect. 4.5). Using the definition given by Eq. 4.3.11 we obtain a probability $p < 10^{-10}$ of finding the ensemble correlation by chance. This small value indicates that the correlation, although small, is significant.

In order to raise the significance of the data, we defined a better subsample, by eliminating the worst observations, which means those ones with $\sigma(\Gamma) > 0.5$. This subsample discards 1 245 observations, and leaves us with 6 592 epochs of 2 309 unique sources. We found a very similar value of the spectral variability parameter ($\beta = -0.68 \pm 0.02$) and therefore, given the little statistical difference between the two sets, we will use the whole sample rather than this subset.

We also want to compare β for the coincident subsample between MEXSAS and XMMFIT-

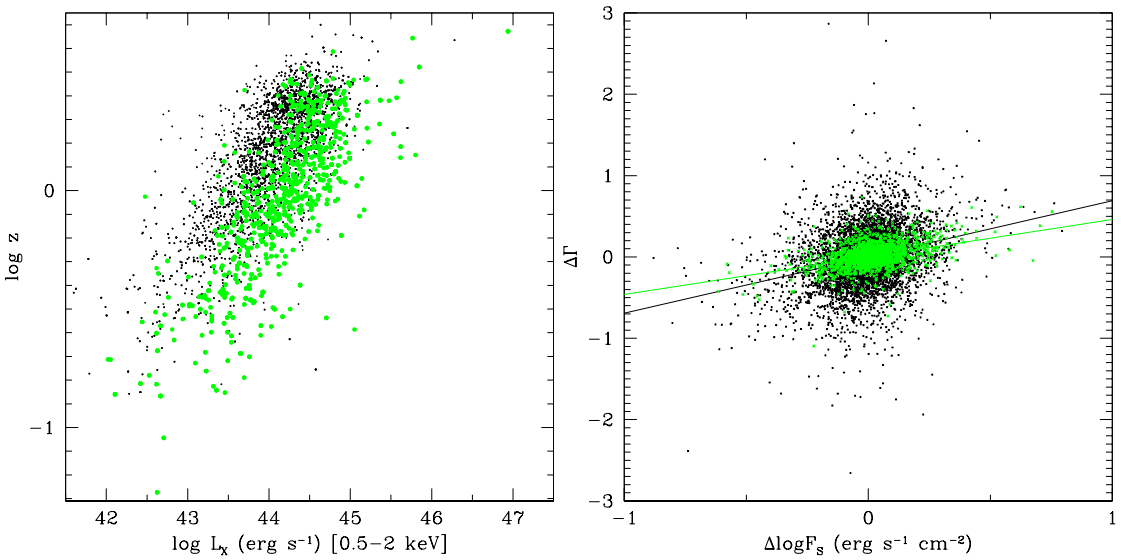

Figure 4.4: *Left.* Relation between the redshift z and the X-ray luminosity L_{X}. *Right.* $\Delta\Gamma - \Delta \log F_{\mathrm{S}}$ correlation plotted using photon indices from our analysis, computed as described in Sect. 4.2. In both figures, the green subset represents all observations from the sources that are present in both the MEXSAS and XMMFITCAT catalogues, while the black dots represents epochs that are only present in MEXSAS and not in the sample by Corral et al. (2015).

CAT (see Sect. 4.2), in order to further validate the consistency of our computing method, using both Γ as computed in Sect. 4.2 and the `WAPO_GAMMA` entry of the XMMFITCAT catalogue, representing the photon indices obtained by assuming an absorbed power law model for the spectra. Using our photon indices we obtain $\beta = -0.46 \pm 0.02$, while computing Eq. 4.0.1 using Γs computed by Corral et al. (2015) gives $\beta = -0.46 \pm 0.04$. This is another evidence that our calculation of Γ is solid and represents a good approximation of the actual photon index of the spectrum.

This value of β is lower than the one derived using Eq. 4.3.10. As shown in Fig. 4.4, since the XMMFITCAT consists of observations with a high number of counts, it is made up by brighter sources. This could mean that the spectrum of brighter sources is less variable than the spectrum of the fainter ones.

To investigate this possible effect, we divided our sample into four bins of source-averaged flux $\langle F_{\mathrm{S}} \rangle$ (see Table 4.2). The first bin includes extremely faint sources, from $\langle F_{\mathrm{S}} \rangle = 4.26 \cdot 10^{-16}$ erg cm^{-2} s^{-1} to $\langle F_{\mathrm{S}} \rangle = 5 \cdot 10^{-15}$ erg cm^{-2} s^{-1}; the second bin includes all sources with $5 \cdot 10^{-15} \leq \langle F_{\mathrm{S}} \rangle < 10^{-14}$ erg cm^{-2} s^{-1}; the third includes the sources with $10^{-14} \leq \langle F_{\mathrm{S}} \rangle < 2.5 \cdot 10^{-14}$ erg cm^{-2} s^{-1}; while the fourth bin includes the brightest sources of the sample, from $\langle F_{\mathrm{S}} \rangle = 2.5 \cdot 10^{-14}$ erg cm^{-2} s^{-1} up to the highest value of $\langle F_{\mathrm{S}} \rangle = 4.3 \cdot 10^{-12}$ erg cm^{-2} s^{-1}. As shown in Table 4.2, the spectral variability parameter β decreases in absolute value with the average flux, showing that brighter sources are less variable than fainter ones. However, brighter sources also have smaller values of the

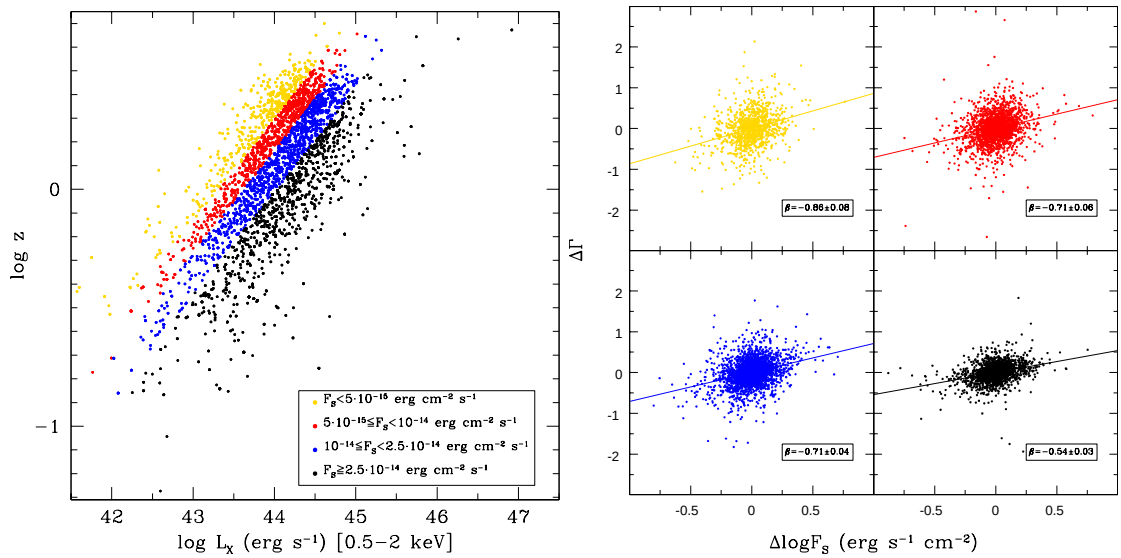

Figure 4.5: *Left.* Relation between the redshift z and the X-ray luminosity L_X for the four flux bins. The color legend is also shown. *Right.* $\Delta\Gamma - \Delta \log F_S$ correlation for the same four flux bins. The slopes are all positive and decrease with increasing mean fluxes. The correlation coefficients are all around $r \sim 0.3$ and all the probabilities of finding such correlations by chance are negligible, $p < 10^{-10}$. See Table 4.2 for details

$\langle F_S \rangle_{min}$	$\langle F_S \rangle_{max}$	N_{sour}	N_{obs}	$\beta \pm \sigma(\beta)$	$\langle \sigma(\Gamma) \rangle$	r_0
$4.26 \cdot 10^{-16}$	$5 \cdot 10^{-15}$	401	1039	-0.86 ± 0.08	0.37	0.295
$5 \cdot 10^{-15}$	10^{-14}	729	1923	-0.71 ± 0.06	0.33	0.261
10^{-14}	$2.5 \cdot 10^{-14}$	963	2689	-0.71 ± 0.04	0.25	0.317
$2.5 \cdot 10^{-14}$	$4.30 \cdot 10^{-12}$	715	2186	-0.54 ± 0.03	0.16	0.329

Table 4.2: List of four $\langle F_S \rangle$ flux bins with spectral variability parameter $\beta \pm \sigma(\beta)$, number of sources N_{sour}, number of observations N_{obs} and correlation coefficient r_0. A column showing the average error of Γ in each bin is also shown, which indicates that fainter sources also have average larger errors on the photon index Γ. The bins at higher fluxes have a smaller absolute value of β, which means their spectrum is less variable, but higher correlations are found for these sources. All probabilities $p\,(r > r_0)$ of finding these correlations by chance are found to be smaller than 10^{-10}.

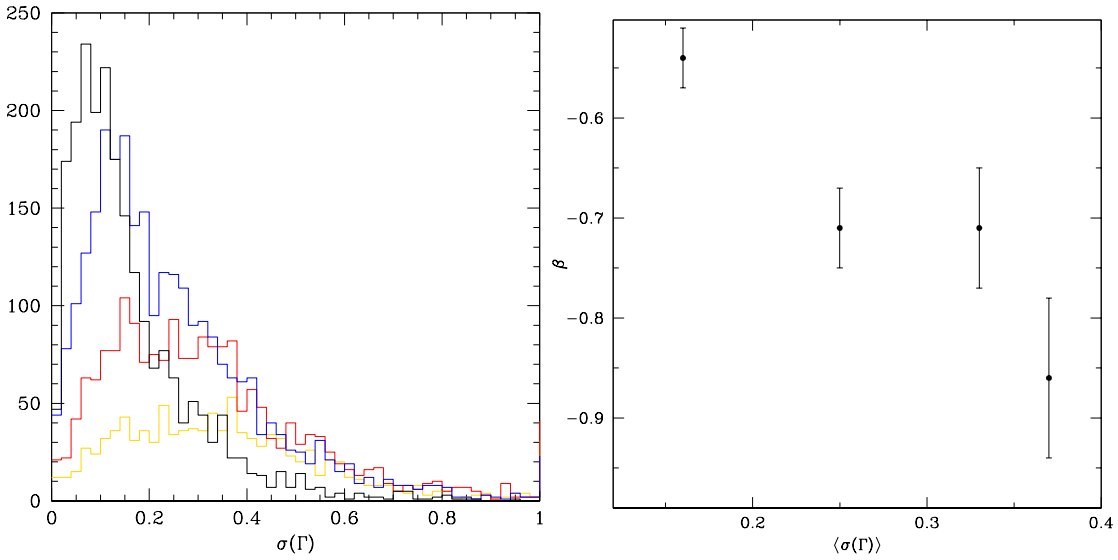

Figure 4.6: *Left.* The distribution of the error of Γ for the four flux bins defined in Table 4.2. The brightest sources (black) have a distribution narrowly peaked at small values of $\sigma(\Gamma)$, with a small incidence of high-error observations, while the faintest (yellow) distribution of $\sigma(\Gamma)$ is flatter and with larger incidence from high-error data. *Right.* The decrease of β with $\sigma(\Gamma)$, which is larger for fainter sources is shown.

average Γ error, $\langle\sigma(\Gamma)\rangle$, whose value in the lowest flux bin is more than double the one for the highest flux bin. This means that β increases in absolute value for fainter sources due to a systematic effect, since the photon indices in fainter sources have larger average errors. This is due to the fact that the distribution of errors on Γ is narrowly peaked at low errors for the brightest bin, while it is flatter for the lowest flux bins (see Fig. 4.6).
It must be stressed that these ensemble values of β represent how the spectra of the sources in the sample vary with flux on average, but individual sources may deviate significantly from these ensemble values. A negative value of β indicate a global softer when brighter trend, but this does not mean that there cannot be sources with the opposite, harder when brighter, trend, showing non-negative values of β. We did not find such sources among the most correlated ones of the MEXSAS catalogue (see Sect. 4.5), but we will return on this topic in Chapter 5.
Finally, we compare these results with an approximation of β that we estimated by means of the structure function (SF) computation for the same sample in different bands (Vagnetti et al., 2016), namely bands EP1 ($0.2-0.5$ keV), EP2 ($0.5-1$ keV), EP3 ($1-2$ keV) and EP4 ($2-4.5$ keV). We neglect band EP5 ($4.5-12$ keV) because of the already mentioned great errors that affect it, which makes it less reliable. Given that the bands are relatively narrow, the photometric errors are very important at short timelags ($\Delta t \lesssim 30$ days). As shown in Fig. 4.7, the variability decreases from EP1 to EP3, with a more complex behaviour for EP4. We averaged the SF in $100 \leq \Delta t \leq 1000$ days, where it is definitely larger than the error contribution, for bands EP1 to EP3, while we did not

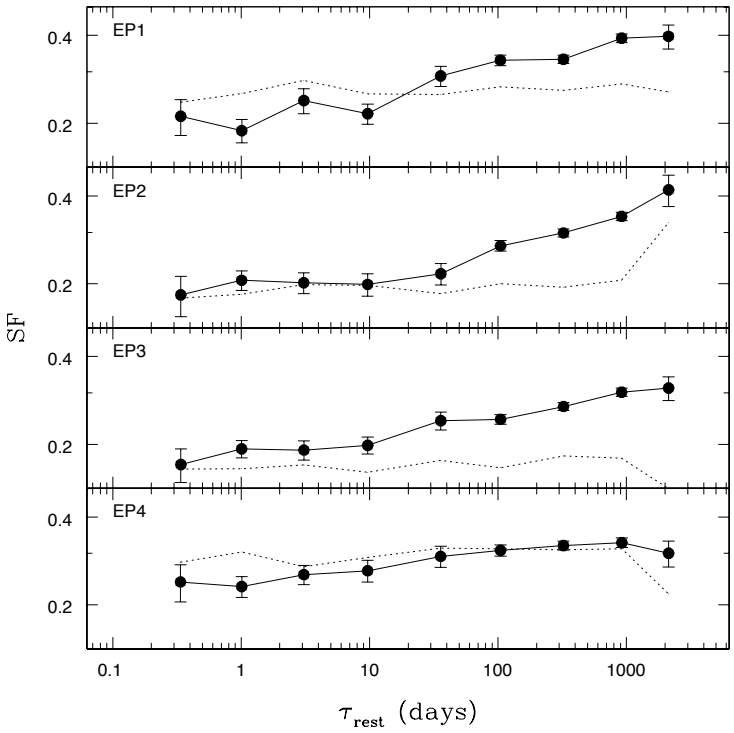

Figure 4.7: Structure function for the XMM-Newton bands EP1 ($0.2-0.5$ keV), EP2 ($0.5-1$ keV), EP3 ($1-2$ keV) and EP4 ($2-4.5$ keV). The contribution of the photometric error, which has been subtracted from the SF, is shown as a dotted line. The variability is decreasing for increasing energy in bands 1 to 3, hinting at a softer when brighter behaviour.

consider band EP4, where this condition does not hold (see Fig. 4.7). We find that the SF depends on the emission frequency ν by

$$\log \mathrm{SF} = A - B \log \nu, \tag{4.3.12}$$

with $A = 2.06 \pm 0.15$ and $B = 0.15 \pm 0.01$. Once a given variation of the photon index is given, the SF varies at different frequencies as $\delta\mathrm{SF} = -\Delta\Gamma \cdot \delta \log \nu$. (Vagnetti et al., 2016) From Eq. 4.0.1 we have $\Delta\Gamma = -\beta \cdot \Delta \log F \simeq -\beta \cdot \mathrm{SF}$. Thus, we have $\delta\mathrm{SF} = \beta \cdot \mathrm{SF}\delta \log \nu$ and therefore:

$$\frac{\delta \log \mathrm{SF}}{\delta \log \nu} \simeq \frac{1}{\delta \log \nu} \log e \cdot \frac{\delta \mathrm{SF}}{\mathrm{SF}} = \beta \log e. \tag{4.3.13}$$

Combining Eqs. 4.3.12 and 4.3.13 we obtain

$$\beta \simeq \log e \cdot \frac{\delta \log \mathrm{SF}}{\delta \log \nu} \simeq -0.35 \pm 0.02. \tag{4.3.14}$$

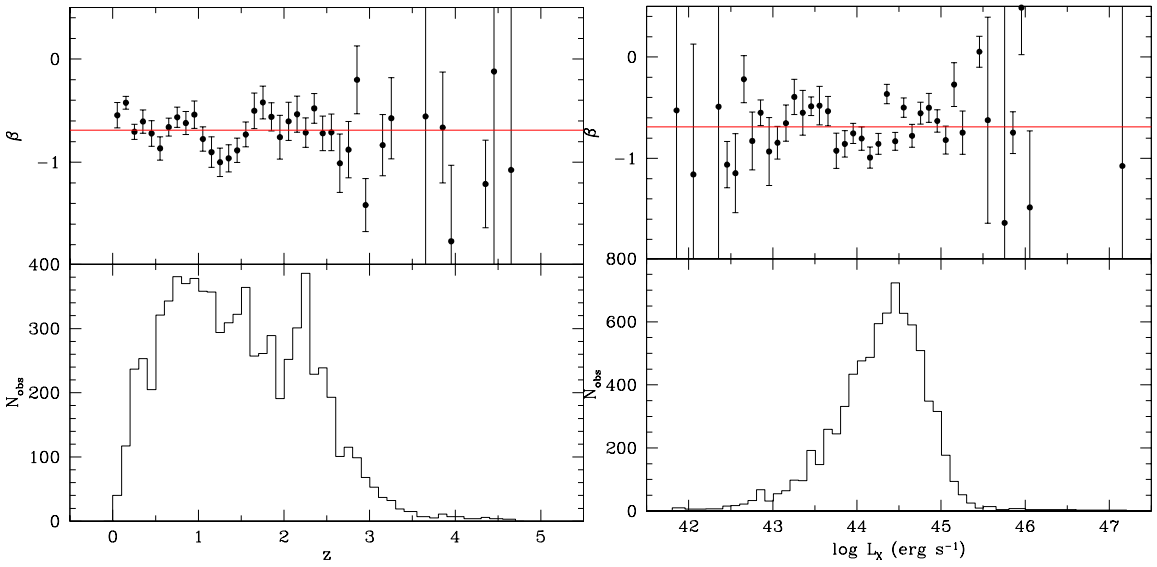

Figure 4.8: *Top.* Dependence of β on redshift (left) and $2-10$ keV X-ray luminosity (right). The red line represents the ensemble value $\beta = -0.69$. No clear trend on either z or $\log L_{\rm X}$ is found, although some bins present significant deviations. *Bottom.* Histograms of the redshift (left) and X-ray luminosity (right) bins in the $2-10$ keV band. The errors on the top figure are related to the number of points included in the bin.

Considering that β in Eq. 4.3.14 is obtained by using an approximate method, performed using just parts of the SF ($100-1000$ days) in narrow bands with high photometric errors due to a small number of counts, this estimate roughly agrees with β directly computed with linear fits, using photon indices and a larger flux band.

4.4 Dependence on physical parameters

As described in Chapter 3, the MEXSAS sample is highly heterogeneous. Different sources might have different spectral properties and hence different spectral variability. In this section we investigate how this properties influence the spectral variability parameter β, and we want to find if there are possible dependences from source parameters such as redshift, X-ray luminosity, black hole mass or Eddington ratio.

4.4.1 Redshift and X-ray luminosity

Both Sloan Digital Sky Survey (SDSS) quasar catalogues DR7Q and DR12Q list the redshift z of each source, obtained by optical spectroscopy of SDSS spectra.
We divided our sample in redshift bins of width $\delta z = 0.1$, and for each bin we computed the ensemble β.

As shown in the left panel of Fig. 4.8, β does not appear to depend on the redshift. The number of points for each bin drastically drops below $\sim 10^2$ for $z \gtrsim 2.8$. Since the error on β is dependent on the number of points of the set in which the linear fit is computed, all βs above such point have greater errors and therefore are less reliable.
As shown in Fig. 4.4 and 4.5, there is a strong correlation between redshift and the X-ray luminosity $L_{\rm X}$.
Neither SDSS catalogues nor 3XMM-DR5 include the X-ray luminosity of each source. Assuming a cosmology with $H_0 = 70$ km s^{-1} Mpc^{-1}, $\Omega_\Lambda = 0.7$ and $\Omega_{\rm m} = 0.3$, we compute the luminosity distance of each source as follows:

$$D_{\rm L}(z) = \frac{c}{H_0}\,(1+z)\int_0^z \frac{dz}{\sqrt{\Omega_{\rm m}\,(1+z)^3 + \Omega_\Lambda}}, \tag{4.4.15}$$

which is used to compute the X-ray luminosity as e.g., Ryden (2016):

$$L_{\rm X} = 4\pi F_{\rm S} D_{\rm L}^2(z)\,(1+z)^{\Gamma-2}\,, \tag{4.4.16}$$

where we have used the soft flux $F_{\rm S}$, the redshift z of each source and we adopted the mean photon index that best represents the bulk of the sources $\Gamma_0 = 1.7$ (see Sect. 4.2). Then we averaged $L_{\rm X}$ for each source. We used a fixed $\Gamma_0 = 1.7$ in Eq. 4.4.16 because the photon indices computed in Sect. 4.2 are affected by relatively large errors. While these errors are less important when considering the variations from the mean value of the source $\Delta\Gamma$, they could be predominant in the absolute Γ, and therefore the use of a mean value is preferred for the computation of $L_{\rm X}$.
Once the X-ray luminosities are computed and averaged for each sources, we group all the observations in X-ray luminosity bins of width $\delta \log L_{\rm X} = 0.1$ and computed β for each bin. As shown in the right panel of Fig. 4.8, there is no dependence on X-ray luminosity either.
This is not surprising, since z and $L_{\rm X}$ are strongly related (see Fig. 4.4). However, the spectral variability parameter does not depend on either the redshift or the X-ray luminosity of the source.
To take into account the dependence between these two parameters we verified that β does not depend on z on a narrower range of $L_{\rm X}$, i.e. $43.5 \lesssim \log L_{\rm X} \lesssim 44.5$ erg s^{-1}.

4.4.2 Black hole mass and Eddington ratio

Neither SDSS catalogues nor the 3XMM-DR5 catalogue include typical parameters of the source, other than the spectroscopically measured redshift.
In order to study the relation between the spectral variability parameter with more of these

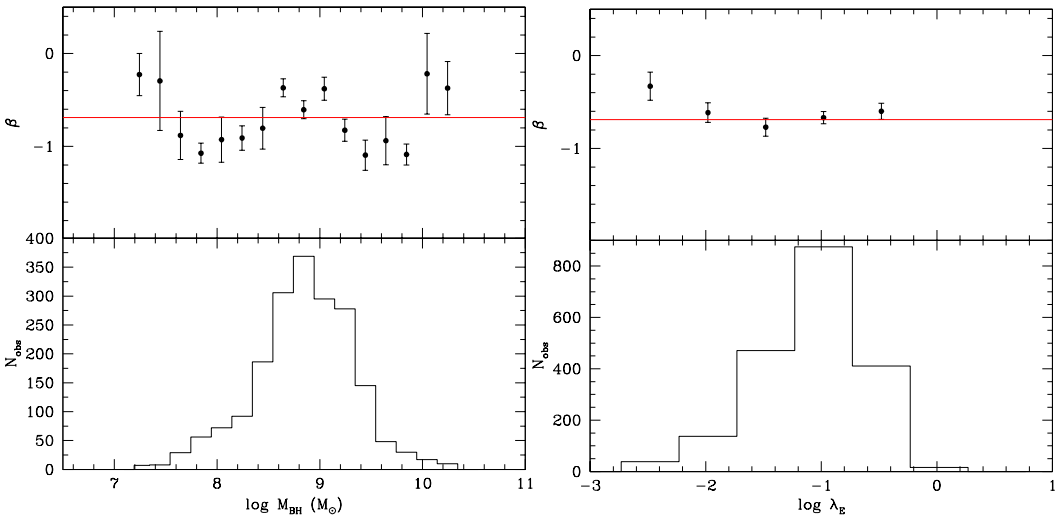

Figure 4.9: *Top.* Dependence of β on black hole mass (left) and Eddington ratio (right). The red line represents the ensemble value $\beta = -0.69$. No clear trend on either $M_{\rm BH}$ or $\lambda_{\rm E} = L/L_{\rm Edd}$ is found. Even though the number of points in the $\log \lambda_{\rm E} \lesssim -2$ bin is scarce and not statistically significant, there appears to be a small rise in the ensemble β, that might be due to the presence in the bin of sources with advection-dominated accretion disks, which are believed to follow a harder when brighter trend (see e.g., Emmanoulopoulos et al., 2012; Connolly et al., 2016). *Bottom.* Histograms of the black hole mass (left) and Eddington ratio (right) bins. The errors on the top figure are related to the number of points included in the bin.

parameters, namely the black hole mass $M_{\rm BH}$ and the Eddington ratio $\lambda_{\rm E} = L/L_{\rm Edd}$, we matched the MEXSAS sample with one that contains such parameters for 105 783 quasars (Shen et al., 2011)[3]. This catalogue only includes sources within the SDSS-DR7Q, which means that we can only analyze a subsample of the MEXSAS, excluding every source that is present in DR12Q, but not in DR7Q. This subsample is made up of 565 unique sources and 1 953 observations.
We divided the sample into bins of black hole mass, with width $\delta \log M_{\rm BH} = 0.2$, and we computed the ensemble β of each bin. As shown in the left panel of Fig. 4.9, also for the black hole mass no clear trend with the spectral variability parameter is found, aside from fluctuations from the ensemble value $\beta = -0.69$. This means that the black hole mass is not a driver for the spectral variability either.
We stress that the black hole masses reported in Shen et al. (2011) are single-epoch virial estimates, which are computed from the Hβ, Mg II and C IV lines, depending on the

[3] http://quasar.astro.illinois.edu/BH_mass/dr7.htm

redshift of the source. These estimates, especially the masses obtained with the C IV, since this line might be affected by winds (e.g., Filiz Ak et al., 2012), are highly uncertain and must be taken with care.

We also divided our sample in bins of Eddington ratio $\lambda_E = L_{bol}/L_{Edd}$ of width $\delta \log \lambda_E = 0.5$. As shown in the right panel of Fig. 4.9, there is no clear trend either on the $\beta - \log \lambda_E$ relation for $-2 \lesssim \log \lambda_E \lesssim 0$, while the bin at $\log \lambda_E \lesssim -2$ shows a small rise towards less negative values. While this point might just be a fluctuation, it might also be due to the presence of Low-Luminosity AGNs (LLAGN), that usually present very small Eddington ratios ($L/L_{Edd} \lesssim 0.01$), possibly due to advection-dominated accretion disks, for which the opposite, harder when brighter, trend is expected (Emmanoulopoulos et al., 2012; Connolly et al., 2016). However, this trend is not strong enough to be conclusive and this hypothesis remains a suggestion.

4.4.3 BALQSOs and radio-loud sources

As mentioned in Chapter 3, the MEXSAS sample also includes some Broad Absorption Line quasars (BALQSO) and radio-loud sources. Both classes might differ in their spectral variability properties from the overall ensemble value. For instance, BALQSOs usually show X-ray absorption associated with wind outflows (e.g., Brandt et al., 2000), and radio-loud sources show enhanced X-ray emission associated with their jets (e.g., Worrall et al., 1987). Moreover some theoretical models have recently suggested that the presence of jets might influence the accretion rate of the disk (Nemmen & Tchekhovskoy, 2015), and this might affect the spectral variability properties of the source.

The cross-matched sample between MEXSAS and DR7Q contains 14 BALQSOs, flagged by Shen et al. (2011) following both C IV and Mg II BAL flags by Gibson et al. (2009) for SDSS-DR5Q sources, and by visual inspection for sources not included in such data release, for 31 observations. SDSS-DR12Q directly flags BALQSOs (Pâris et al., 2017) by visual inspection of the spectra, and we find 171 observations of 63 sources. We merge these two lists, taking into account that 13 observations of 6 sources are repeated in both lists, we remove them from DR7Q, and we end up with 189 observations of 71 unique sources.

We compute the spectral variability parameter of this subsample, finding $\beta = -0.64 \pm 0.16$, with correlation coefficient $r_0 = 0.285$ and probability of finding such correlation by chance given by $p(r > r_0) \simeq 5 \cdot 10^{-5}$. This value of β is very close to the total ensemble value, therefore we conclude that the spectral behaviour of BALQSOs is the same as the average global ensemble one.

We then looked again at the coincident data between MEXSAS and the Shen et al. (2011) catalogue of source parameters. Among the many properties listed, this list displays the

radio loudness parameter, according to the definition of Jiang et al. (2007) (see Sect. 1.2), given by:

$$R = \frac{F_\nu(6\text{ cm})}{F_\nu(2500\text{ Å})}, \tag{4.4.17}$$

computed at rest-frame, for 159 observations of 56 unique sources.
As for the DR12Q sources, not listed in the Shen et al. (2011) sample, we identified in the SDSS catalogue the FIRST flux density (Becker et al., 1995) at wavelength $\lambda = 20$ cm. In order to have results that are comparable with Shen et al. (2011), we computed the radio flux at rest-frame $\lambda = 6$ cm using $F_\nu \propto \nu^\alpha$, after finding the rest-frame frequency corresponding to the observer-frame wavelength $\lambda = 20$ cm, while rest-frame $\lambda = 6$ cm corresponds to $\nu \simeq 5$ GHz. Following Gibson et al. (2008) and Vagnetti et al. (2010) we adopt a typical $\alpha_{\rm radio} = -0.8$ value for all sources.
We also identify the five *ugriz* fluxes in the SDSS (Fukugita et al., 1996) and computed the flux by interpolating between the nearest SDSS rest-frame filters. In case all the filters lie in the same side with respect to rest-frame 2500 Å, we extrapolate the spectrum by using in such case $\alpha_{\rm UV} = -0.46$, following Vanden Berk et al. (2001).
We are now able to compute Eq. 4.4.17, for 244 observations of 80 sources for which the FIRST flux is available. If we merge with the Shen et al. (2011) sources with radio data and exclude nine sources from SDSS-DR7Q that are also present in DR12Q, we remain with a sample of 384 observations of 126 sources. The radio loudness parameter R ranges from $R = 0.3$ to $R = 5 \cdot 10^4$. Most of these sources (114) are radio-loud ($R > 10$) because the radio emission of many radio-quiet sources is undetectable at FIRST flux density limit. For these radio-loud sources we find a spectral variability parameter $\beta = -0.38 \pm 0.10$. This value is less negative than the overall ensemble β of the whole sample. This means that, on average, the spectrum of radio-loud sources is less variable than the rest of the sources. A similar result is found in the optical/UV spectra of another class of jetted AGNs, blazars (Vagnetti et al., 2003).

4.5 Individual sources from the MEXSAS sample

As shown in Sect. 4.4, there is no evidence of clear trends of the spectral variability parameter β with any quasar parameter such as redshift z, X-ray luminosity $L_{\rm X}$, black hole mass $M_{\rm BH}$, and Eddington ratio $L/L_{\rm Edd}$. However, it is clear that fluctuations, even significant ones, from the ensemble values are present in many bins; some bins of X-ray luminosity even show $\beta > 0$, see Fig. 4.8 and 4.9.

Source	$\beta \pm \sigma(\beta)$	$\langle F_{\rm S} \rangle$	$N_{\rm obs}$	r_0	$p\,(r > r_0)$	z	$\log L_{\rm X}$
97	-1.57 ± 0.28	$7.32 \cdot 10^{-14}$	13	0.861	$7.9 \cdot 10^{-5}$	1.288	45.02
117	-1.17 ± 0.15	$3.80 \cdot 10^{-14}$	11	0.932	$1.5 \cdot 10^{-5}$	0.360	43.46
228	-3.54 ± 0.54	$3.34 \cdot 10^{-14}$	8	0.938	$2.9 \cdot 10^{-4}$	1.647	44.88
256	-1.43 ± 0.39	$1.70 \cdot 10^{-14}$	24	0.613	$7.1 \cdot 10^{-4}$	0.770	43.87
269	-0.81 ± 0.10	$5.63 \cdot 10^{-14}$	7	0.964	$2.4 \cdot 10^{-4}$	0.910	44.57
532	-0.80 ± 0.06	$5.82 \cdot 10^{-14}$	5	0.992	$3.9 \cdot 10^{-4}$	0.678	44.33
2066	-0.80 ± 0.06	$9.24 \cdot 10^{-14}$	5	0.991	$4.6 \cdot 10^{-4}$	0.136	42.95
2125	-1.38 ± 0.11	$1.92 \cdot 10^{-14}$	8	0.980	$9.3 \cdot 10^{-6}$	1.843	44.81

Table 4.3: Single-source spectral variability parameter and correlation coefficients are shown in this table. To identify each source, we have reported the serial number in the MEXSAS catalogue that labels each source, which is shown in the first column. For each source, the spectral variability parameter β and its error $\sigma\,(\beta)$, the number of epochs $N_{\rm obs}$, the correlation coefficient r_0, the probability of finding such correlation by chance $p\,(r > r_0)$, the redshift z and the X-ray luminosity $\log L_{\rm X}$ are shown. Also shown is the average value of the soft flux $\langle F_{\rm S} \rangle$ in units of erg s^{-1} cm^{-2}, from which we see that all of the most correlated sources are present in the two brightest flux bins (see Tab. 4.2).

This means that the spectral variability parameter of each source in the bin might be different from each other and deviate significantly from the average ensemble trend. To investigate this, we computed β for every source with a number of observations $N_{\rm obs} > 3$. Even though for a single source calculating β from the $\Gamma - \log F_{\rm S}$ or the $\Delta\Gamma - \Delta \log F_{\rm S}$ correlation is in principle equivalent, we prefer the latter to avoid the possible presence of uncertainties in the calculation of the photon indices. Most of these β values are not significant, though, since either $\Delta\Gamma$ and $\Delta \log F_{\rm S}$ are not actually correlated, suggesting that their spectrum might be mildly variable, or the number of observations is too scarce to obtain a significant linear fit.

For a low number of points N the probability of finding a correlation r_0 by chance is given by (Bevington, 1969):

$$p\,(r > r_0, N) = 2 \int_{|r_0|}^{1} p_x\,(x; \nu_0)\, dx, \tag{4.5.18}$$

where $\nu_0 = N - 2$ is the number of degrees of freedom of the set, and

$$p_x\,(x; \nu_0) = \frac{1}{\sqrt{\pi}} \frac{\Gamma\left[\frac{\nu_0+1}{2}\right]}{\Gamma\left[\frac{\nu_0}{2}\right]} \left(1 - x^2\right)^{\frac{\nu_0-2}{2}}, \tag{4.5.19}$$

where $\Gamma\,[n]$ is the so-called *gamma function*, equivalent to the factorial $n!$, extended to non-integer numbers. We tested Eq. 4.5.18 against Eq. 4.3.11 for various values of the number of dataset points N, and we found that the two expressions basically give the same results for $N \gtrsim 50$, while they differ for a lower number of points. Given that all

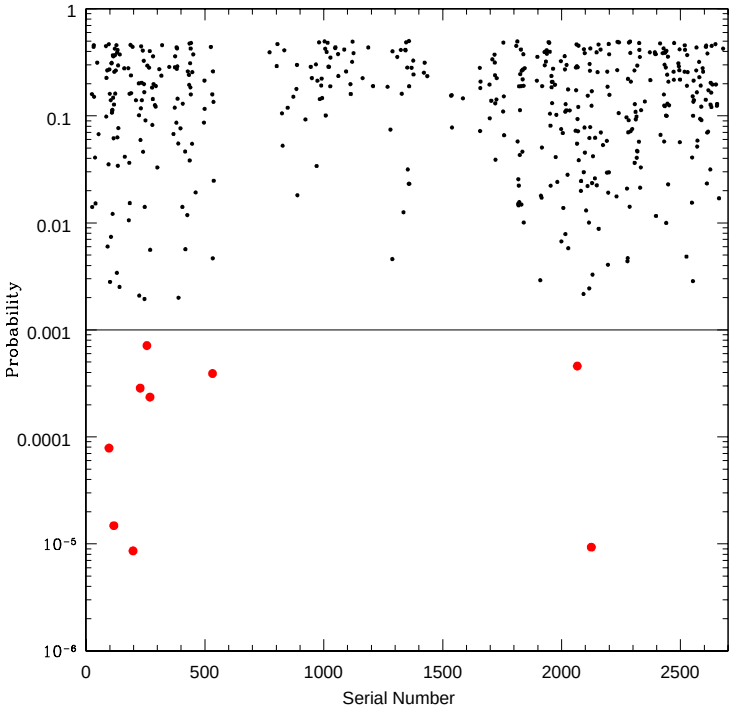

Figure 4.10: Probability $p\,(r > r_0)$ that the correlation between $\Delta\Gamma$ and $\Delta \log F_S$ is obtained by chance. The horizontal line represent the threshold for source selection $p = 10^{-3}$. The red dots represents the selected nine sources that satisfy the requirement $p \leq 10^{-3}$. Out of these nine sources, source 198, also known as PG 1114+445, was discarded due to the presence of a warm absorber (see Chapter 6).

XMM sources have $N_{\rm obs} < 50$, we must compute $p\,(r > r_0, N_{\rm obs})$ using Eq. 4.5.18.
We only selected those quasars for which $p\,(r > r_0) \leq 10^{-3}$, because we only want to select those sources with the most significant probability. Nine sources satisfy this requirement (see Fig. 4.10), although only eight of which are listed in Table 4.3. Source 198 is missing from that list because, after visual inspection of the X-ray spectra plots made available by the XMM-Newton Science Archive[4], we identified source 198 with PG 1114+445, a source that is already known in the literature for having a significant warm absorber (Ashton et al., 2004; Piconcelli et al., 2005, XMM-Newton observation), and the possible presence of a highly ionized gas outflow with velocity $v \sim 0.1c$ (George et al., 1997, ASCA observation). We stated that the presence of such spectral features, along with others, affects approximately 10% of the MEXSAS catalogue. Although these cases are statistically negligible in an ensemble study, they are crucial in the calculation of Γ and β for single sources, therefore a more exhaustive analysis is needed. A detailed study of the 12 XMM-Newton X-ray spectra of PG 1114+445, along with a new spectral analysis of the ASCA spectrum, already studied by George et al. (1997), will be presented in Chapter 6. For the moment, we just exclude the source from the list and analyze the remaining eight

[4] http://nxsa.esac.esa.int/nxsa-web

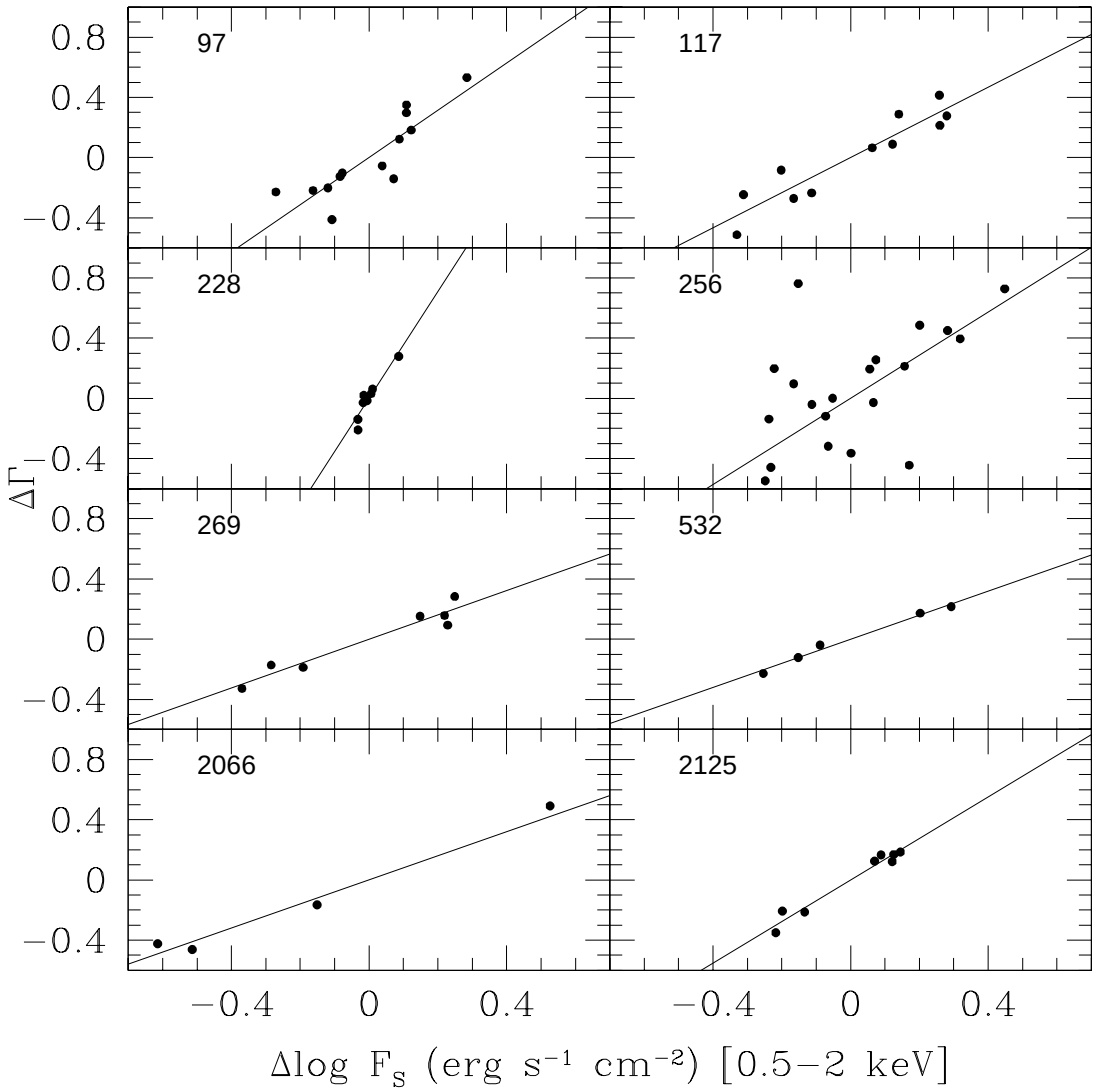

Figure 4.11: $\Delta\Gamma - \Delta \log F_S$ plots for the eight individual sources, listed in Table 4.3, with low probability of spurious correlation ($p \leq 10^{-3}$). We plotted the eight sources with the same scale, in order to compare them. The slopes of those linear fits are quite different from source to source, and they range from $\beta = -3.54$ to $\beta = -0.80$, suggesting that even though the spectral variability driver is likely the same, it acts with different extent from source to source. The errors are not shown, because we computed β without taking such errors into account.

sources with photon indices computed as shown in Sect. 4.2.

As it can be seen in Table 4.3, these eight single sources are distributed in a wide range of X-ray luminosity and redshift. All these sources show a softer when brighter trend, with high correlation coefficients, although with different extents. Indeed, β ranges from $\beta = -0.80 \pm 0.06$ for sources 532 and 2066 to an extreme value of $\beta = -3.54 \pm 0.54$ for source 228. All the sources belong to the highest flux bin of Table 4.2, confirming that the brightest sources are also the most correlated ones.

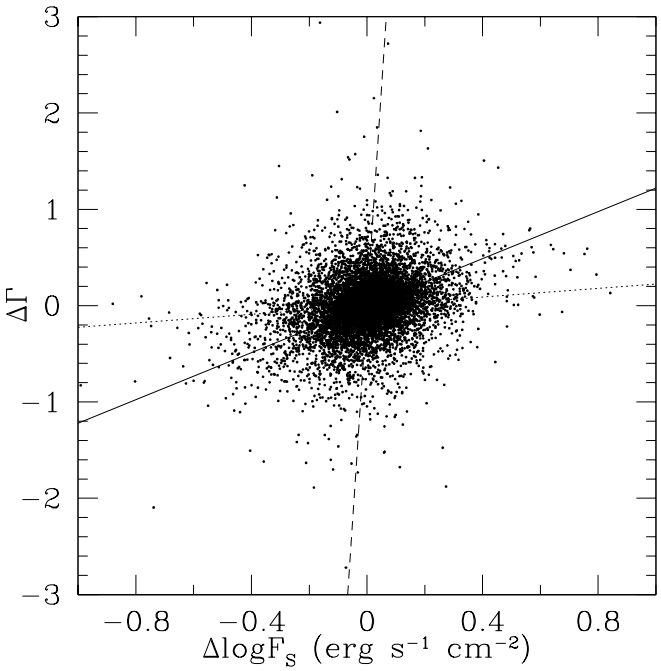

Figure 4.12: $\Delta\Gamma - \Delta \log F$ correlation. The dotted line represents the OLS($Y|X$) linear regression, and the dashed line instead represents the OLS($X|Y$). The bisector is represented by a continuous line.

4.6 Bisector method and the MEXSAS2 sample results

We updated the ensemble analysis using MEXSAS2 (see Sect. 3.3; Serafinelli et al., 2017a; Vagnetti et al., 2018).

The ensemble correlation between $\Delta\Gamma$ and $\Delta \log F$ is affected by large scatters, mostly due to measurement errors for the faintest sources. We fitted the $\Delta\Gamma - \Delta \log F$ relation taking these uncertainties into account. We performed several linear fits, by replacing the original data with 10^4 simulated points within the error bar of each catalogue entry, and then we averaged the arctan of the angular coefficient, so that the desired β is the tangent of this quantity.

Moreover, following Isobe et al. (1990), we computed both the least squares regression OLS($Y|X$) of the dependent variable Y on the independent variable X, which we call β_{xy} and is equal to the usual β from Eq. 4.0.1, and the inverse regression OLS($X|Y$), which we call β_{yx}, and then we compute the bisector, as follows:

$$\beta_{bis} = \frac{\beta_{xy}\beta_{yx} - 1 + \sqrt{\left(1+\beta_{xy}^2\right)\left(1+\beta_{yx}^2\right)}}{\beta_{xy} + \beta_{yx}}. \tag{4.6.20}$$

For the ensemble set we find that these two estimators give $\beta_{xy} = -0.22 \pm 0.04$ and

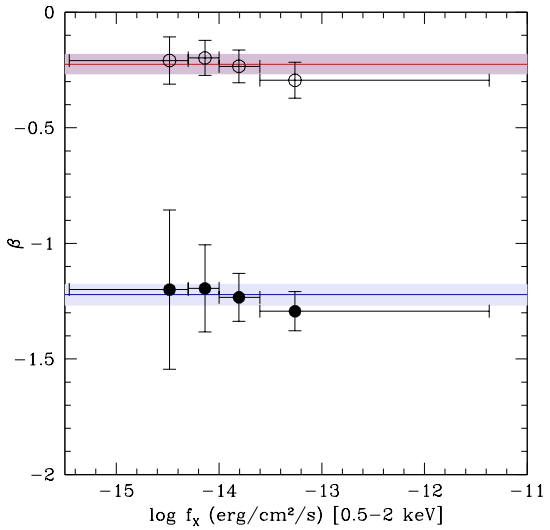

Figure 4.13: β vs flux. The upper red line is the ensemble β_{xy} with its error, shown as a grey band. The blue line instead is the ensemble β_{bis} with its error, represented by the blue band. The dependence seen in Fig. 4.5 is greatly reduced.

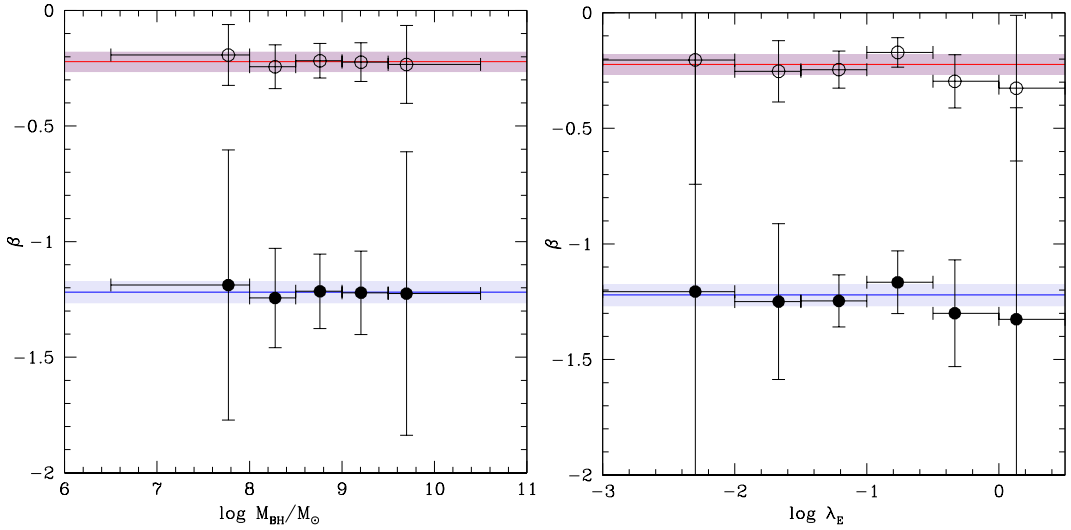

Figure 4.14: *Left.* β vs $M_{\rm BH}$. As in Fig. 4.13, the red line is the ensemble β_{xy} and the grey band is its error, with analogous meaning for the blue line and band for β_{bis}. The values of both estimators are compatible with the ensemble value. *Right.* β vs $\lambda_{\rm E} = L/L_{\rm Edd}$. Same color legend. MEXSAS2 confirms no dependence also on the Eddington ratio, for both the estimators. This result is statistically more significant than the one in Sect. 4.4.2, since it involves a much larger number of sources.

$\beta_{bis} = -1.22 \pm 0.05$ (see Fig. 4.12), confirming the softer when brighter trend, already found for MEXSAS.
Moreover, we also tested both spectral variability estimators β_{xy} and β_{bis} versus the flux, and we found that in every bin, the value is close to the ensemble one, for both estimators (Fig. 4.13). This result shows that the dependence on the flux bins that we found in Fig. 4.5 was due to the large measurement errors, and it disappears when such large errors are taken into account.
Thanks to the addition of masses and luminosities for nearly all sources in the MEXSAS2 catalogue (see Sect. 3.3 for details), we were able to confirm no trend with either the black hole mass or Eddington ratio (see Fig. 4.14), for both spectral variability estimators, confirming the result of Sect. 4.4.2 for a much larger statistical sample.

4.7 Summary and discussion

A negative spectral variability parameter β, as well as the bisector estimator β_{bis}, means that the spectrum of the AGN becomes steeper when the source is in a high flux state. This means that the bulk of the SDSS-selected sources follow this trend.
Our approximate calculation of Γ is very similar with the accurate one performed by Corral et al. (2015) on a small subset of our sample, and this means that the method - although unable to account for spectral features such as absorption, iron lines or soft excess - is able to give a reliable estimate of the photon index. Moreover, the calculation of β gives the same result for both Γ computed by Corral et al. (2015) and by us.
The errors in both $\Delta\Gamma$ and $\Delta \log F$ are higher for fainter sources, and this produces an apparent dependence of β on the flux, since brighter sources appear to be more correlated than fainter ones. This bias can be removed by taking errors into account, as shown in Fig. 4.13.
As discussed in Chapter 2, the observed variations of Γ can be either intrinsic or apparent, due to the superposition of a continuum that is variable in flux, but not in photon index, and a reflection component that is constant.
No significant trend with either redshift z, X-ray luminosity $L_{\rm X}$, black hole mass $M_{\rm BH}$ or Eddington ratio $\lambda_{\rm E} = L_{\rm bol}/L_{\rm Edd}$ is found. This means that the mechanism that generates the spectral variability is likely the same for the majority of the sources. It is expected, though, that low-accreting sources ($L/L_{\rm Edd} \leq 0.01$) follow the opposite, harder when brighter, trend, due to the low UV emission of these sources, that makes UV radiation not the dominant seed photon source anymore. Quasars with these low accretion rates are very rare though, and even though we have a hint that low-Eddington ratio sources tend to have positive βs (see Fig. 4.9, right panel), we have very few points to confirm it.

We computed β for a subsample of 114 radio-loud sources, finding slightly smaller absolute values of β, which could be due to additional X-ray emission from the jet (e.g., Worrall et al., 1987). On the contrary, BALQSOs have β values that are comparable to the one of the ensemble, suggesting that warm absorbers, to which BALs seem to be connected (e.g., Brandt et al., 2000), should play a marginal role in spectral variability.

We also computed individual values of β for a restricted set of eight sources (see Table 4.3) with significant $\Gamma - \log F$ correlations. We find a great range of β, from -3.54 ± 0.54 to -0.80 ± 0.06. The origin of such spread is not clear, we speculate that it might depend on the inclination of the AGN with respect to the line of sight, in the scenario that spectral variability is mainly driven from the superposition of a constant reflection component, that clearly depends on the angle of view ι. Another possibility, though hardly verifiable, is that the black hole spin plays some role, by means of the additional X-ray emission from the jet, partially suggested from the different value we find for the radio-loud subset and from the fact that red wings in the Fe Kα line, associated with fast-spinning black holes, do not appear to show variability (Brenneman & Reynolds, 2006). Prominent soft excesses or ionized absorbers may also have some effect on the variations of the spectra of AGNs.

Next-generation X-ray telescopes, such as the NASA/JAXA *X-ray Astronomy Recovery Mission* (XARM[5]), an identical copy of the defunct JAXA X-ray telescope Hitomi/ASTRO-H (Takahashi et al., 2014), scheduled for launch in 2021, or eROSITA (Merloni et al., 2012), scheduled for 2019, that is estimated to be able to detect $\sim 10^6 - 10^7$ AGN at redshifts up to $z \sim 7 - 8$ (Predehl et al., 2010), would certainly improve this kind of ensemble variability studies with vast catalogues and high-resolution spectroscopy. Moreover, in the farther future, Athena (Nandra et al., 2013), scheduled for launch in 2030, and possibly *Lynx X-ray Surveyor*, with its larger collecting area and Chandra-like spatial resolution, whose fate will be decided by NASA in 2020[6], will certainly shed more light on the topic.

[5] https://heasarc.gsfc.nasa.gov/docs/xarm/
[6] https://wwwastro.msfc.nasa.gov/lynx/

Chapter 5

SPECTRAL VARIABILITY OF NEARBY SEYFERT GALAXIES

5.1 Methodology

We studied the X-ray spectral variability of a sample of 9 nearby type-1 AGN, using XMM-Newton EPIC-pn spectra (Serafinelli et al., 2018a). The sample was already described in Sect. 3.4 and summarized in Table 3.1, including PG 1114+445, that will be analyzed in the next chapter. All these sources have redshifts $z \lesssim 0.05$, with a great variety of masses, that range from $\log M_{\rm BH}/M_{\odot} \simeq 6$ up to $\log M_{\rm BH}/M_{\odot} \simeq 8.5$, obtained with both reverberation mapping and single-epoch virial techniques (see Table 3.1 for details and references), and bolometric luminosities, that range from $\log L_{\rm bol} \simeq 41.5$ to $\log L_{\rm bol} \simeq 45.5$.
As it was done for the first ensemble study on data from the XMMSSC, we quantify the spectral variability with the simple parameter β:

$$\beta = -\frac{\Delta\Gamma}{\Delta \log F}. \tag{5.1.1}$$

Again, $\beta < 0$ suggests a softer when brighter trend for the spectrum, while $\beta > 0$ suggests the opposite, harder when brighter, behaviour.
Given that we are dealing with nearby, very bright, sources, there is no need to take measurement errors into account and therefore we carried a traditional linear fit study of the $\Delta\Gamma - \Delta \log F$ correlation. In ensemble studies it is necessary to fit deviations from mean values of both photon index and flux logarithms, to take the heterogeneity of the sample into account, while in single-source studies such as this one this is not necessary.
In Chapter 4 (Serafinelli et al., 2017b) we computed approximate Γs, assuming that the

spectrum is a pure power law.

We use a different approach here. These sources are very bright and it is possible to study their spectral features, therefore we retrieved all the data products of each source from the XMM Archive (XSA[1]), reduced their data with the standard procedure (see Appendix A for details), and computed the photon index by performing spectral fits with model as accurate as possible. For each source we used previously developed spectral models from the literature. Since we are mainly interested in the spectral variability of the continuum, we only modelled the $3-10$ keV band of the spectrum, to avoid complications from the soft excess, that does not have significant effects on the $3-10$ keV band. With the exception of NGC 5548 (see Sect. 5.2 for details), we always used the same model for each observation of the same source.

All spectra were produced using the software SAS 16.0.0, removing proton flaring and correcting for pile-up when appropriate, as described in Appendix A. They were binned at 60 counts per bin, forcing an energy bin of 1/5 of the full width half maximum (FWHM) resolution.

Concerning the fluxes, we want to analyze how the photon index responds to variations of the continuum, therefore we only extrapolated the $2-10$ keV flux of the continuum, excluding absorbing components or the Fe Kα line. To do this, we used the `XSPEC` (Arnaud, 1996) command `flux`. Once the model is fitted to the spectrum, we retrieve the output values of the photon index Γ_0 and the normalization n_0. Using the command `error`, it is possible to compute the asymmetric 1σ errors of both variables. Let us call $\sigma_1(\Gamma)$ and $\sigma_1(n)$ the "left" errors on Γ and n, and $\sigma_2(\Gamma)$ and $\sigma_2(n)$ the "right" errors on Γ and n, in this way we will have

$$\Gamma = \Gamma_0 \, {}^{+\sigma_2(\Gamma)}_{-\sigma_1(\Gamma)}$$

and

$$n = n_0 \, {}^{+\sigma_2(n)}_{-\sigma_1(n)}.$$

We simulate then a pure power law model, with Γ_0 and n_0, and by means of the command `flux` we obtain the $2-10$ keV flux F_0. The lowest possible state is obtained by setting instead the minimum normalization, $n-\sigma_1(n)$, and the softest continuum, represented by $\Gamma_0+\sigma_2(\Gamma)$. The `flux` command will return $F_0-\sigma_1(F_0)$. In the same way, we can obtain $F_0+\sigma_2(F_0)$ by setting $n+\sigma_2(n)$ and $\Gamma_0-\sigma_1(\Gamma)$.

Once the photon indices and the fluxes are rightfully computed for every observation, it is possible to apply Eq. 5.1.1 and compute the spectral variability parameter of a given source.

Power law continua were modelled with `XSPEC` model `powerlaw`. Fe Kα lines were usually modelled with Gaussian lines, with fixed centroid energy at 6.4 keV and variable width,

[1] http://nxsa.esac.esa.int/nxsa-web/

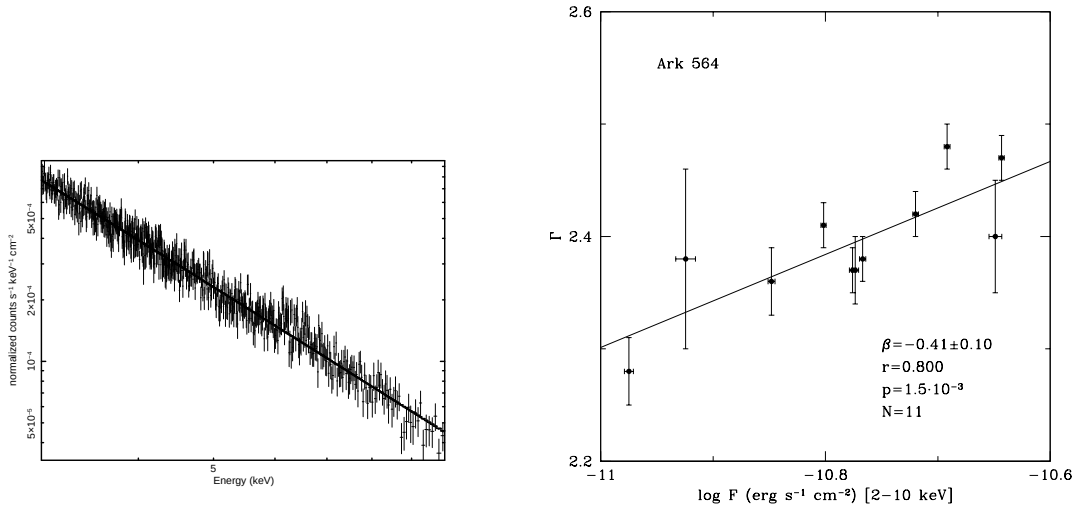

Figure 5.1: *Left.* Ark 564 hard energy ($3-10$ keV) spectrum. The spectrum is well fitted by a simple power law. *Right.* $\Gamma - \log F$ correlation, showing softer when brighter behaviour with high correlation coefficient and low probability of random correlation.

that take the redshift, however small, into account (`zgauss`), with the exception of NGC 5506, in which we modelled the full reflection spectrum using `xillver`, to take into account the ionization state of the disk. As for ionized absorbers, for this work we used `zxipcf`, that assumes a standard value of the turbulence (200 km s^{-1}). The Galactic absorption was taken into account by using the model `phabs`, fixing the value of $N_{\rm H}$ to the appropriate value for the source coordinates, taken from Kalberla et al. (2005).

5.2 Sources and spectral fits

We report in the following the spectral analysis and the results of the sources of Table 3.1, with the exception of PG 1114+445, that will be analyzed in Chapter 6. All the computed values of the spectral variability parameter, with its correlation coefficient and probability of spurious correlation, are reported in Table 5.1.

5.2.1 Ark 564

Ark 564 is the brightest ($F_{2-10} \sim 1.5 \cdot 10^{-11}$ erg cm^{-2} s^{-1}) Narrow-Line Seyfert 1 galaxy (NLS1) in the sky. It was observed 11 times by XMM-Newton during different campaigns. To avoid complications due to the soft excess of this source (Kara et al., 2017), and since we do not find any evidence of the presence of a Fe Kα line nor absorption, following Papadakis et al. (2007), we fit all the $3-10$ keV spectra with a simple power law model, with moderate Galactic absorption $N_{\rm H}^{\rm gal} = 5.34 \cdot 10^{20}$ cm^{-2} (Kalberla et al., 2005) taken

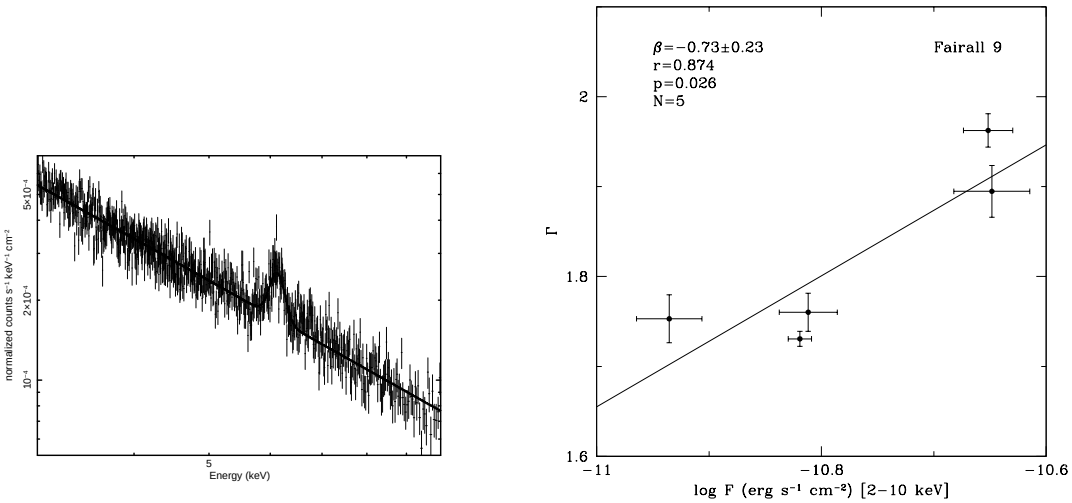

Figure 5.2: *Left.* Fairall 9 hard energy ($3-10$ keV) spectrum. The spectrum is well fitted by a simple power law plus iron Kα line. *Right.* $\Gamma - \log F$ correlation, showing softer when brighter behaviour with high correlation coefficient and low probability of random correlation.

into account by using the `phabs` model.
We find $\beta = -0.41 \pm 0.10$, which means that the spectrum is softer when the source is brighter, with high correlation coefficient ($r = 0.800$) and spurious correlation probability (see Eq. 4.5.18) given by $p = 1.5 \cdot 10^{-3}$. Both the spectrum (with fitted model) and the $\Gamma - \log F$ correlation are shown in Fig. 5.1.

5.2.2 Fairall 9

The Seyfert 1 galaxy Fairall 9 was observed by XMM-Newton in five different occasions. A very complex two-component soft excess is present in this source (Lohfink et al., 2016), and therefore only the $3-10$ keV band was considered. The Fe Kα line is clearly visible in the spectrum of this source, and therefore we adopted a model consisting in a power law plus Gaussian iron line, and Galactic absorption fixed at $N_{\rm H}^{\rm gal} = 3.16 \cdot 10^{20}$ cm^{-2}.
As shown in Fig. 5.2, the source shows a softer when brighter trend, with $\beta = -0.73 \pm 0.23$, high correlation coefficient $r = 0.874$ and moderately low probability of finding such correlation by chance ($p = 0.026$).

5.2.3 M81

Nearby low-luminosity active galaxy (LLAGN) M81 (also known as NGC 3031) has been observed 14 times by XMM-Newton. Connolly et al. (2016) studied the spectral variability of this source using Swift data, obtaining a harder when brighter behaviour. They ex-

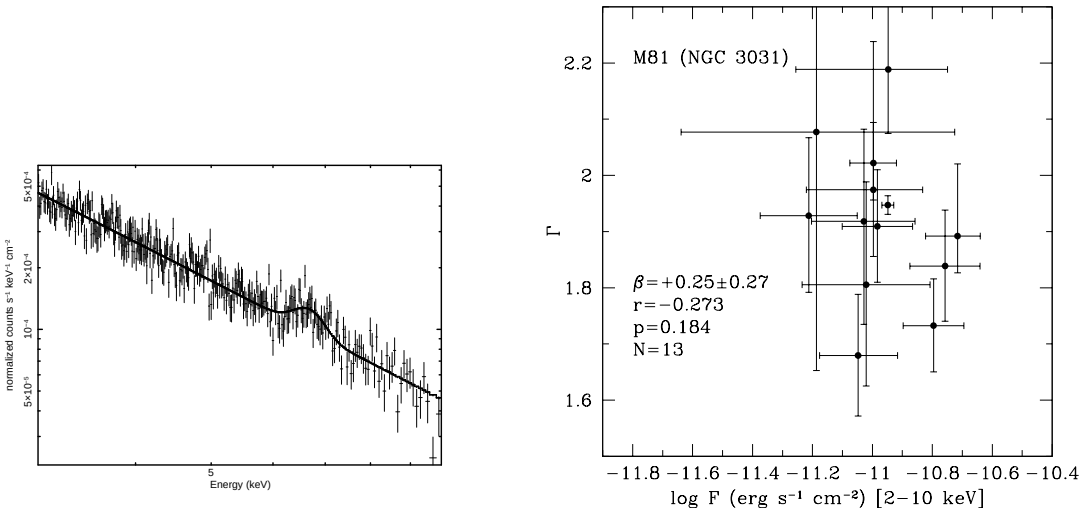

Figure 5.3: *Left.* Best M81 hard energy ($3-10$ keV) spectrum. The spectrum is well fitted by a simple power law plus iron Kα line. *Right.* $\Gamma - \log F$ correlation, showing a positive β, suggesting harder when brighter behaviour, but the correlation is very small with high probability of finding it by chance.

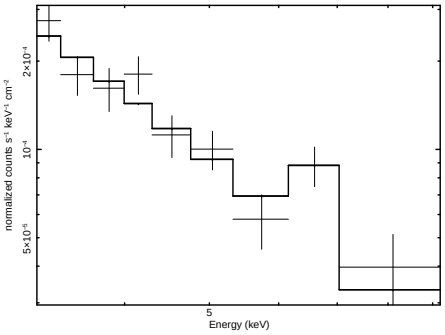

Figure 5.4: Most of the M81 spectra have low signal-to-noise ratio, because the observations were targeted at nearby ULX Holmberg IX X-1. The wide field of XMM-Newton allowed M81 to be observed, but the spectra have low S/N.

plained this behaviour with the extremely low normalized accretion rate ($L/L_{\rm Edd} \lesssim 10^{-4}$). At these low accretion rates it has been proposed (e.g., Reynolds et al., 1996) that the inner accretion disk is dominated by advection onto the black hole rather than by radiative efficiency, therefore the dominant seed photons are expected to be synchrotron X-ray photons from the corona itself, in analogy to what is commonly seen in black hole X-ray binary systems.

Following Dewangan et al. (2004) we model this source using a simple powerlaw with Galactic absorption, fixed at $N_{\rm H}^{\rm gal} = 5.5 \cdot 10^{20}$ cm^{-2}, and a Gaussian iron line at 6.4 keV. One observation (OBSID 0657801801) was severely affected by high background flaring (De Luca & Molendi, 2004), therefore we were not able to retrieve any spectra, reducing

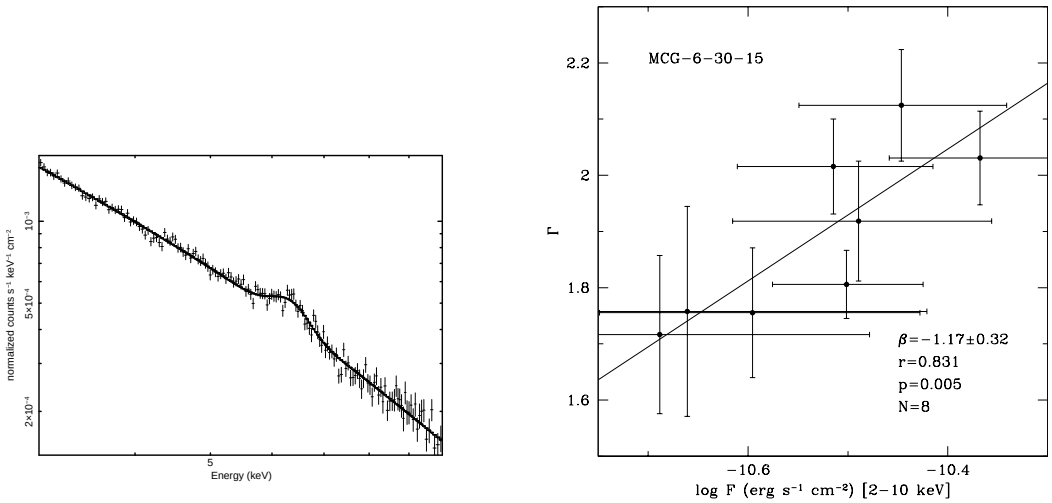

Figure 5.5: *Left.* MCG-6-15-30 hard energy ($3 - 10$ keV) spectrum. The spectrum is well fitted by a power law plus iron Kα line. *Right.* $\Gamma - \log F$ correlation, showing a negative β, with high correlation coefficient and small probability of finding it by chance.

the number of observations to 13.

We find a positive value of the spectral variability parameter ($\beta = 0.25 \pm 0.27$), but a very poor correlation ($r = -0.273$) and a high probability ($p = 0.184$) that this correlation is obtained by chance (see Fig. 5.3).

In all but one epoch (OBSID 0111800101) the source was not the target for the observation, therefore most of the observations have low signal-to-noise ratios, which is higher in the center of the camera (see Fig. 5.4 for an example of low signal-to-noise ratio spectrum of M81). For OBSID 0200980101, the source was out of the sight of the pn camera and therefore we retrieve a spectrum by combining MOS1 and MOS2 cameras. Moreover, it should be stressed that we also neglected the effect of possible X-ray sources close to the galactic center. We extracted the spectra in a region of 40" radius containing the source, according to the resolution of XMM-Newton. Local X-ray sources have been detected in this region with higher spatial resolution instrument Chandra by Swartz et al. (2003), in which the authors estimated a negligible effect on the photon index Γ of the spectrum, but it is not excluded that they might affect variability studies. All these effects are possible explanations for the low $\Gamma - \log F$ correlation in M81.

5.2.4 MCG-6-30-15

The Seyfert 1 galaxy MCG-6-30-15 was observed eight times by XMM-Newton, and to date is still the source with the most accurate calculation of black hole spin ($a \simeq 0.990^{+0.009}_{-0.002}$, Brenneman & Reynolds, 2006).

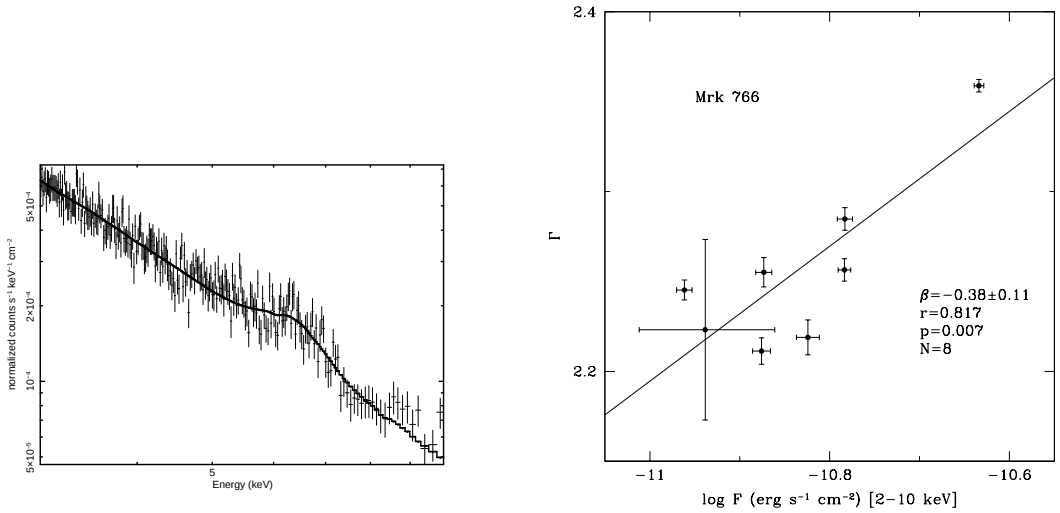

Figure 5.6: *Left.* Mrk766 hard energy ($3-10$ keV) spectrum. The spectrum is well fitted by a two ionized absorbers, power law plus iron Kα line. *Right.* $\Gamma - \log F$ correlation, showing a negative β, with high correlation coefficient and small probability of finding it by chance.

Given the extremely complex nature of the soft spectrum of this source (Miller et al., 2008), we only model this source in the $3-10$ keV band.
We used a simplified model, comprising of a powerlaw and Galactic absorption with fixed column density $N_{\rm H}^{\rm gal} = 3.92 \cdot 10^{20}$ cm^{-2}, and the addition of a fixed iron line at 6.4 keV, as well as the simplified treatment by Marinucci et al. (2014).
The correlation between the unabsorbed fluxes and the photon indices can be found in Fig. 5.5. We find $\beta = -1.17 \pm 0.32$, high correlation $r = 0.831$ and low probability of spurious correlation ($p = 5 \cdot 10^{-3}$).

5.2.5 Mrk 766

We analysed 8 observations from the NLS1 galaxy Markarian 766.
A detailed spectral study of this source was presented in Miller et al. (2007) and Turner et al. (2007). Using the same XMM-Newton data as this work, they found that the source can be modeled either by a scattering component or a warm absorber with partial covering factor. An extra component, which Risaliti et al. (2011) identified with absorption due to broad-line region clouds, is also needed to correctly model the X-ray spectra.
We therefore model this source in the $3-10$ keV band with two ionized absorbers, plus Galactic absorption with fixed column density $N_{\rm H}^{\rm gal} = 1.78 \cdot 10^{20}$ cm^{-2}, powerlaw component and iron line with fixed energy at 6.4 keV.
The correlation between the unabsorbed fluxes and the photon indices Γ, obtained by fitting such spectral model, is shown in Fig. 5.6. We obtain $\beta = -0.38 \pm 0.11$, with a

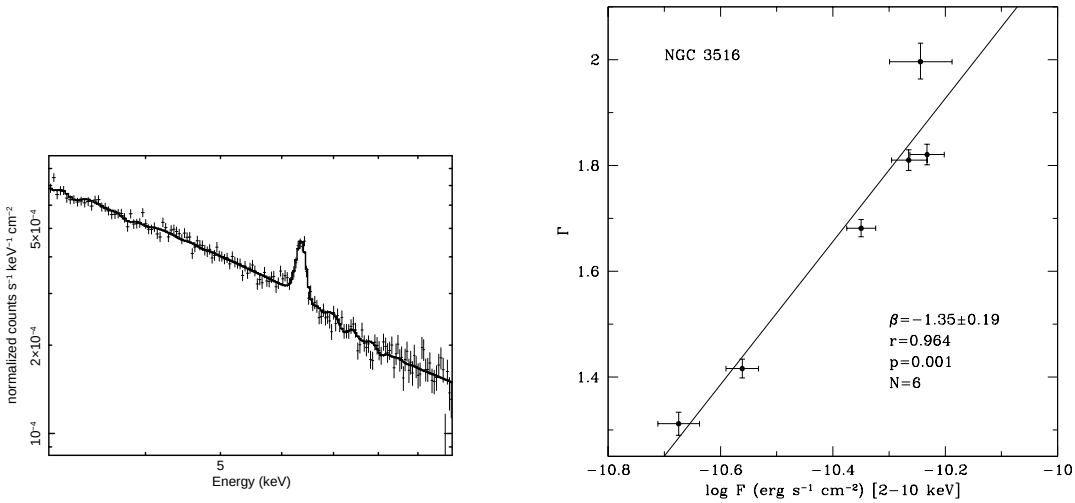

Figure 5.7: *Left.* NGC 3516 hard energy ($3-10$ keV) spectrum. The spectrum is well fitted by a ionized absorber, power law and an iron Kα line. *Right.* $\Gamma - \log F$ correlation, showing a negative β, with high correlation coefficient and small probability of finding it by chance.

high correlation coefficient ($r = 0.817$) and a relatively low probability of finding such correlation by chance ($p = 0.007$). These results are quite similar to those of Ark 564, also a NLS1.

5.2.6 NGC 3516

NGC 3516 is a Seyfert 1 galaxy, observed six times by XMM-Newton.
It was found by Turner et al. (2008) that two layers of ionized absorbers are present in this source, one highly ionized, with Fe XXV (He-like) and Fe XXVI (H-like), and a less ionized one.
In our fit in the $3-10$ keV we model the data by taking into account only the more ionized absorber, a power law and a line at fixed energy 6.4 keV, and fixed galactic column density of $N_{\rm H}^{\rm gal} = 3.45 \cdot 10^{20}$ cm^{-2}.
A very large positive correlation ($r = 0.964$) is found, with probability of spurious correlation equal to $p = 0.001$ (see Fig. 5.7). The spectral variability parameter is given by $\beta = -1.35 \pm 0.19$, which again means that the spectrum follows a softer when brighter trend.

5.2.7 NGC 4051

NLS1 galaxy NGC 4051 has been the subject of many single observations and one campaign in 2009 by XMM-Newton, totalling 17 observations of the source.

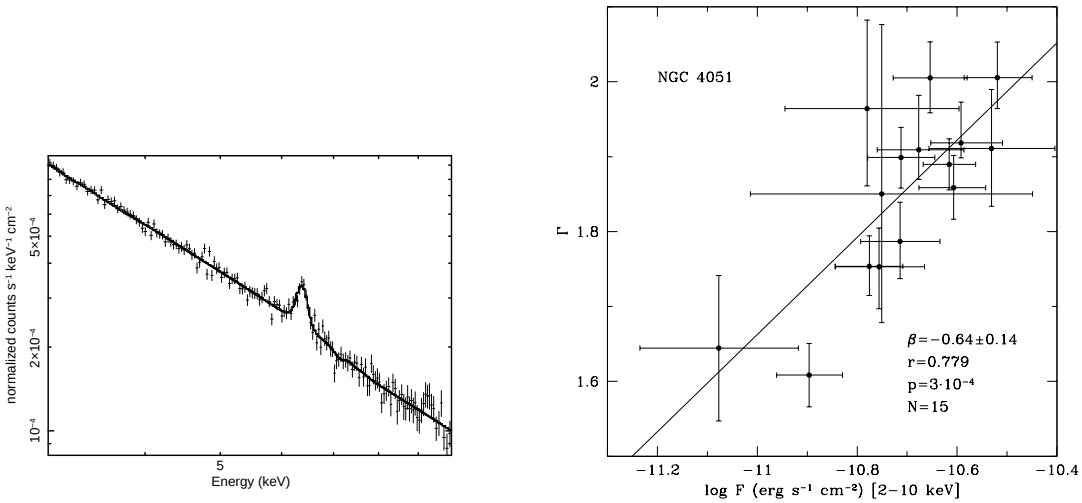

Figure 5.8: *Left.* NGC 4051 hard energy ($3-10$ keV) spectrum. The spectrum is well fitted by a ionized absorber, power law and an iron Kα line. *Right.* $\Gamma - \log F$ correlation, showing a negative β, with high correlation coefficient and small probability of finding it by chance.

The source is notoriously outflowing (Pounds & Vaughan, 2011a,b, 2012), consistently with a scenario of shocked winds by the interstellar medium, inferred from the structure of the absorption lines.

At $3-10$ keV, the source is well modelled by a ionized absorber with variable redshift, to take the velocity of the outflow into account.

The Galactic absorption column density is given by $N_{\rm H}^{\rm gal} = 1.15 \cdot 10^{20}$ cm^{-2}. We also added a power law continuum and a Gaussian iron line with fixed central energy at 6.4 keV.

The spectral variability parameter is $\beta = -0.64 \pm 0.14$, with high positive correlation coefficient ($r = 0.779$) and very low probability of spurious correlation, given by $p = 3 \cdot 10^{-4}$.

5.2.8 NGC 5506

XMM-Newton observed the NLS1 galaxy NGC 5506 in 9 occasions.

This source shows evidence of extreme broadening of the Fe Kα line, due to the superposition of neutral iron line, Fe XXV and Fe XXVI emission lines, which means that the reflection spectrum is highly ionized.

Therefore we did not model this source with the usual Gaussian line, but we added a reflection on a ionized disk component, using the spectral model `xillver` (García et al., 2013) in `XSPEC`. Following Matt et al. (2015), we fixed the cut-off energy to 720 keV and we assumed a typical angle of view of 60°.

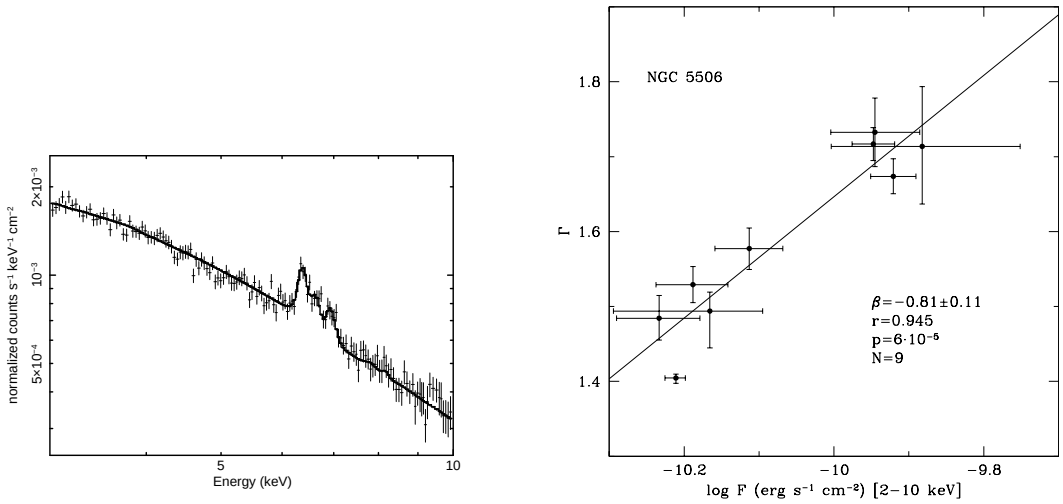

Figure 5.9: *Left.* NGC 5506 hard energy ($3 - 10$ keV) spectrum. The spectrum shows evidence of Fe XXV and Fe XXVI emission lines, emitted by the disk. A reflection on ionized disk model (`xillver`), that also takes the Fe Kα line into account was therefore used. A ionized absorber and power law are also fitted. *Right.* $\Gamma - \log F$ correlation, showing a negative β, with extremely high correlation coefficient and small probability of finding it by chance.

In addition to the power law and to the reflection on ionized disk components, we also found that a ionized absorber is also necessary. The Galactic column density is fixed to $N_{\rm H}^{\rm gal} = 4.08 \cdot 10^{20}$ cm^{-2}

We find a negative spectral variability parameter $\beta = -0.81 \pm 0.11$, with a very high correlation coefficient $r = 0.945$ and an extremely low probability of finding such correlation by chance, given by $p = 6 \cdot 10^{-5}$ (see Fig. 5.9).

5.2.9 NGC 5548

NGC 5548 is one of the most studied Seyfert 1 galaxies in the sky, in all electromagnetic bands. In particular, XMM-Newton observed this source 19 times.

In the X-rays, prior to 2013, the source used to have a simple power law continuum spectrum, plus iron line and black body soft excess. In an observational campaign performed during 2013, Kaastra et al. (2014) found the source in an exceptional low state, which was not due to regular variability of the source, but to the appearance of a large column density ionized absorber (see Fig. 5.11).

We could not use the same model for pre-2013 and post-2013 observations, then. We adopted a very simple power law plus iron line and Galactic absorption ($N_{\rm H}^{\rm gal} = 1.55 \cdot 10^{20}$ cm^{-2}) for the three observations taken prior to 2013. As for the rest of the observations, the addition of a ionized absorber was necessary.

Two observations (OBSIDs 0720110301 and 0720111601) have very low signal-to-noise

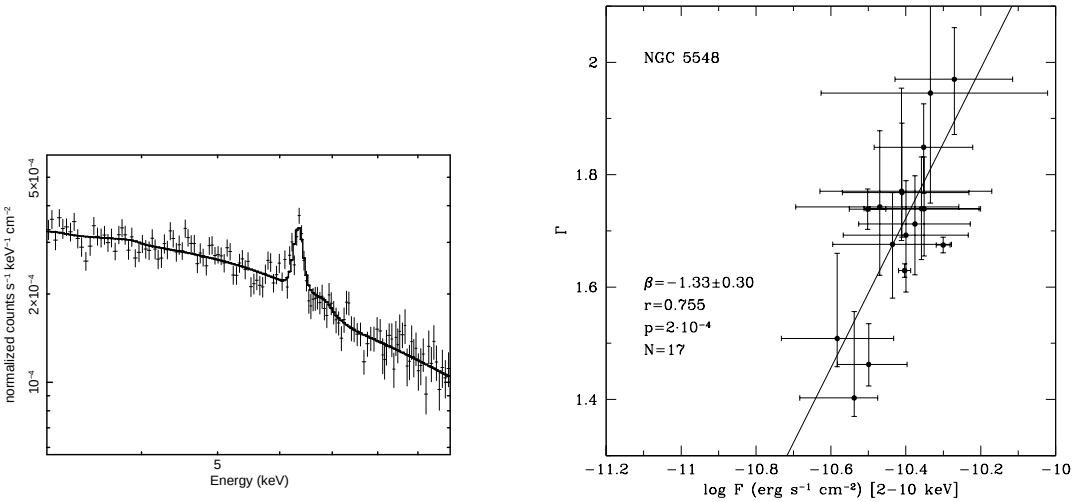

Figure 5.10: *Left.* NGC 5548 post-2013 hard energy ($3-10$ keV) spectrum. In this case, the spectrum is well fitted by a ionized absorber, power law and an iron Kα line. In pre-2013 observations, the ionized absorber is not present (see Fig. 5.11). *Right.* $\Gamma - \log F$ correlation, showing a negative β, with high correlation coefficient and small probability of finding it by chance.

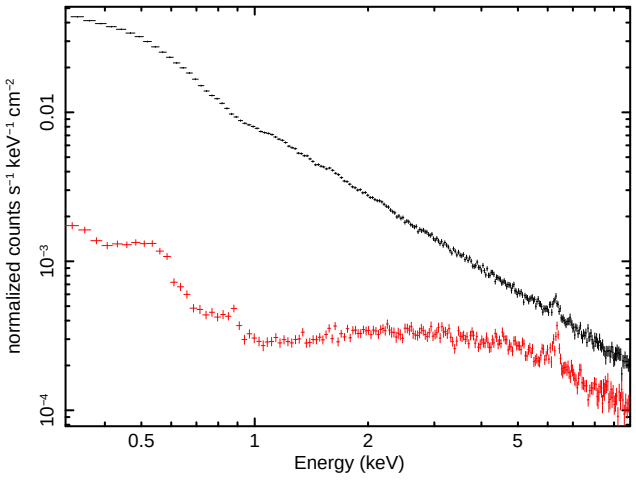

Figure 5.11: The difference between the two spectra from NGC 5548 is evident when showing comparison between full ($0.3-10$ keV) spectra. Prior to 2013 (black) the source was dominated by power law continuum, and a soft excess that is modest, if compared with the continuum. After 2013 (red), a prominent ionized absorber appeared (Kaastra et al., 2014) and therefore it is not possible to fit the same model to both pre- and post-2013 observations.

Source	$\beta_{\rm xs}$	$r_{\rm xs}$	$p_{\rm xs}$	$\beta_{\rm tab}$	$r_{\rm tab}$	$p_{\rm tab}$
Ark 564	-0.41 ± 0.10	$+0.800$	$1.5 \cdot 10^{-3}$	$+0.13 \pm 0.09$	-0.414	0.103
Fairall 9	-0.73 ± 0.23	$+0.874$	0.026	-0.88 ± 0.15	$+0.961$	0.005
M81	$+0.25 \pm 0.27$	-0.273	0.184	$+0.20 \pm 0.05$	-0.791	$6 \cdot 10^{-4}$
MCG-6-30-15	-1.17 ± 0.32	$+0.831$	0.005	-0.43 ± 0.13	$+0.800$	0.009
Mrk 766	-0.38 ± 0.11	$+0.817$	0.007	-0.65 ± 0.12	$+0.915$	$7 \cdot 10^{-4}$
NGC 3516	-1.35 ± 0.19	$+0.984$	0.001	-1.18 ± 0.23	$+0.930$	0.004
NGC 4051	-0.64 ± 0.14	$+0.779$	$3 \cdot 10^{-4}$	-0.42 ± 0.26	$+0.387$	0.063
NGC 5506	-0.81 ± 0.11	$+0.945$	$6 \cdot 10^{-5}$	-0.04 ± 0.05	$+0.280$	0.251
NGC 5548	-1.33 ± 0.30	$+0.755$	$2 \cdot 10^{-4}$	-2.21 ± 0.80	$+0.580$	0.007

Table 5.1: Spectral variability parameter table for the sample of nearby sources studied in this chapter. We report both correlations between Γ and the $2-10$ keV flux as computed by `XSPEC`, using subscript "xs", and between Γ computed following Serafinelli et al. (2017b) with the tabulated flux $F_{\rm H}$ from the Serendipitous Source Catalogue, in band $2-12$ keV, using subscript "tab". For each method we list the spectral variability parameter β, the correlation coefficient r, and the probability of finding such correlation by chance $p(r > r_0)$, given by Eq. 4.5.18.

ratio ($F/\sigma(F) \lesssim 1$) and therefore were not included in the calculation of the photon index-flux correlation, therefore the considered number of observations is 17.

A very steep $\Gamma - \log F$ correlation is found, with $\beta = -1.33 \pm 0.30$, with high correlation coefficient ($r = 0.755$) and very low probability of random correlation ($p = 2 \cdot 10^{-4}$), as it is shown in Fig. 5.10. This does not agree with Sobolewska & Papadakis (2009), who found a rather flat correlation. This might be due to the fact that all RXTE observations were taken before the appearance of this absorber, while most of XMM-Newton observations are taken after its appearance.

5.3 Comparison of β using photon indices with approximate method

In addition to the above described method of calculating the photon indices Γ, we also wanted to compute both Γ and β using the approximate method described in Chapter 4 and Serafinelli et al. (2017b).

Most of the MEXSAS sources are too faint to have a detectable spectrum and spectral features, such as possible absorption features, soft excesses or hard excesses due to broadened iron line or reflection, are hidden and it is impossible to disentangle the intrinsic variability of the photon index with the apparent one due to the superposition of different spectral features.

As we saw on the previous section, these sources provide a very wide range of spectral features, from ionized absorbers to relativistic outflows or reflection on ionized disk, and

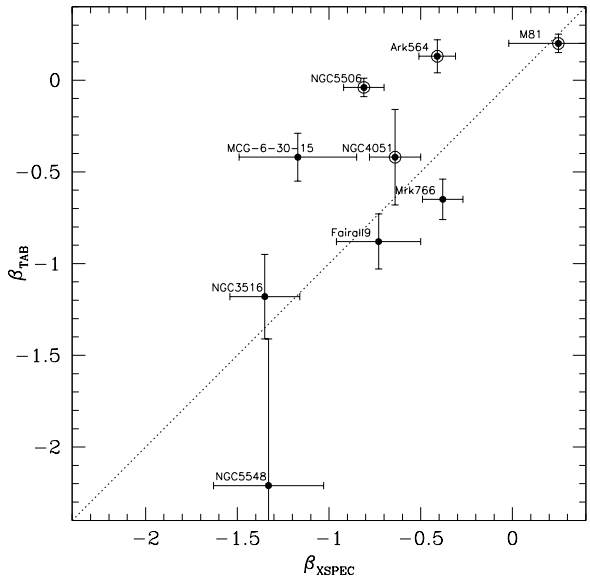

Figure 5.12: Comparison between the β as computed using best fit results from `XSPEC` and tabulated data. The dotted line represents the ideal case $\beta_{\rm xs} = \beta_{\rm tab}$, and the circles around some dots indicates that the probability of spurious correlation is not negligible for that source in either $\beta_{\rm xs}$ calculation (for M81) or $\beta_{\rm tab}$, see Table 5.1 for details. Apart from Ark 564, they follow the same trend with both methods. The outliers can be explained with the presence of spectral features such as prominent absorbers (NGC 5548), red wing (MCG-6-30-15) or reflection on ionized disk (NGC 5506). Ark 564 is affected by seriously piled-up spectra, possibly apparently hardening the spectrum at brighter phases.

therefore they are ideal to check the effect of this features on the approximated method that we developed in Chapter 4.

In order to achieve this goal, we cross-matched the 3XMM-DR6 Serendipitous Source Catalogue with a list of the sources used in this chapter, each with its own sky coordinates. The list of observations is not perfectly coincident with the one we studied in the previous section, due to the fact that some observations have been made public very recently and are only present in 3XMM-DR7, that was released during the writing of this dissertation. Then, we computed the photon indices following the method described in Sect. 4.2.

In Serafinelli et al. (2017b), we computed correlations between these Γs and the soft ($0.5-2$ keV) fluxes, mostly because the hard ($2-12$ keV) fluxes are affected by high measurement errors. An ideal comparison between the spectral variability parameters should be done using correlations with the same flux bands. Since we computed β by performing linear fits between Γ and $2-10$ keV fluxes, we should do the same for the tabulated photon indices, using the similar band H ($2-12$ keV), computed as in Eq. 4.3.8. For these sources, though, the measurement errors on the hard fluxes are not so large, and therefore we can calculate such $\Gamma - F_{\rm H}$ correlations.

The results of these correlations between tabulated data, as well as a summary of the correlations between best fit parameters, are reported in Table 5.1, while a plot with the

comparison of the β as computed using best fit parameters ($\beta_{\rm xs}$) and tabulated data ($\beta_{\rm tab}$) are reported in Fig. 5.12.

At first order, the values of $\beta_{\rm xs}$ and $\beta_{\rm tab}$ seem to be correlated. Five of these sources (Fairall 9, M81, Mrk 766, NGC 3516, and NGC 4051) are very close to the ideal case $\beta_{\rm xs} = \beta_{\rm tab}$, while other four (Ark 564, MCG-6-30-15, NGC 5506, and NGC 5548) are outliers. We speculate that the absorbing features of Mrk 766, NGC 3516 and NGC 4051 do not influence the computation of the photon index, while Fairall 9 and M81 are well represented by an almost-pure power law and therefore a similarity between the two spectral variability parameters was expected.

The spectra of MCG-6-30-15 notoriously present a red wing. Even though in the best fit calculation the red wing effect can be compensated by a larger iron line width, in tabulated data this broadened iron line could in principle generate a hard excess that can alter the calculation of Γ. This situation is similar to NGC 5506, where the broadening of the iron line has a different origin (close lines of ionized iron), but may produce a hard excess as well in the tabulated flux and produce smaller values of Γ.

The situation of NCG 5548 is clear by looking at Fig. 5.11. If we sample five points from the spectrum plotted in red and perform a linear fit, we will obtain a very low value of Γ, even though the actual value is not much different from the photon index of the spectrum plotted in black.

The case of Ark 564 is completely different. Since the spectrum of this source is a pure power law, it is somehow surprising that there is so much difference between the approximate method and the accurate one. We believe that the observed mismatch between the two calculation is mostly due to pile-up (Ballet, 1999). During the data reduction process (see Appendix A for details), we corrected the pile-up effect by selecting the area of the source in an annular region of external radius $40''$ and internal radius $10''$, to exclude data from the first diffraction angle, where pile-up is most probable. In the Serendipitous Source Catalogue, the pile-up is not corrected, but only flagged in the `PN_FLAG`, `M1_FLAG` and `M2_FLAG` entries. For Ark 564, the pile-up is flagged "True". The pile-up, if not corrected, produces a significant hard excess, that is greater in brighter phases, producing a systematic hardening at brighter phases. Since this source has a low absolute value of the spectral variability parameter (see Table 5.1), this effect is probably dominant over the intrinsic softer when brighter effect, producing an apparent harder when brighter trend that does not describe well the actual behaviour of the spectrum of the source. However, this effect is mostly negligible for fainter sources in the MEXSAS catalogue.

5.4 Discussion

In this chapter we have analyzed the spectral variability of 9 nearby bright Seyfert galaxies. Differently from Chapter 4, we have retrieved the full spectra of each observation of every source and made accurate spectral fits in the $3 - 10$ keV band.

We selected the same sample that was studied by Sobolewska & Papadakis (2009) in RXTE data, because it is very heterogeneous and presents almost every spectral feature, from ionized absorbers to broadened Fe Kα lines, due to either gravitational redshift or blending with close emission lines from reflection on an ionized disk. Two sources, NGC 3227 and NGC 3783, had less than five XMM-Newton observations, and therefore it was not possible to include them. We included an additional source, M81, a LLAGN for which it was recently found (Connolly et al., 2016, using Swift data) that the spectra follow the opposite, harder when brighter, trend, possibly due to its extremely low accretion rate ($\log L/L_{\rm Edd} \simeq -4.17$; Xu, 2011), that prevents the UV radiation from the disk of being the dominant seed photon source. This source therefore possibly has a different X-ray emission process.

With the exception of M81, we find a softer when brighter behaviour for every source, with spectral variability parameter ranging from -1.35 ± 0.19 to -0.38 ± 0.11.

Since we find this behaviour in all sources with $L/L_{\rm Edd} > 0.01$, independently of the shape of their spectrum, a first result of this study is that most likely the continuum spectral slope varies intrinsically, independently of the presence of absorbers and other features. That said, the $\Gamma - \log F$ correlation of NGC 5506 is very poor if the reflection spectrum is not taken into account, that suggests that the Compton hump plays a role in spectral variability.

Therefore, among the possible spectral variability drivers we listed in Sect. 2.4, an origin due to both continuum slope variation and superposition of continuum and reflection spectra appears to be favoured. When hard X-ray ($3 - 80$ keV) telescope NuSTAR (Harrison et al., 2013) will have a sufficient number of observations to perform a study such as this one, the role of reflection will be much clearer.

Concerning M81, we do find a negative correlation coefficient, which means positive β and hence harder when brighter trend, but it is very small ($r = -0.273$) and we have 18% probability to find such correlation by chance. This is due to the fact that all but one observations of this source was targeted at another object, and therefore the signal-to-noise ratio is quite bad (see Fig. 5.4), hence it is not possible to confirm a harder when brighter trend with sufficient confidence.

We also computed the spectral variability with the approximate method described in Chapter 4, by cross-matching 3XMM-DR6 with the list of sources studied here. We find very good agreement for five sources, while four of them do not agree with the β computed

by means of spectral fits.

For one of these sources (Ark 564) we blame seriously piled-up spectra, that hardens the spectrum, especially at brighter phases. This effect does not concern any source of the MEXSAS sample, since they are mostly luminous quasars at high distance, with a much lower photon count, which makes pile-up phenomenon less likely.

For the other three sources, the mismatch is due to spectral features that the tabulated data cannot possibly take into account, such as Fe Kα line red wing due to gravitational redshift (MCG-6-30-15), prominent absorbers (NGC 5548) or unaccounted reflection spectra (NGC 5506). When sampling just five points in the spectra of these sources, the spectra themselves appear to critically flatten, and the photon indices computed with such five points give unreliable results, in most cases $\Gamma < 1.1$.

In Chapter 4, we estimated that the number of quasars that are not correctly represented by a pure power law spectrum are $\sim 10\%$ of the sources and we considered this subset as negligible in the ensemble $\Gamma - \log F$ correlation. In future ensemble spectral variability studies, a more accurate ensemble value of β might be obtained, by excluding every observation with $\Gamma \lesssim 1.1 - 1.3$.

Chapter 6

THE MULTI-LAYER OUTFLOW STRUCTURE OF PG 1114+445

6.1 The source

PG 1114+445 is a type-1 quasar at $z = 0.144$ (Hewett & Wild, 2010), with SMBH mass $M \simeq 5.9 \cdot 10^8 M_\odot$, derived from single-epoch virial technique and bolometric luminosity $L \simeq 5.5 \cdot 10^{45}$ erg s^{-1} (Shen et al., 2011). An ASCA observation taken in 1996 showed the presence of an ionized absorber in the soft X-ray spectrum of this source, interpreted as photoelectric absorption edges of O VII and O VIII (George et al., 1997). Moreover, a detection of an absorption line around the Fe Kα band was claimed, suggesting the presence of mildly relativistic high-ionization outflow with $v \sim 0.1c$, although the low resolution of the instrument did not allow to assess the presence of the lines with high confidence. In parallel, a 1996 Hubble Space Telescope observation was able to detect an ionized, ultraviolet (UV) absorption line, associated with the soft X-ray absorber (Mathur et al., 1998). The line-of-sight velocity was found to be $v \simeq 530$ km s^{-1}, computed from narrow absorption feature in both C IV and Lyα broad lines. Given the rarity of detecting both soft X-ray and UV absorption features, the authors concluded that it was probably originating from the same material.

In 2002, a much higher quality spectra was made available by a 44ks XMM-Newton observation, and a second X-ray absorber was found in the spectrum of the source (Ashton et al., 2004; Piconcelli et al., 2005), as well as a black-body soft excess (Piconcelli et al., 2005).

As already mentioned in Chapter 4, in an ensemble work on a sample of SDSS-selected quasars in XMM-Newton archival data (Serafinelli et al., 2017b), we found 11 additional

Instrument	OBSID	ID	Start date	Duration (s)	Exposure (s)	Counts
ASCA	74072000	A	1996-05-05	151175	$\sim$ 65000	13126
EPIC-pn	0109080801	0	2002-05-14	43512	32500	23462
EPIC-pn	0651330101	1	2010-05-19	37816	20550	7657
EPIC-pn	0651330201	2	2010-05-21	34264	9824	4248
EPIC-pn	0651330301	3	2010-05-23	35764	5271	1846
EPIC-pn	0651330401	4	2010-06-10	41362	10740	5742
EPIC-pn	0651330501	5	2010-06-14	37055	6613	3247
EPIC-pn	0651330601	6	2010-11-08	34441	18500	17359
EPIC-pn	0651330701	7	2010-11-16	34260	16240	10611
EPIC-pn	0651330801	8	2010-11-18	34343	20350	10478
EPIC-pn	0651330901	9	2010-11-20	34166	21350	13529
EPIC-pn	0651331001	10	2010-11-26	28864	17660	9462
EPIC-pn	0651331101	11	2010-12-12	28914	13710	7927

Table 6.1: Data reduction table for PG 1114+445. In all the spectra, a binning of a minimum of 50 counts per bin has been used, with the only exception of the ASCA observation, for which the data was already reduced. The ASCA observation includes all four cameras (sis0, sis1, gis2 and gis3). The two sis cameras have 61000 s exposure, while the two gis cameras have exposures of 68400 s. We report an average value in the table. The ID column shows a one-digit code for each observation, introduced for simplicity: A stands for ASCA, the 2002 observation was labelled 0, and a number from 1 to 11 was assigned to each of the 2010 campaign observations. Observations 2, 3, 4 and 5 are affected by high particle background. Such high background is responsible for the low number of counts of these observations.

archival spectra, which spectral analysis, together with a new analysis of both the 2002 XMM-Newton and the 1996 ASCA observations, is presented in the present chapter (Serafinelli et al., 2018b).

6.2 Data reduction

XMM-Newton observed PG 1114+445 on twelve occasions between 2002 and 2010. In May 2002 it was observed for $\sim$ 44ks (OBSID 0109080801), and then a campaign of 11 observations of $\sim$ 380 ks total duration was performed between 2010 May 19th and 2010 December 12th (sequential OBSIDs from 0651330101 to 0651331101). For simplicity, we introduced a one-digit marker for each observation: A marks the ASCA observation, OBSID 0109080801 is Obs. 0, while a number from 1 to 11 was given to all observations of the 2010 campaign. Details on duration and exposure of the single observations are shown in Table 6.1. EPIC-pn and MOS event lists were extracted by using the standard System Analysis Software (SAS, version 16.0.0) tools `epproc` and `emproc`. As shown in Table 6.1, all observations are affected, with different extent, by background particle flaring (De Luca & Molendi, 2004), particularly Obs. 2 to 5, and therefore the appropriate filtering was applied (see Appendix A for details). After checking that no pile-up correction is needed

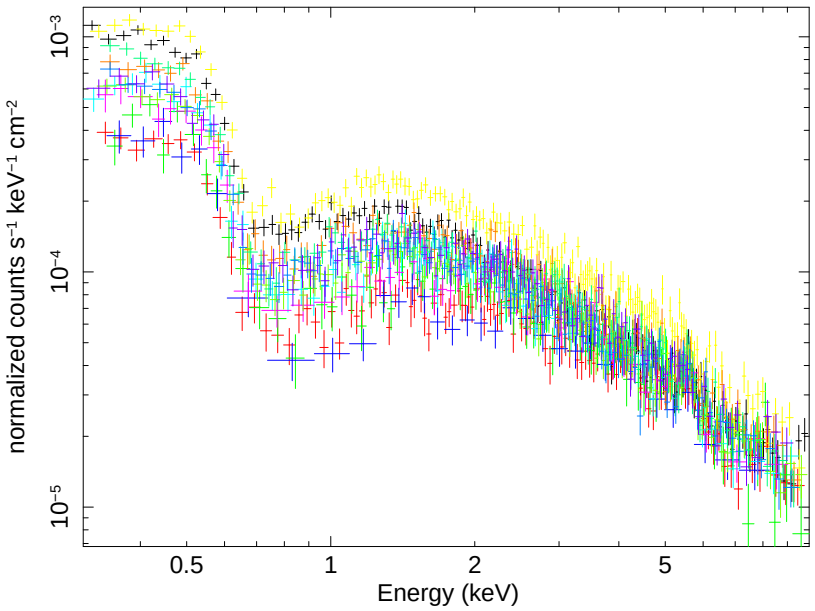

Figure 6.1: Superposition of all twelve XMM-Newton observations of PG 1114+445. Each color represents a different observation.

for any of these observations, we extracted the spectra by selecting a region in the CCD image of 40″ radius around the source, and the background by extracting a source-free region of the same size. Response matrices and auxiliary response file were generated using respectively SAS tools `rmfgen` and `arfgen`. Finally, we grouped the spectra by allowing 50 counts for each spectral bin using `specgroup`, forcing a minimum energy width of 1/5th of the Full Width Half-Maximum (FWHM) resolution at the central photon energy of the bin, using the command `oversample`.

Moreover, a $\sim$ 150 ks ASCA observation was performed 1996 May 5th (sequence number 74072000). In order to compare with previous results obtained with such data (George et al., 1997), we retrieved the already reduced spectral products from online archive[1]. All the four cameras (sis0, sis1, gis2 and gis3) were used, and the exposure of the two sis cameras is 61 ks, while the gis cameras exposure is 68.4 ks.

Given the low counts of Obs. 2 and 3, we decided to merge them with Obs. 1, since they are very close in time and flux, and we call this merged spectrum 1+2+3. With the same motivation we merged Obs. 4 and 5 into spectrum 4+5 and Obs. 8 and 9 into spectrum 8+9.

[1] https://heasarc.gsfc.nasa.gov/FTP/asca/data/tartarus/products/74072000/74072000_gsfc.html

ID	$N_{\rm H}^{(1)}/10^{21}$ cm^{-2}	$\log\xi^{(1)}$/erg cm s^{-1}
A	7.5*	0.35*
0	$7.7^{+0.3}_{-0.4}$	$0.34^{+0.01}_{-0.01}$
1+2+3	7.5**	0.35**
4+5	$6.9^{+0.7}_{-3.1}$	≤ 0.32
6	$7.5^{+0.6}_{-0.5}$	$0.35^{+0.04}_{-0.02}$
7	$7.9^{+0.5}_{-0.3}$	$0.33^{+0.01}_{-0.01}$
8+9	$7.4^{+0.5}_{-0.5}$	$0.34^{+0.02}_{-0.01}$
10	$7.6^{+0.6}_{-1.0}$	$0.37^{+0.06}_{-0.03}$
11	7.5**	0.35**

Table 6.2: Parameters of the "first" absorber, i.e. Abs. 1. The redshift of the absorber is found to be about the same as the cosmological redshift of the source. Therefore, we assume that this absorber is the same that was identified by both George et al. (1997) and Mathur et al. (1998), for which a velocity of $\sim$ 530 km s^{-1} was estimated, by measuring an absorption feature in both Lyα and C IV lines. *For the ASCA observation, the instrument is not able to resolve both soft X-ray absorbers, therefore we fixed the parameters of this one to the average values of the other XMM-Newton observations. **For these observations, the low number of counts does not allow to find an adequate fit for this absorber, and therefore we fixed the parameters to the average values found in the other EPIC-pn observations.

6.3 Spectral analysis

As a baseline model for the analysis of this source, we used a similar model to the one that was used for the 2002 observation by Piconcelli et al. (2005): a power law with Gaussian iron line, black body soft excess and two ionized absorbers.

In such work, the model `absori` was used to describe the ionized absorbers, while for this work we used a a proper photoionization code, `Xstar` (Kallman & Bautista, 2001), to derive detailed absorption grids to fit the data. For these two absorbers, following Tombesi et al. (2011), we derived an `Xstar` table, with SED described by a power law with $\Gamma = 2$ in the $10^{-1} - 10^{6}$ eV band, and cut-off energy assumed to be at $E_c > 100$ keV, following Haardt & Maraschi (1991). Solar abundances from Asplund et al. (2009) were assumed. This photoionization code takes into account all known resonance absorption lines and edges for every element up to $Z = 30$. The turbulent velocity for this grid was set to 100 km s^{-1}, and a unitary covering factor was chosen. The free parameters of this grid are the

hydrogen column density of the absorber $N_{\rm H}$, the ionization parameter ξ (see Eq. 1.3.11), and the observed redshift z_o of the absorber.
We indicate the cosmological redshift of the source z_c, the observed absorber redshift z_o and the Doppler shift of the absorber in the source rest-frame z_a are related by:

$$1 + z_o = (1 + z_a)(1 + z_c), \tag{6.3.1}$$

and the velocity of the outflow will be therefore

$$1 + z_a = \sqrt{\frac{1 - v/c}{1 + v/c}}. \tag{6.3.2}$$

In case of outflows, the Doppler shift will be a blueshift, and $v/c > 0$.
One of the two absorbers, that we labelled with superscript (1) (the "first" absorber, i.e. Abs. 1) has very small variability (see Table 6.2), and a redshift very close to the cosmological redshift of the source $z_o \simeq z_c$ and therefore we fixed the redshift of the absorber to the value $z_c = 0.144$, hence we assumed that the absorber can be identified with the warm absorber found in both X-rays (George et al., 1997) and UV (Mathur et al., 1998), who computed the velocity of the material, $v^{(1)} \simeq 530$ km s^{-1}. The typical values of the parameters of this absorber are $N_{\rm H} \simeq 7.5 \cdot 10^{21}$ cm^{-2} and $\log \xi \simeq 0.35$ erg cm s^{-1}.
The other absorber, labelled with superscript (2) (the "second" absorber, i.e. Abs. 2) appears to be more variable (see Table 6.3), even though the variations of the velocity are within the errors. Its average value is $v^{(2)} = 0.104^{+0.043}_{-0.039}c$, with c being the speed of light. Since the standard deviation is about half of the mean errors ($\sigma \sim 0.015c$), we assume that the absorber does not change and we report the mean value of the errors of the best fit. The ionization parameter $\log \xi$ varies from less than 0.12 to 1.51, way smaller than the expected ionization parameters for such high velocities.
For two observations (XMM-Newton Obs. 6 and 8+9) we also find evidence of the presence of a third absorber with higher ionization state, i.e. Abs. 3. To model this one we used a similar `Xstar` grid as the other absorbers, only setting the turbulence velocity to 10^3 km s^{-1}, to take into account the broadening of the Fe XXV and Fe XXVI lines. For the ASCA observation, we find an F-test probability of 80%, but given the claim of George et al. (1997) and the much lower resolution of the instruments of this telescope, we add a third absorber also to this observations. Obs. 6 has F-test probability of 99.9%, while F-test probability for observation 8+9 is 95%.
The average value of the ionization parameter is $\log \xi \simeq 4.08$ erg cm s^{-1}, and the average value of the velocity is $v^{(3)} = (0.127 \pm 0.015)c$. In this case we reported the standard

ID	$N_{\rm H}^{(2)}/10^{21}$ cm^{-2}	$\log \xi^{(2)}$/erg cm s^{-1}	$z_o^{(2)}/10^{-2}$	v/c
A	$7.8^{+0.6}_{-1.4}$	$0.34^{+0.63}_{-0.06}$	$+3.3^{+3.9}_{-2.4}$	$0.102^{+0.052}_{-0.032}$
0	$1.8^{+0.6}_{-0.5}$	$0.87^{+0.16}_{-0.36}$	$+4.6^{+1.6}_{-3.1}$	$0.089^{+0.021}_{-0.040}$
1+2+3	$6.4^{+2.5}_{-1.4}$	$1.18^{+0.20}_{-0.14}$	$+3.3^{+1.4}_{-3.2}$	$0.102^{+0.019}_{-0.042}$
4+5	$5.5^{+3.8}_{-1.2}$	$0.44^{+0.43}_{-0.09}$	$+1.1^{+3.6}_{-4.1}$	$0.123^{+0.048}_{-0.056}$
6	$2.8^{+0.4}_{-0.5}$	≤ 0.12	$+0.8^{+3.7}_{-5.5}$	$0.126^{+0.050}_{-0.074}$
7	$7.3^{+5.1}_{-3.9}$	$1.51^{+0.23}_{-0.45}$	$+4.1^{+2.1}_{-2.4}$	$0.094^{+0.027}_{-0.031}$
8+9	$2.9^{+0.5}_{-0.5}$	$0.64^{+0.29}_{-0.15}$	$+1.8^{+1.2}_{-1.4}$	$0.116^{+0.029}_{-0.019}$
10	$2.7^{+1.3}_{-0.7}$	$0.63^{+0.42}_{-0.36}$	$+3.2^{+3.9}_{-4.6}$	$0.103^{+0.051}_{-0.060}$
11	$5.7^{+2.6}_{-1.7}$	$1.24^{+0.23}_{-0.25}$	$+5.4^{+4.2}_{-2.1}$	$0.082^{+0.054}_{-0.027}$

Table 6.3: Parameters of the "second" absorber. In this case the average observed redshift of the absorber is significantly lower than the cosmological redshift of the source $z_c = 0.144$. At first order, the variations of $z^{(2)}$ are all within the error (see Fig. 6.2). Column densities and ionization parameters are more variable instead. The velocity of the absorber, in units of v/c, with c the speed of light, is also shown.

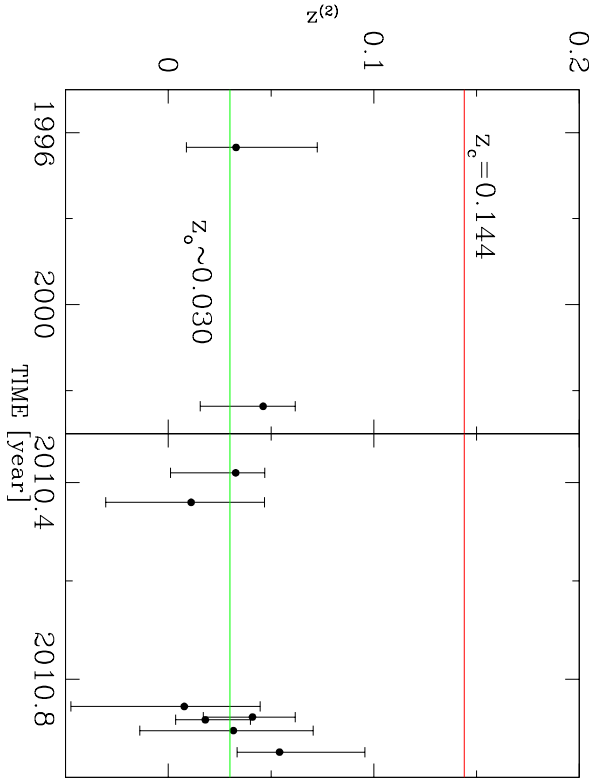

Figure 6.2: Time dependence of the observed redshift of Abs. 2. The variability is very small, most of the points are compatible within the error with the average value (the green line at $z = 0.030$). The red line represents the cosmological redshift of the source, $z_c = 0.144$.

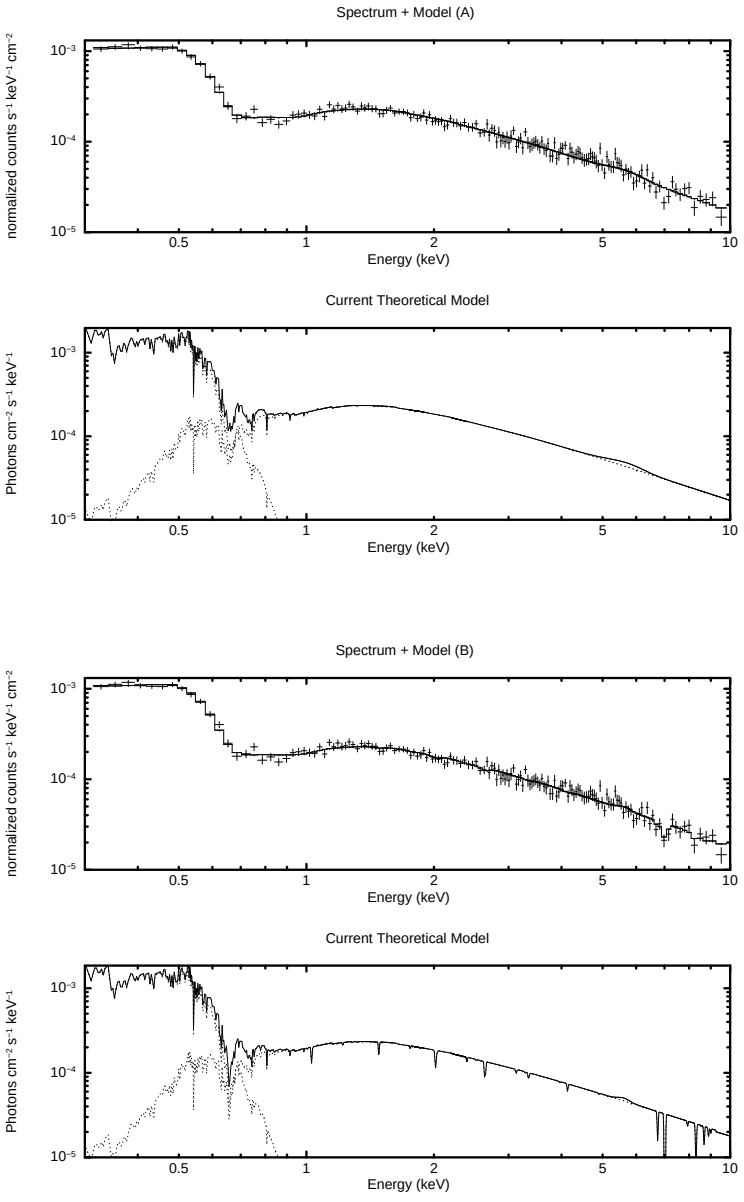

Figure 6.3: *Top.* Spectrum and best fit model of Obs. 6, using Model (A), consisting of two absorbers, power law, iron line and black body soft excess. *Bottom.* Same figure, using Model (B) with three absorbers.

ID	$N_{\rm H}^{(3)}/10^{21}$ cm^{-2}	$\log\xi^{(3)}$/erg cm s^{-1}	$z_o^{(3)}/10^{-2}$	v/c
A	≥ 440	$3.83^{+0.21}_{-0.21}$	$+0.2^{+0.5}_{-0.5}$	$0.132^{+0.007}_{-0.008}$
6	≥ 289	$4.42^{+0.18}_{-0.33}$	$-0.6^{+0.6}_{-0.5}$	$0.139^{+0.009}_{-0.007}$
8+9	88^{+330}_{-61}	$3.98^{+0.49}_{-0.30}$	$2.4^{+0.9}_{-0.9}$	$0.110^{+0.011}_{-0.012}$

Table 6.4: Parameters of the "third" absorber. For the ASCA observation and XMM-Newton OBSID 0651330601 we were only able to report a lower limit for the column density. The average value of the ionization parameter is $\log\xi \simeq 4.08$ erg cm s^{-1}, and the average value of the observed redshift of the absorber is $z_o \simeq 0.0067$. The velocity of this absorber is also reported in units of v/c.

deviation as error, because in this case it is larger than the mean value of the best fit errors ($\sim 0.009c$). The parameters of this third absorber are reported in Table 6.4.
In all three cases, the addition of this third absorber and the new fit produce irrelevant changes on the parameters of the other two absorbers, as well as the continuum and black body ones. Finally, in Table 6.5 we report the black body temperature and photon index, as well as the normalized χ^2, of the best fit for each observation. The two velocities are compatible within the errors.
The values of v/c and ξ for Abs. 1 (Table 6.2) and Abs. 3 (Table 6.4) are consistent with the Tombesi et al. (2013) picture of - respectively - warm absorbers and ultra-fast outflows (see Fig. 2.5). As for Abs. 2 (Table 6.3), its values are not consistent with Fig. 2.5, since high-velocity outflows are usually paired with much higher values of the ionization parameter ξ. This suggests that the nature of this absorber is different from the other ones. Since Tombesi et al. (2013) suggested that warm absorbers and ultra-fast outflows are different manifestations of the same large scale outflow structure, it is likely that Abs. 2 represents a byproduct of the interaction between these two types of absorber instead, i.e. the ultra-fast outflow shocking and/or entraining the interstellar matter.

6.4 Spectral variability

We also computed the spectral variability of PG 1114+445, using the method described in Sect. 5.1. We took the best fit results of both photon index (see Table 6.5) and normalization to compute the flux in the $2-10$ keV band. Then we performed a linear fit between Γ and $\log F$ and computed β according to Eq. 4.0.1.
We find a positive correlation ($r = 0.581$) and a negative $\beta = -0.65 \pm 0.35$, with probability of spurious correlation $p = 0.05$, given by Eq. 4.5.18. This means that the source follows a softer when brighter trend. The $\Gamma - \log F$ correlation is shown in Fig. 6.5.

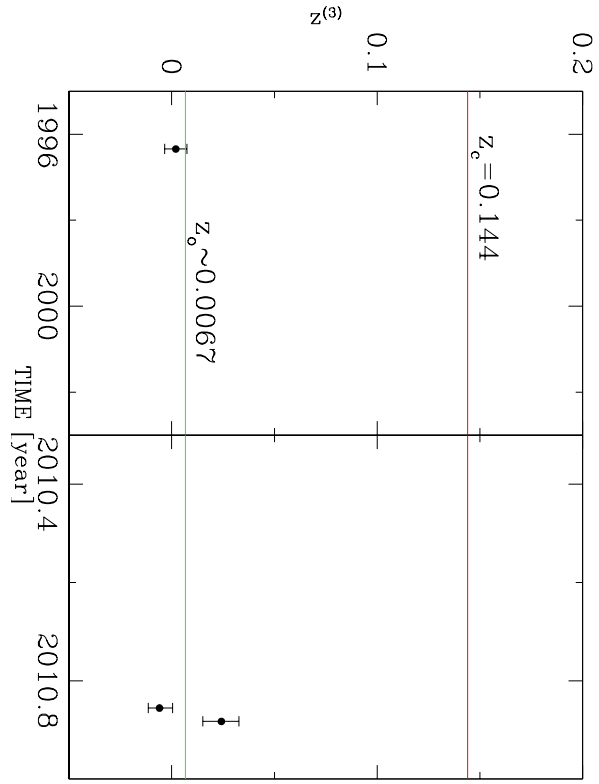

Figure 6.4: Time dependence of the observed redshift of the "third" absorber. The variability is very small also for this absorber, with average value give by the green line at $z_o = 0.0067$. The red line represents the cosmological redshift of the source, $z_c = 0.144$.

ID	$kT/10^{-2}$ keV	Γ	χ^2/dof	Model
A	$6.4^{+1.2}_{-1.1}$	$1.84^{+0.05}_{-0.08}$	410/381	B
0	$6.0^{+0.2}_{-0.3}$	$1.68^{+0.04}_{-0.02}$	177/161	A
1+2+3	$7.0^{+0.2}_{-0.2}$	$1.44^{+0.04}_{-0.02}$	246/242	A
4+5	$6.1^{+0.6}_{-0.7}$	$1.68^{+0.05}_{-0.06}$	126/147	A
6	$5.5^{+0.3}_{-0.3}$	$1.62^{+0.03}_{-0.03}$	137/148	B
7	$5.5^{+0.6}_{-0.3}$	$1.63^{+0.04}_{-0.07}$	112/118	A
8+9	$6.3^{+0.3}_{-0.4}$	$1.53^{+0.02}_{-0.02}$	327/366	B
10	$6.7^{+0.9}_{-0.6}$	$1.58^{+0.05}_{-0.06}$	98/109	A
11	$6.7^{+0.2}_{-0.3}$	$1.59^{+0.09}_{-0.06}$	131/105	A

Table 6.5: Black body temperatures and photon indices of each observation. For each observation we list the normalized χ^2/dof of the best fit, that refers to the model with two (A) or three (B) absorbers. Given that the addition of a third absorber does not change these parameters significantly, we only made distinction by listing the model we used.

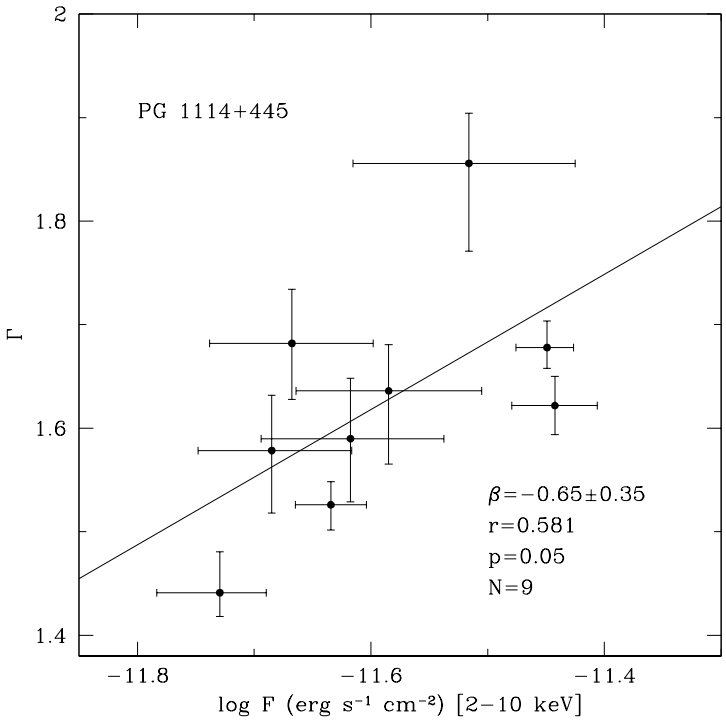

Figure 6.5: $\Gamma - \log F$ correlation of PG 1114+445. We find $\beta < 0$ and therefore softer when brighter behaviour.

If we calculate β, by performing linear fits between the approximate photon indices that we computed in Chapter 4 and the hard fluxes ($2 - 12$ keV) from the serendipitous source catalogue, we obtain $\beta = -0.88 \pm 0.25$ with higher correlation $r = 0.746$ and lower probability $p = 0.003$. However, the values of Γ found with this method, due to the complex nature of the spectrum of this source, are very low, in the range $\Gamma \sim 0.8 - 1$, much lower than the ones in Table 6.5. Therefore, the spectral variability parameter $\beta_{\rm tab}$, obtained with approximate photon indices, is not reliable.

6.5 Discussion

We have analyzed 13 observations of type-1 QSO PG 1114+445, one taken in 1996 by ASCA and 12 observations taken by XMM-Newton in 2002 and 2010.
Three absorbers are present in the spectra of this source: a low velocity ($v \sim 530$ km s^{-1}), low ionization ($\log \xi \sim 0.35$ erg cm s^{-1}) one, one with high velocity ($v \sim 0.104c$) and low ionization ($\log \xi \sim 0.80$ erg cm s^{-1}) and, for three of these observations, we find a typical ultra-fast outflow with $v \sim 0.127$ and $\log \xi \sim 4.08$ erg cm s^{-1}.
In Compton-thick AGNs, the central emission is believed to be heavily absorbed (see left panel of Fig. 6.6), and also winds are still too weak to blow out the gas. In luminous,

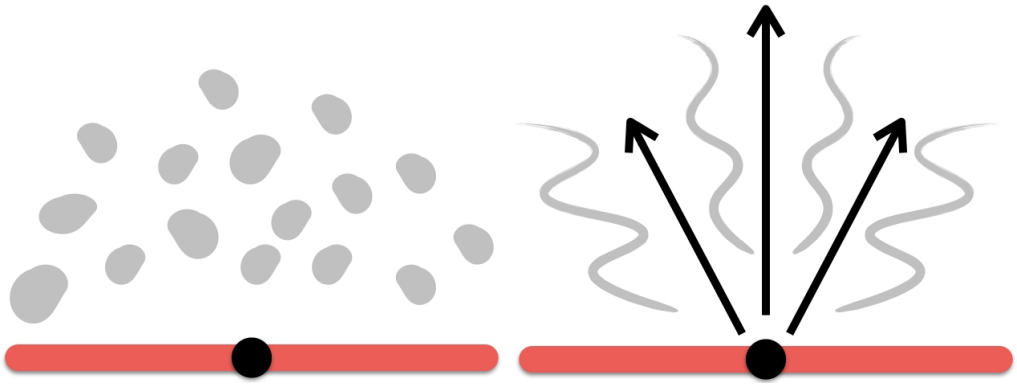

Figure 6.6: *Left.* Initial Compton thick-like situation where the wind is too weak to blow the clouds away, and the absorbing material has velocities of the order of $\sim 100 - 1000$ km s^{-1}. *Right.* Final quasar-like situation in which the ultra-fast wind has blown up the absorber.

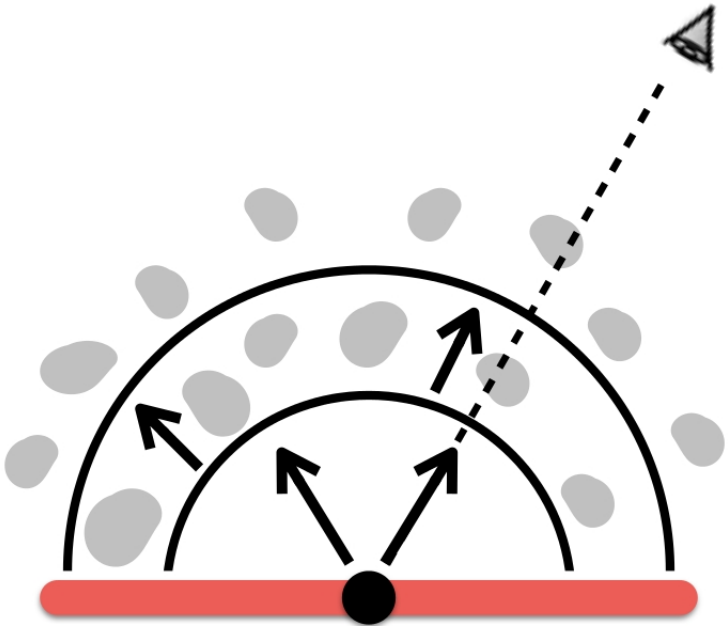

Figure 6.7: Interpretation of the situation that we observe in PG 1114+445. We believe that a UFO (inner shell, Abs. 3) is blowing the warm absorber (outer shell, Abs. 1) at a moderately relativistic velocity, $v \simeq 0.127c$ and that the intermediate shell is likely to be shocked interstellar matter (Abs. 2) that is being accelerated at velocities comparable to the one of the UFO.

unabsorbed quasars (Fig. 6.6, right panel), on the other hand, UFOs are probably responsible for the absence of prominent absorbers. Indeed, UFOs are believed to be very important for the feedback process in the galaxy evolutionary scenario, blowing out and dispersing the ISM at kpc scales (e.g., Zubovas & King, 2012; Wagner et al., 2013).

Our interpretation of the observational evidence of the spectra of PG 1114+445 is shown in Fig. 6.7. Close to the supermassive black hole, there is an inner shell with an ultra-fast wind of high ionization and moderately relativistic velocity (Abs. 3, Table 6.4), produced in the innermost parts of the AGN, perhaps by magnetic processes (Fukumura et al., 2015, 2017).

The fast outflow with lower ionization, i.e. Abs. 2, can be associated with the UFO shocking on and/or entraining the ISM, which is suggested by the fact that the values of v/c and ξ are not consistent with the usual $v - \xi$ correlation (Tombesi et al., 2013, see also Fig. 2.5). Its high velocity, indeed, is comparable, within the errors, with the one of the UFO, even though the much lower ionization state suggests that the UFO is "pushing" on lower ionization gas clumps, located at higher distances from the supermassive black hole (e.g., Pounds & Vaughan, 2011a).

The outer shell is the ISM (Abs. 1, Table 6.2). Given its distance, this gas has not yet felt the effect of the pushing from the UFO.

So far this is the first simultaneous detection of all three kinds of absorbers in the same source and it may represent a promising step forward in the understanding of these physical phenomena in Active Galactic Nuclei.

Future multi-wavelength observations of this source, using observations with longer exposures from XMM-Newton, as well as other telescope facilities such as Chandra, NuSTAR, Hubble Space Telescope and more, are going to further clarify the nature of this possible multi-layer structure of absorbers around the accretion disk of this source.

SUMMARY AND CONCLUSIONS

In this thesis I have investigated the X-ray spectral variability of various types of Active Galactic Nuclei.

In the first part of the thesis, I have created the Multi-Epoch XMM Serendipitous AGN Sample (MEXSAS, Vagnetti et al., 2016), which is made up of 7 837 observations from 2 700 sources. This sample was created by cross-matching the 3XMM-DR5 Serendipitous Source Catalogue (Rosen et al., 2016) with two quasar catalogues, SDSS-DR7Q (Schneider et al., 2010) and SDSS-DR12Q (Pâris et al., 2017). I have developed (Serafinelli et al., 2017b) an approximate technique to derive the photon index of each observation, by assuming that the spectrum of the source is a pure power law, both locally and globally, and computing linear spectral fits between the logarithm of the five flux points listed in 3XMM-DR5, and the logarithm of the associated energy. By comparing our Γs with a subset of coincident data with the photon index catalogue of Corral et al. (2015), computed with more accurate spectral fits, we find a good aggreement. By assuming that the spectral shapes of the subset of coincident data is distributed as the whole MEXSAS sample, I estimated that a pure power law spectrum well describes $\sim 90\%$ of the X-ray observations of the catalogue, which is the result found by Corral et al. (2015) for their whole sample.

I computed the spectral variability parameter, $\beta = -\Delta\Gamma/\Delta \log F$, of the ensemble, using the soft $(0.5 - 2$ keV) flux, due to the large measurement errors on the hard fluxes. I find $\beta = -0.69 \pm 0.03$ with correlation coefficient $r = 0.293$ and negligible probability of finding such correlation by chance. The negative sign of β means that the ensemble spectral variability of the sample is softer when brighter, thus implying that the bulk of the MEXSAS sources follow such trend, therefore extending the result that was found on Seyfert galaxies by Sobolewska & Papadakis (2009) in RXTE data to quasars with larger ranges of luminosity and redshift.

Brighter sources appear to be more correlated than fainter ones, and this results in an

apparent dependence of β on the average flux of the source. This was taken into account when studying MEXSAS2 (Vagnetti et al., 2018), in which I replaced each data point with 10^4 simulated points, with Gaussian distributions around the actual data point itself. I computed several fits (Serafinelli et al., 2017a) and averaged the result, which resulted in an almost complete removal of this bias (see Fig. 4.13).

No clear trend was found for the spectral variability parameter β with either redshift, X-ray luminosity, black hole mass or Eddington ratio. This means that the process that produces the observed spectral variability is likely the same for the majority of the sources. No significant difference in β from the ensemble value is found for a subset of known BALQSO, while radio-loud sources show a sightly lower absolute value of the spectral variability, possibly due to contamination from additional X-ray emission from the jet.

I also found softer when brighter trends for nine individual sources, one of which (PG 1114+445) was not considered, due to its complex spectrum, which is clearly not possible to approximate as a pure power law. The values of β range from $\beta = -0.80 \pm 0.06$ to the extremely steep relation $\beta = -3.54 \pm 0.54$. This large range might be due to various effects, such as inclination, from which the reflection spectra is clearly dependent, black hole spin through the broadening of Fe Kα line, presence of soft excess or hidden unresolved absorbers. Perhaps future X-ray telescopes such as XARM (Takahashi et al., 2014), eROSITA (Merloni et al., 2012) or Athena (Nandra et al., 2013) will provide an answer to this puzzling question.

I have also studied the spectral variability of 9 nearby sources (Serafinelli et al., 2018a) by performing accurate spectral fits in the $3 - 10$ keV band, chosen from the sample already studied by Sobolewska & Papadakis (2009) in RXTE data, plus M81 to investigate a possible harder when brighter trend, already found by Connolly et al. (2016) in Swift data. With the exception of M81, we find a softer when brighter trend for every source, with β ranging from $\beta = -0.41 \pm 0.10$ to $\beta = -1.35 \pm 0.19$. This result is independent of the spectral features of the source, which means that the slope of the continuum is likely intrinsically variable. However, if we do not take reflection into account in NGC 5506, the $\Gamma - \log F$ correlation becomes rather poor, while it is highly correlated otherwise. This suggests that reflection plays a significant role as well in the observed spectral variability. It appears then that the model predicting that the observed spectral variability is due to both intrinsic variations of the photon index and superposition with a constant reflection component is favoured. However, when hard X-ray telescope NuSTAR (Harrison et al., 2013) will have a sufficient number of observations of single sources to perform a an analysis such as this one, the role of reflection will be much clearer.

I compared then these values of β with their counterpart, computed from approximate photon indices, following Serafinelli et al. (2017b). I find agreement for five sources, while there is a mismatch for the other four. While the mismatch in one of the sources (Ark

564) is mainly due to piled-up data, for the other three sources the mismatch is due to prominent spectral features, such as absorbers (NGC 5548), red wing (MCG-6-30-15) and reflection (NGC 5506). These spectral features have the effect of flattening the continuum to photon indices of $\Gamma \lesssim 1.1$. Since these sources are part of the putative 10% of observations in the MEXSAS sample, it is recommended that future ensemble spectral variability studies should improve the ensemble result by removing all photon indices in the range $\Gamma \lesssim 1.1 - 1.3$. In this way, the spurious 10% of the sources will be taken into account.
Finally, I analyzed 13 spectra (one from ASCA taken in 1996, and 12 from XMM-Newton taken in 2002 and 2010) of the source I discarded in Serafinelli et al. (2017b), PG 1114+445 (Serafinelli et al., 2018b). Following Piconcelli et al. (2005), I developed a model with two ionized absorbers, black body soft excess, power law and Gaussian line. I find that all the observations are well fitted by a low-ionization ($\log \xi \sim 0.35$ erg cm s^{-1}), slow (~ 530 km s^{-1}) warm absorber, one absorber with low-ionization ($\log \xi \sim 0.8$ erg cm s^{-1}) and high velocity ($v \sim 0.104c$), power law, iron line and black body soft excess. For three of these observations, I also find a high-ionization ($\log \xi \sim 4.08$ erg cm s^{-1}), ultra-fast ($v \sim 0.127c$) outflow (UFO).
I interpret this result as the superposition of three different absorbing layers (see Fig. 6.7). According to this interpretation, the inner layer is an accretion disk ultra-fast wind, represented by the typical high-ionization UFO, that is shocking and/or entraining the interstellar matter (ISM), "pushing" the outer low-ionization layer to comparable velocities with the one of the UFO. This layer is the observed low-ionization, fast outflow seen in the soft X-rays. The warm absorber likely represents an outer layer of ISM that has not yet felt the effect of the pushing UFO. It is the first time that all three kind of absorbers are detected in the same source.

Appendix A

XMM-NEWTON DATA REDUCTION PIPELINE

The reduction of the XMM-Newton spectra was performed by means of the SAS software package[1].
Once the software is installed, before doing any actual analysis, it is important to download the latest Current Calibration File (`ccf`) in a repository folder. Provided that the `ccf`s are placed in the `/sasworkspace/ccf/` folder, the calibration files can be updated by running the code

```
rsync -v -a --delete --delete-after --force --include='*.CCF' --exclude='*/'
xmm.esac.esa.int::XMM_CCF /sasworkspace/ccf/
```

A.1 SAS start-up and event list production

The data was downloaded from the XMM-Newton Science Archive (XSA[2]) in their raw format `odf` and placed in the `/sasworkspace/odf/` folder. Once the `odf`s are placed in the work folder, we need to launch the software and trigger the SAS startup process:

```
export SAS_ODF=/sasworkspace/odf/
export SAS_CCFPATH=/sasworkspace/ccf/
cifbuild
export SAS_CCF=/sasworkspace/ccf.cif
odfingest
```

[1] https://www.cosmos.esa.int/web/xmm-newton/sas
[2] http://nxsa.esac.esa.int/nxsa-web

These four lines identify the positions of the raw `odf` data and the `ccf`s. The `cifbuild` task then creates a Calibration Index File `ccf.cif`, in which the correct calibration files for the specific observation we are analysing are selected, which position needs to be identified in the work folder.
The `odfingest` task then creates a summary file for the calibrated `odf`s, which will be named the following way:

```
rrrr_iiiiiijjkk_SCX00000SUM.SAS
```

where `rrrr` is a four digit number that identifies the revolution number and `iiiiiijjkk` is the observation identification number (`OBSID`). This file must be now identified using the line:

```
export SAS_ODF=/sasworkspace/rrrr_iiiiiijjkk_SCX00000SUM.SAS
```

After all the start-up process is done, data from the EPIC-pn and the two MOS cameras will be processed using the tasks:

```
epproc
emproc
```

The first line processes data from the EPIC-pn camera, in order to obtain calibrated and concatenated event lists, while the second command executes the same task for both MOS1 and MOS2 cameras. For most of the practical cases no additional commands are needed, although in some cases the default options are not the most comfortable ones. For instance, in case we are looking at an offset source (i.e., not the target of the observation) it is better to change the reference pointing for the calculation of the sky coordinates to a value of our choice:

```
epproc referencepointing=user ra=340.663939 dec=29.7253637
```

The output of these commands are the following:

```
rrrr_iiiiiijjkk_AttHk.ds
rrrr_iiiiiijjkk_CAM_blll_zz_BadPixels.ds
rrrr_iiiiiijjkk_CAM_blll_ImagingEvts.ds
```

Again, `rrrr` is the revolution number and `iiiiiijjkk` is the `OBSID`. `CAM` is replaced by an identifier of the camera, `EPN`, `EMOS1` or `EMOS2`, `b` can be either `S` in case the observation is scheduled or `U` in case of an unscheduled one, `lll` is the exposure identifier, and `zz` is the CCD camera number.
The first output file is the reconstructed attitude file, while the second one is the list of

bad pixels, one file for each reduced CCD.
The latter file is the most important and contains the calibrated and concatenated event list, the files we need to produce scientific products such as spectra, images or time series. We rename for simplicity such files as `image_raw_cam.fits`, with `cam` to be replaced with either `pn`, `m1` or `m2`, depending on which camera they refer to.

A.2 Filtering for flaring events

Other than photons, XMM-Newton can also focus charged particles on the detection plane. Before the launch of the instrument, the capability of X-ray telescopes to focus electrons was already known, therefore they were equipped with magnetic diverters in order to deflect such electrons outside of the detection plane. In addition, the first observations of XMM-Newton revealed that the instrument is also able to focus soft protons, with $E \lesssim 300$ keV. These protons, of likely solar origin (e.g., Carter & Read, 2007), lose energy for each interaction with the mirrors, and are able to contaminate the higher energies ($E \gtrsim 10$ keV) of the detected spectrum, since they are almost undistinguishable from the actual X-rays, making it impossible to reject them *a priori*.
While the EPIC instruments are well protected by the magnetic diverters when the satellite crosses the radiation belt, in which the soft protons are obviously more common, this effect is also observed above the radiation belt limit, where the instruments are fully operative. The effect is seen as a sudden increase, known as *soft proton flare* (SPF), of the background level, that can prevail over the regular background by several orders of magnitude (see Fig. A.1). Moreover, SPFs are unpredictable and can last from hundreds of seconds up to hours (De Luca & Molendi, 2004).
Since these background flares have a catastrophic effect on the detected X-ray spectrum of all three EPIC cameras aboard XMM-Newton, it is imperative to remove this events during the data reduction process.

First of all, we need to examine the countrate of such events, by selecting all those single-pixel events (i.e., `PATTERN==0`) in the energy range that is sensitive to soft proton flares. This is done by using the command

```
evselect table=image_raw_cam.fits withrateset=Y rateset=rate_cam.fits
maketimecolumn=Y timebinsize=100 makeratecolumn=Y
expression='Selection_Expression'
```

with `cam` being either `pn` or `m1`, `m2` and `Selection_Expression` given by

`#XMMEA_EP && (PI>10000&&PI<12000) && (PATTERN==0)` for EPIC-pn,

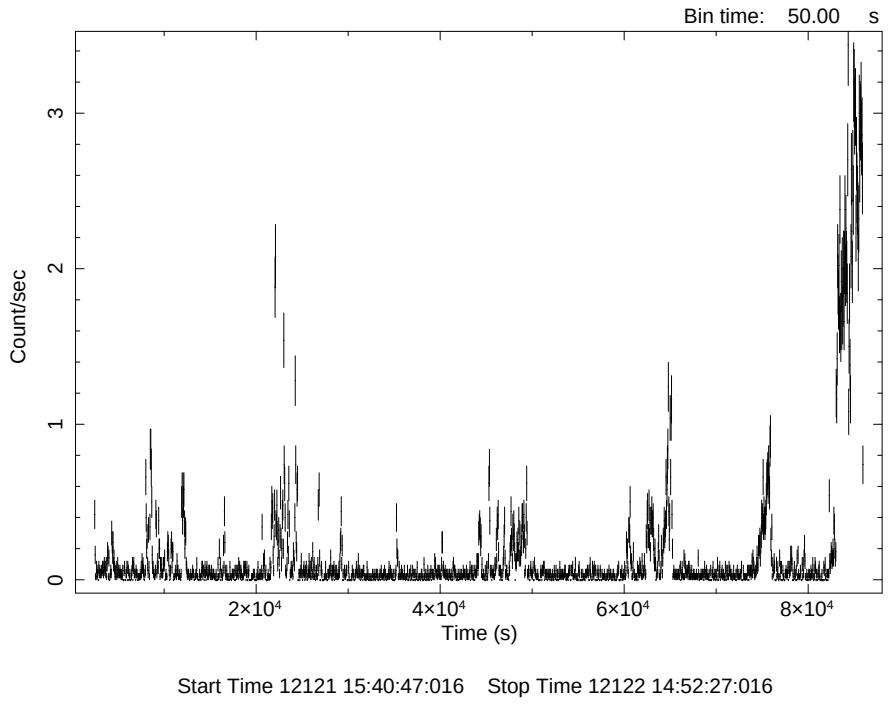

Figure A.1: Example of soft proton flaring in EPIC-pn data of `OBSID` 0029740101. The times of these flaring events must be removed by using the SAS command `evselect`, otherwise the spectrum might be affected by high background.

`#XMMEA_EM && (PI>10000) && (PATTERN==0)` for EPIC-MOS

Suppose we are working on EPIC-pn data, we can generate a lightcurve as Fig. A.1 by running the command

```
lcurve nser=1 cfile1=rate_pn.fits window="-" dtnb=50 nbint=3000 outfile="lc"
plot=yes plotdev="/xs".
```

The SPFs are then removed from the data with a manual inspection of the lightcurve. In the example of Fig. A.1, we should get rid of all data in the time bins where the countrate exceeds ~ 0.2 counts/s, since the average countrate is all contained within that value. The selection is done by running the command

```
tabgtigen table=rate_pn.fits:RATE expression='RATE<0.2'
gtiset=gtisel_pn.fits timecolumn=TIME,
```

that creates a Good Time Interval (GTI) event list for non flaring events. A filtered event list is then created with the command

```
evselect table=image_raw_pn.ds:EVENTS expression='Selection_Expression
&&GTI(gtisel_pn.fits,TIME)' withfilteredset=yes
filteredset=filtered_image_raw_pn.fits
filtertype=expression updateexposure=yes filterexposure=yes
keepfilteroutput=yes,
```

with `Selection_Expression` given by

`#XMMEA_EP &&(PATTERN<=4.0)&&(PI in [200:12000])` for EPIC-pn,
`#XMMEA_EM &&(PATTERN<=12.0)&&(PI in [200:12000]` for EPIC-MOS

This procedure selects events with countrate less than the selected one, in the whole energy band of the instrument ($200 - 12000$ eV), with the appropriate selection of event type for each camera with the `PATTERN` command.

A.3 Image generation and pile-up correction

Once the event list is appropriately cleaned of soft proton flaring events, an image of the X-ray observation can be created by running the code

```
evselect table=filtered_image_raw_cam.fits withimageset=yes
imageset=image_cam.fits xcolumn=X ycolumn=Y imagebinning=imageSize
ximagesize=1000 yimagesize=1000
```

with, again, `cam` to be replaced with either `pn`, `m1` or `m2`, depending on which camera we are analyzing. This image, `image_cam.fits`, can be read by several software, such as `ds9`, see Fig. A.2.
Before extracting any spectra, we should check for the presence of pile-up (Ballet, 1999) in the observation. In X-ray CCD detectors, such as the three EPIC cameras, one assumes that an event, i.e. a local excess of charge, is due to an impact of a single X-ray photon on the detector. If an event is due to more than one event, we have a superposition of X-ray photons, known as pile-up. During a single read-out of the CCD, in fact, two photons might hit two adjacent pixels, and the electronics is not able to distinguish if the two pixels are both hit by the same photon or by two or more, and are erroneously combined in an event of wrong pattern type (*pattern pile-up*). Also, during a single read-out, more than a photon might hit the same pixel, therefore the event is erroneously read as a single photon with energy equal to the sum of the energies of the photons actually hitting the CCD, moving the count to harder parts of the spectrum (*energy pile-up*). Pile-up therefore significantly alters the measurement of both countrate and energy, and needs to be corrected.

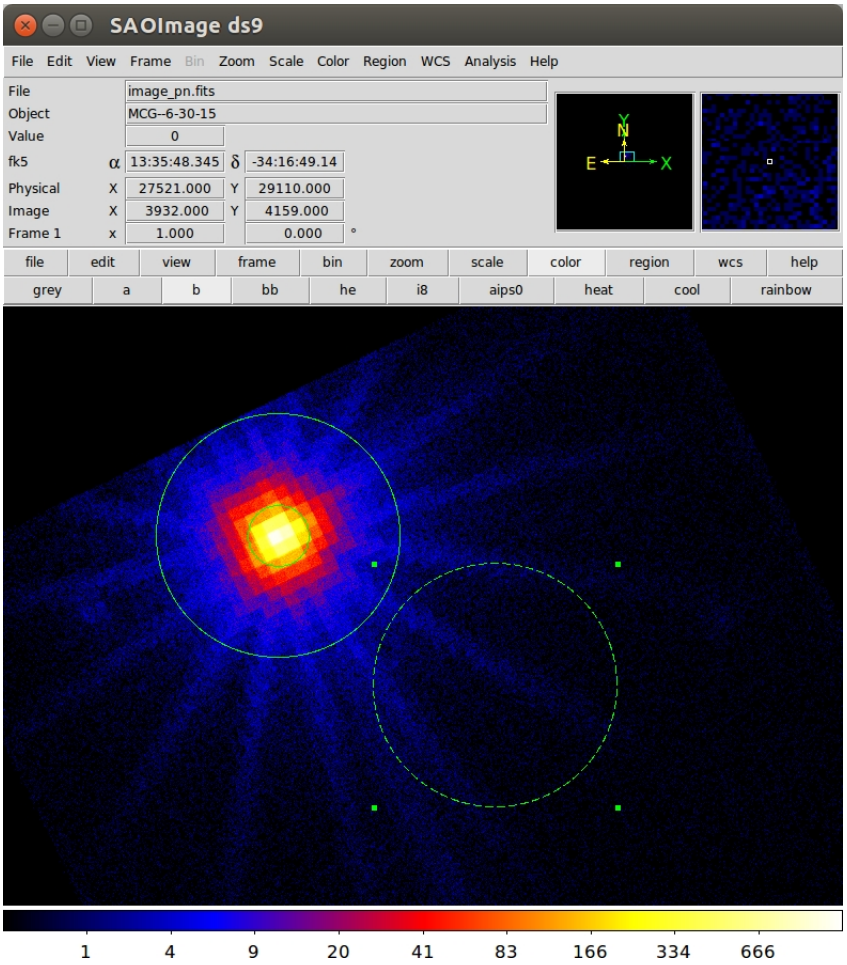

Figure A.2: DS9 screenshot of the EPIC-pn image generated for `OBSID` 0029740101. In this case, the source spectrum is extracted by selecting an annulus, centered on the source, of internal radius 10" and external radius of 40", to avoid pile-up. A second zone, the dashed circle of radius 40" is selected to sample the background of the observation.

The majority of the energy is contained in the core of the so-called *Point Spread Function* (PSF), which is the spatial response of the detector to a point-like source. The PSF is usually made up by a central gaussian peak, called "first diffraction angle", and some other higher order diffraction angles. Since the majority of the signal is located in the central peak, the first diffraction angle has the biggest probability of hosting pile-up events. The other diffraction angles, on the contrary, have lower probability of hosting more than one event during a single read-out of the CCD camera.

The correction therefore might be done by removing the data from the first diffraction angle. As we shall see in the next section, the spectrum is extracted from the image by selecting a circle around the source (see Fig. A.2). If we want to exclude piled-up data, we can select an annulus with internal radius equal to the first diffraction angle, that depends

on the observation.
Therefore we need to assess if we need this correction or not, and this might be done by extracting a filtered event list, including only photons within the source region, without any filtering in pattern. Provided that our `gti` file is `gtisel_cam.fits`, the original event list is `image_raw_cam.ds`, and that the source is contained within a circle of radius 800 in physical units, that corresponds to 40", centered in sky coordinates (26191.086, 27996.994), this selection is done by typing

```
evselect table=image_raw_cam.ds withfilteredset=yes
filteredset=cam_filtered.evt keepfilteroutput=yes
expression="((X,Y) in circle(26191.086,27996.994,800))
&& gti(gtisel_cam.fits,TIME)".
```

Once the selection is done, we run the command `epatplot` on the filtered output event list, `cam_filtered.evt`, to display the observed and the expected pattern distribution in a plot such as Fig. A.3.

```
epatplot set=pn_filtered.evt plotfile="pn_filtered_pat.ps"
```

Such plots also include the observed-to-model fraction of single and double-pixel events in the $0.5 - 2$ keV band. In a pile-up-free scenario, those two fractional values would be compatible with unity, but if the observation is piled-up in both pattern and energy, the distribution of pattern will deviate, as in the case of the top plot of Fig. A.3.
If the source is piled-up, we shall repeat the procedure by trying to exclude the first diffraction angle of the PSF, for example taking an annulus of internal radius 10" (200 in physical coordinates) and external radius 40" (800 in physical coordinates), instead of a circle, excluding in fact all data within the internal radius. Therefore we type

```
evselect table=image_raw_cam.ds withfilteredset=yes
filteredset=cam_filtered.evt keepfilteroutput=yes
expression="((X,Y) in annulus(26191.086,27996.994,200,800))
&& gti(gtisel_cam.fits,TIME)"
epatplot set=pn_filtered.evt plotfile="pn_filtered_pat.ps"
```

If the new observed-to-model fraction is now compatible with unity, such as the bottom plot of Fig. A.3, we stop and use such coordinates to extract the spectrum (see next section), otherwise we repeat with greater internal radii. In this thesis we considered acceptable an observed-to-model fraction compatible with unity within a 95% confidence level.

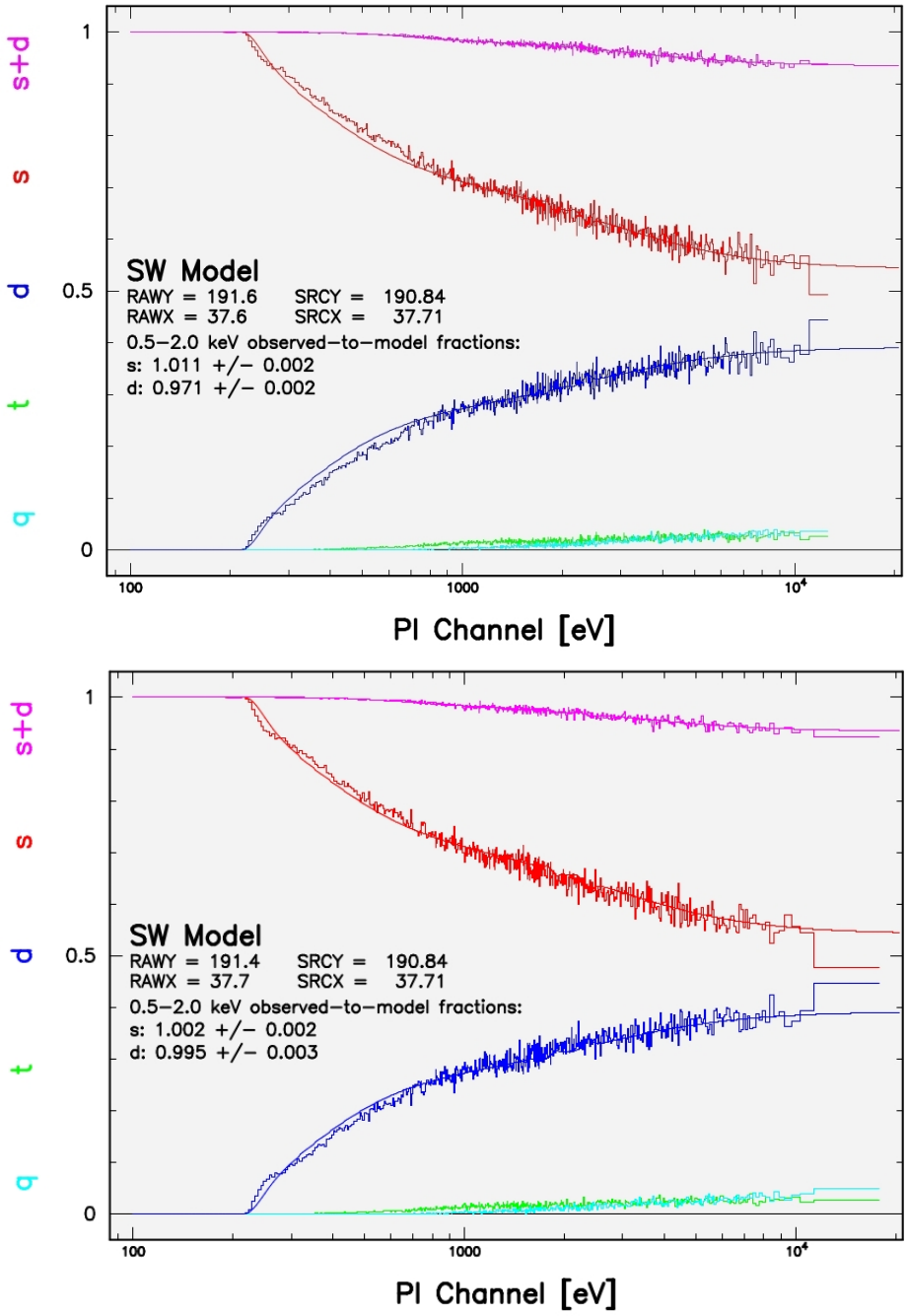

Figure A.3: *Top.* Comparison between the observed and expected pattern distribution in the $0.5 - 2$ keV band, for a piled-up observation with no correction. The ratio is not compatible with unity for neither single or double pixel distribution. *Bottom.* Same comparison, after correcting for pile-up by only selecting data on the higher order diffraction angles, by taking an annulus with internal radius equal to 10" and external radius equal to 40" (see Fig. A.2). The ratio is now compatible with unity within 95% confidence interval. The color legend is also shown: "q" stands for quadruple pixel events distribution, "t" for triple, "d" for double and "s" for single. The sum of the double and single pixel pixel events ("s+d") is also shown.

A.4 Spectrum extraction

Once we have selected the appropriate area in which the source data is likely located and pile-up-free, for example an annulus, centered on the centre of the source (see Fig. A.2) of internal radius 10" (200 in physical coordinates) and external radius 40" (800 in physical coordinates), we are able to extract a spectrum from the image, by using again the command `evselect`. The on-axis Encircled Energy Fraction (EEF), i.e. the percentage of photons that lie in a circle of given radius, is 85% at the chosen radius of 40".
For EPIC-pn, the spectrum selection is done by typing

```
evselect table=filtered_image_raw_pn.fits withspectrumset=yes
spectrumset=spectrum_pn.fits energycolumn=PI spectralbinsize=5
withspecranges=yes specchannelmin=0 specchannelmax=20479
expression='(FLAG==0) && (PATTERN<=4) && ((X,Y) IN
annulus(26191.086,27996.994,200,800))'
```

while for EPIC-MOS cameras, the command is slightly different

```
evselect table=filtered_image_raw_m1.fits withspectrumset=yes
spectrumset=spectrum_m1.fits energycolumn=PI spectralbinsize=5
withspecranges=yes specchannelmin=0 specchannelmax=11999
expression='#XMMEA_EM && (PATTERN<=12) && ((X,Y) IN
annulus(26191.086,27996.994,200,800))'
```

In addition to the spectrum, it is also necessary to sample the background of the observations in the proximity of the source, let's say in a circle of 40" radius centered in $(27749.907, 27491.695)$, see the dashed circle in Fig. A.2. Given that we choose the background very close to the source, we assume the on-axis EEF. The procedure is the same, we only need to change the names of the files and the coordinates of the region we are selecting. For EPIC-pn we have

```
evselect table=filtered_image_raw_pn.fits withspectrumset=yes
spectrumset=bkgrd_pn.fits energycolumn=PI spectralbinsize=5
withspecranges=yes specchannelmin=0 specchannelmax=20479
expression='(FLAG==0) && (PATTERN<=4) && ((X,Y) IN
circle(27749.907,27491.695,800))'
```

while for EPIC-MOS cameras we have

```
evselect table=filtered_image_raw_m1.fits withspectrumset=yes
spectrumset=bkgrd_m1.fits energycolumn=PI spectralbinsize=5
withspecranges=yes specchannelmin=0 specchannelmax=11999
```

```
expression='#XMMEA_EM && (PATTERN<=12) && ((X,Y) IN
circle(27749.907,27491.695,800))'.
```

At this point we need to generate the Redistribution Matrix File (RMF). The convolution from energy space into detector space involves a spreading of the observed counts by the detector resolution, which is expressed by a matrix multiplication. While for gratings instruments, such as the two RGS cameras of XMM-Newton, this matrix is almost diagonal, it's not the case of CCD cameras, such as the three EPIC cameras. Therefore we must generate a RMF by using the command

```
rmfgen format=var rmfset=cam.rmf spectrumset=spectrum_cam.fits
threshold=1.0e-6
```

for every camera `cam`=`pn`, `m1`, `m2`.

Another fundamental tool to analyze the spectrum of a source is the Auxiliary Response File (ARF), that contains information about the "effective area" of the instrument, which includes the geometric areas of telescope, filter and detector, and about the quantum efficiency (QE) as a function of energy averaged over time. While the effective area is measured in cm^2, and the QE is measured in counts/photons, these two quantities are multiplied to create the ARF, which is then measured in cm^2·counts/photon. The ARF is generated with the command

```
arfgen arfset=cam.arf spectrumset=spectrum_cam.fits withrmfset=yes
rmfset=cam.rmf extendedsource=no modelee=yes withbadpixcorr=yes
badpixlocation=filtered_cam.fits modelootcorr=yes
```

When the input spectrum, in our case `spectrum_cam.fits` is multiplied by the ARF, the result will be the distribution of counts as would be seen by a detector with ideal resolution in energy. Then, the RMF is needed, in order to produce the final spectrum.
All these files can be compressed into a single file, easily readable by spectrum analysis program `XSPEC` (Arnaud, 1996), using the SAS tool `specgroup`, by which we can specify the number of photons for each bin with the `mincounts` option. If the number of counts is very high, we take the risk to oversample the instrument resolution, which is to be avoided, since we cannot have bins that are closer in energy than the energy resolution of the instrument. A minimum energy width of each bin can be forced by introducing the parameter `oversample`. If we want our spectrum to have bins composed of 60 counts and ensure that no group is narrower than 1/5 of the full width half maximum (FWHM) resolution at the central photon energy of the bin, we need to type

```
specgroup spectrumset=spectrum_cam.fits
groupedset=spectrum_cam_bin60_oversample5.pi mincounts=60 oversample=5
```

```
rmfset=cam.rmf arfset=cam.arf backgndset=bkgrd_cam.fits
```

The output `spectrum_cam_bin60_oversample5.pi` file takes into account the ARF, the RMF and the background file, and it is readable by spectral analysis program `XSPEC`.

Bibliography

Abazajian K. N., et al., 2009, ApJS, 182, 543

Abramowicz M. A., Bao G., Lanza A., Zhang X.-H., 1991, A&A, 245, 454

Abrassart A., Czerny B., 2000, A&A, 356, 475

Alam S., et al., 2015, ApJS, 219, 12

Allevato V., Paolillo M., Papadakis I., Pinto C., 2013, ApJ, 771, 9

Almaini O., et al., 2000, MNRAS, 315, 325

Andrae R., Kim D.-W., Bailer-Jones C. A. L., 2013, A&A, 554, A137

Antonucci R., 1993, ARA&A, 31, 473

Arévalo P., Papadakis I., Kuhlbrodt B., Brinkmann W., 2005, A&A, 430, 435

Arnaud K. A., 1996, in Jacoby G. H., Barnes J., eds, Astronomical Society of the Pacific Conference Series Vol. 101, Astronomical Data Analysis Software and Systems V. p. 17

Aschenbach B., Citterio O., Ellwood J. M., Jensen P., de Korte P., Peacock A., Willingale R., Burke W. R., eds, 1986, The high-throughput X-ray Spectroscopy Mission. Report of the Telescope Working Group. ESA Special Publication Vol. 1084

Ashton C. E., Page M. J., Blustin A. J., Puchnarewicz E. M., Branduardi-Raymont G., Mason K. O., Córdova F. A., Priedhorsky W. C., 2004, MNRAS, 355, 73

Asplund M., Grevesse N., Sauval A. J., Scott P., 2009, ARA&A, 47, 481

Ballet J., 1999, A&AS, 135, 371

Barr P., Mushotzky R. F., 1986, Nature, 320, 421

Barvainis R., Lehár J., Birkinshaw M., Falcke H., Blundell K. M., 2005, ApJ, 618, 108

Becker R. H., White R. L., Helfand D. J., 1995, ApJ, 450, 559

Becker R. H., White R. L., Gregg M. D., Brotherton M. S., Laurent-Muehleisen S. A., Arav N., 2000, ApJ, 538, 72

Begelman M. C., de Kool M., 1991, in Bertout C., Collin-Souffrin S., Lasota J. P., eds, IAU Colloq. 129: The 6th Institute d'Astrophysique de Paris (IAP) Meeting: Structure and Emission Properties of Accretion Disks. p. 143

Bennert N., Falcke H., Schulz H., Wilson A. S., Wills B. J., 2002, ApJ, 574, L105

Bennett A. S., 1962, MmRAS, 68, 163

Bentz M. C., Katz S., 2015, PASP, 127, 67

Bentz M. C., Peterson B. M., Netzer H., Pogge R. W., Vestergaard M., 2009, ApJ, 697, 160

Bevington P. R., 1969, Data reduction and error analysis for the physical sciences. McGraw-Hill.

Blustin A. J., Page M. J., Fuerst S. V., Branduardi-Raymont G., Ashton C. E., 2005, A&A, 431, 111

Boller T., Brandt W. N., Fink H., 1996, A&A, 305, 53

Boroson T. A., 2011, in Narrow-Line Seyfert 1 Galaxies and their Place in the Universe. p. 3

Botte V., Ciroi S., Rafanelli P., Di Mille F., 2004, AJ, 127, 3168

Brandt W. N., Laor A., Wills B. J., 2000, ApJ, 528, 637

Brenneman L. W., Reynolds C. S., 2006, ApJ, 652, 1028

Burm H., 1986, A&A, 165, 120

Burtscher L., et al., 2013, A&A, 558, A149

Butler R. C., Scarsi L., 1991, Advances in Space Research, 11, 265

Cappi M., et al., 2009, A&A, 504, 401

Carter J. A., Read A. M., 2007, A&A, 464, 1155

Cattaneo A., et al., 2009, Nature, 460, 213

Chartas G., Brandt W. N., Gallagher S. C., Garmire G. P., 2002, ApJ, 579, 169

Chen X., Taam R. E., 1995, ApJ, 441, 354

Chevallier L., Collin S., Dumont A.-M., Czerny B., Mouchet M., Gonçalves A. C., Goosmann R., 2006, A&A, 449, 493

Clausen K., Winkler C., 1994, ESA Bulletin, 79, 6

Collier S., Peterson B. M., 2001, ApJ, 555, 775

Collin-Souffrin S., 1991, A&A, 249, 344

Collin-Souffrin S., Joly M., Pequignot D., Dumont S., 1986, A&A, 166, 27

Connolly S. D., McHardy I. M., Skipper C. J., Emmanoulopoulos D., 2016, MNRAS, 459, 3963

Coppi P. S., 1999, in Poutanen J., Svensson R., eds, Astronomical Society of the Pacific Conference Series Vol. 161, High Energy Processes in Accreting Black Holes. p. 375 (arXiv:astro-ph/9903158)

Corral A., Georgantopoulos I., Watson M. G., Rosen S. R., Page K. L., Webb N. A., 2015, A&A, 576, A61

Crenshaw D. M., Kraemer S. B., 2012, ApJ, 753, 75

Czerny B., Elvis M., 1987, ApJ, 321, 305

Czerny B., Nikołajuk M., Różańska A., Dumont A.-M., Loska Z., Zycki P. T., 2003, A&A, 412, 317

Czerny B., Różańska A., Dovčiak M., Karas V., Dumont A.-M., 2004, A&A, 420, 1

Davidson K., Netzer H., 1979, Reviews of Modern Physics, 51, 715

Dawson K. S., et al., 2013, AJ, 145, 10

De Luca A., Molendi S., 2004, A&A, 419, 837

Den Herder J. W., et al., 2001, A&A, 365, L7

Denney K. D., et al., 2010, ApJ, 721, 715

Dewangan G. C., Griffiths R. E., Di Matteo T., Schurch N. J., 2004, ApJ, 607, 788

Di Clemente A., Giallongo E., Natali G., Trevese D., Vagnetti F., 1996, ApJ, 463, 466

Dietrich M., et al., 1993, ApJ, 408, 416

Edge D. O., Shakeshaft J. R., McAdam W. B., Baldwin J. E., Archer S., 1959, MmRAS, 68, 37

Eisenstein D. J., et al., 2011, AJ, 142, 72

Elitzur M., Shlosman I., 2006, ApJ, 648, L101

Elvis M., 2000, ApJ, 545, 63

Emmanoulopoulos D., Papadakis I. E., McHardy I. M., Arévalo P., Calvelo D. E., Uttley P., 2012, MNRAS, 424, 1327

Emmering R. T., Blandford R. D., Shlosman I., 1992, ApJ, 385, 460

Esin A. A., McClintock J. E., Narayan R., 1997, ApJ, 489, 865

Fabian A. C., 2012, ARA&A, 50, 455

Fabian A. C., Iwasawa K., Reynolds C. S., Young A. J., 2000, PASP, 112, 1145

Fabian A. C., Lohfink A., Kara E., Parker M. L., Vasudevan R., Reynolds C. S., 2015, MNRAS, 451, 4375

Farrah D., Lacy M., Priddey R., Borys C., Afonso J., 2007, ApJ, 662, L59

Farrah D., et al., 2012, ApJ, 745, 178

Fath E. A., 1909, Lick Observatory Bulletin, 5, 71

Ferrarese L., Merritt D., 2000, ApJ, 539, L9

Filiz Ak N., et al., 2012, ApJ, 757, 114

Frank J., King A. R., Raine D. J., 1985, Accretion power in astrophysics. Cambridge University Press.

Fukugita M., Ichikawa T., Gunn J. E., Doi M., Shimasaku K., Schneider D. P., 1996, AJ, 111, 1748

Fukumura K., Tombesi F., Kazanas D., Shrader C., Behar E., Contopoulos I., 2015, ApJ, 805, 17

Fukumura K., Kazanas D., Shrader C., Behar E., Tombesi F., Contopoulos I., 2017, Nature Astronomy, 1, 0062

Gandhi P., 2005, Asian Journal of Physics, 13, 90

García J., Dauser T., Reynolds C. S., Kallman T. R., McClintock J. E., Wilms J., Eikmann W., 2013, ApJ, 768, 146

Gaskell C. M., 2009, New A Rev., 53, 140

Gebhardt K., et al., 2000, ApJ, 539, L13

Gehrels N., et al., 2004, ApJ, 611, 1005

Georgakakis A., et al., 2017, MNRAS, 469, 3232

George I. M., Fabian A. C., 1991, MNRAS, 249, 352

George I. M., Nandra K., Laor A., Turner T. J., Fiore F., Netzer H., Mushotzky R. F., 1997, ApJ, 491, 508

Giallongo E., Trevese D., Vagnetti F., 1991, ApJ, 377, 345

Gibson R. R., Brandt W. N., 2012, ApJ, 746, 54

Gibson R. R., Brandt W. N., Schneider D. P., 2008, ApJ, 685, 773

Gibson R. R., et al., 2009, ApJ, 692, 758

Gierliński M., Done C., 2004, MNRAS, 349, L7

Gilli R., Comastri A., Hasinger G., 2007, A&A, 463, 79

Giustini M., et al., 2011, A&A, 536, A49

Giveon U., Maoz D., Kaspi S., Netzer H., Smith P. S., 1999, MNRAS, 306, 637

Gofford J., et al., 2011, MNRAS, 414, 3307

Gofford J., Reeves J. N., Tombesi F., Braito V., Turner T. J., Miller L., Cappi M., 2013, MNRAS, 430, 60

Graham M. J., et al., 2015a, MNRAS, 453, 1562

Graham M. J., et al., 2015b, Nature, 518, 74

Green A. R., McHardy I. M., Lehto H. J., 1993, MNRAS, 265, 664

Greenstein J. L., Schmidt M., 1964, ApJ, 140, 1

Guainazzi M., Bianchi S., 2007, MNRAS, 374, 1290

Guilbert P. W., Rees M. J., 1988, MNRAS, 233, 475

Gupta A., Mathur S., Krongold Y., Nicastro F., 2013, ApJ, 772, 66

Gupta A., Mathur S., Krongold Y., 2015, ApJ, 798, 4

Haardt F., Maraschi L., 1991, ApJ, 380, L51

Haardt F., Maraschi L., 1993, ApJ, 413, 507

Haardt F., Maraschi L., Ghisellini G., 1997, ApJ, 476, 620

Hainline K. N., Hickox R. C., Greene J. E., Myers A. D., Zakamska N. L., Liu G., Liu X., 2014, ApJ, 787, 65

Halpern J. P., 1984, ApJ, 281, 90

Häring N., Rix H.-W., 2004, ApJ, 604, L89

Harrison C. M., 2016, Observational Constraints on the Influence of Active Galactic Nuclei on the Evolution of Galaxies. Springer Theses, Springer International Publishing., doi:10.1007/978-3-319-28454-5

Harrison F. A., et al., 2013, ApJ, 770, 103

Hawkins M. R. S., 2004, A&A, 424, 519

Hewett P. C., Wild V., 2010, MNRAS, 405, 2302

Ho L. C., 2008, ARA&A, 46, 475

Isobe T., Feigelson E. D., Akritas M. G., Babu G. J., 1990, ApJ, 364, 104

Jaffe W., et al., 2004, Nature, 429, 47

Jansen F., et al., 2001, A&A, 365, L1

Jiang L., Fan X., Ivezić Ž., Richards G. T., Schneider D. P., Strauss M. A., Kelly B. C., 2007, ApJ, 656, 680

Kaastra J. S., Mewe R., Liedahl D. A., Komossa S., Brinkman A. C., 2000, A&A, 354, L83

Kaastra J. S., et al., 2014, Science, 345, 64

Kalberla P. M. W., Burton W. B., Hartmann D., Arnal E. M., Bajaja E., Morras R., Pöppel W. G. L., 2005, A&A, 440, 775

Kallman T., Bautista M., 2001, ApJS, 133, 221

Kara E., García J. A., Lohfink A., Fabian A. C., Reynolds C. S., Tombesi F., Wilkins D. R., 2017, MNRAS, 468, 3489

Kaspi S., Netzer H., 1999, ApJ, 524, 71

Kaspi S., Smith P. S., Netzer H., Maoz D., Jannuzi B. T., Giveon U., 2000, ApJ, 533, 631

Kaspi S., et al., 2002, ApJ, 574, 643

Katz J. I., 1976, ApJ, 206, 910

Kawaguchi T., Shimura T., Mineshige S., 2001, ApJ, 546, 966

Kellermann K. I., Sramek R., Schmidt M., Shaffer D. B., Green R., 1989, AJ, 98, 1195

Kelly B. C., Bechtold J., Siemiginowska A., 2009, ApJ, 698, 895

King A., Pounds K., 2015, ARA&A, 53, 115

Komossa S., 2008, in Revista Mexicana de Astronomia y Astrofisica Conference Series. pp 86–92 (arXiv:0710.3326)

Königl A., Kartje J. F., 1994, ApJ, 434, 446

Kozłowski S., 2016, ApJ, 826, 118

Kozłowski S., 2017a, ApJS, 228, 9

Kozłowski S., 2017b, ApJ, 835, 250

Kozłowski S., Kochanek C. S., Ashby M. L. N., Assef R. J., Brodwin M., Eisenhardt P. R., Jannuzi B. T., Stern D., 2016, ApJ, 817, 119

Krauss F., 2016, Extreme Environments: From supermassive black holes to supernovae, PhD Thesis

Krolik J. H., Begelman M. C., 1988, ApJ, 329, 702

Krolik J. H., Kriss G. A., 2001, ApJ, 561, 684

Laha S., Guainazzi M., Dewangan G. C., Chakravorty S., Kembhavi A. K., 2014, MNRAS, 441, 2613

Lawrence A., Papadakis I., 1993, ApJ, 414, L85

Lehto H. J., 1989, in Hunt J., Battrick B., eds, ESA Special Publication Vol. 296, Two Topics in X-Ray Astronomy, Volume 1: X Ray Binaries. Volume 2: AGN and the X Ray Background.

Liang E. P. T., 1979, ApJ, 231, L111

Lightman A. P., White T. R., 1988, ApJ, 335, 57

Lin D., Webb N. A., Barret D., 2012, ApJ, 756, 27

Liu G., Zakamska N. L., Greene J. E., Nesvadba N. P. H., Liu X., 2013, MNRAS, 436, 2576

Lohfink A. M., et al., 2016, ApJ, 821, 11

Longinotti A. L., Krongold Y., Guainazzi M., Giroletti M., Panessa F., Costantini E., Santos-Lleo M., Rodriguez-Pascual P., 2015, ApJ, 813, L39

Lusso E., Risaliti G., 2016, ApJ, 819, 154

MacLeod C. L., et al., 2010, ApJ, 721, 1014

MacLeod C. L., et al., 2012, ApJ, 753, 106

Madau P., 1988, ApJ, 327, 116

Magdziarz P., Zdziarski A. A., 1995, MNRAS, 273, 837

Magdziarz P., Blaes O. M., Zdziarski A. A., Johnson W. N., Smith D. A., 1998, MNRAS, 301, 179

Manners J., Almaini O., Lawrence A., 2002, MNRAS, 330, 390

Marinucci A., et al., 2014, ApJ, 787, 83

Markowitz A., Edelson R., 2004, ApJ, 617, 939

Mason K. O., et al., 2001, A&A, 365, L36

Mason K. O., et al., 2002, ApJ, 580, L117

Mateos S., Saxton R. D., Read A. M., Sembay S., 2009, A&A, 496, 879

Mathur S., Wilkes B., Elvis M., 1998, ApJ, 503, L23

Matt G., 2002, in Maiolino R., Marconi A., Nagar N., eds, Astronomical Society of the Pacific Conference Series Vol. 258, Issues in Unification of Active Galactic Nuclei. p. 3 (arXiv:astro-ph/0107584)

Matt G., Perola G. C., Piro L., 1991, A&A, 247, 25

Matt G., Fabian A. C., Reynolds C. S., 1997, MNRAS, 289, 175

Matt G., et al., 2015, MNRAS, 447, 3029

McHardy I. M., 2001, in Peterson B. M., Pogge R. W., Polidan R. S., eds, Astronomical Society of the Pacific Conference Series Vol. 224, Probing the Physics of Active Galactic Nuclei. p. 205

McHardy I. M., Papadakis I. E., Uttley P., 1999, Nuclear Physics B Proceedings Supplements, 69, 509

McHardy I. M., Gunn K. F., Uttley P., Goad M. R., 2005, MNRAS, 359, 1469

McKernan B., Yaqoob T., Reynolds C. S., 2007, MNRAS, 379, 1359

Merloni A., et al., 2012, preprint, (arXiv:1209.3114)

Merritt D., 2013, Dynamics and Evolution of Galactic Nuclei. Princeton University Press.

Middei R., Vagnetti F., Bianchi S., La Franca F., Paolillo M., Ursini F., 2017, A&A, 599, A82

Miller L., Turner T. J., Reeves J. N., George I. M., Kraemer S. B., Wingert B., 2007, A&A, 463, 131

Miller L., Turner T. J., Reeves J. N., 2008, A&A, 483, 437

Miniutti G., Fabian A. C., 2004, MNRAS, 349, 1435

Miniutti G., et al., 2007, PASJ, 59, 315

Murray N., Chiang J., 1997, ApJ, 474, 91

Mushotzky R. F., Done C., Pounds K. A., 1993, ARA&A, 31, 717

Mushotzky R. F., Edelson R., Baumgartner W., Gandhi P., 2011, ApJ, 743, L12

Nandra K., Pounds K. A., 1994, MNRAS, 268, 405

Nandra K., George I. M., Mushotzky R. F., Turner T. J., Yaqoob T., 1997, ApJ, 476, 70

Nandra K., et al., 2013, preprint, (arXiv:1306.2307)

Nardini E., et al., 2015, Science, 347, 860

Nemmen R. S., Tchekhovskoy A., 2015, MNRAS, 449, 316

Netzer H., 2013, The Physics and Evolution of Active Galactic Nuclei. Cambridge University Press.

Oke J. B., 1963, Nature, 197, 1040

Onken C. A., Ferrarese L., Merritt D., Peterson B. M., Pogge R. W., Vestergaard M., Wandel A., 2004, ApJ, 615, 645

Osterbrock D. E., 1981, ApJ, 249, 462

Osterbrock D. E., Ferland G. J., 2006, Astrophysics of gaseous nebulae and active galactic nuclei. University Science Books.

Osterbrock D. E., Pogge R. W., 1985, ApJ, 297, 166

Padovani P., et al., 2017, A&A Rev., 25, 2

Pancoast A., Brewer B. J., Treu T., Park D., Barth A. J., Bentz M. C., Woo J.-H., 2014, MNRAS, 445, 3073

Panessa F., et al., 2016, MNRAS, 461, 3153

Paolillo M., Schreier E. J., Giacconi R., Koekemoer A. M., Grogin N. A., 2004, ApJ, 611, 93

Papadakis I. E., 2004, MNRAS, 348, 207

Papadakis I. E., Brinkmann W., Page M. J., McHardy I., Uttley P., 2007, A&A, 461, 931

Pâris I., et al., 2017, A&A, 597, A79

Peterson B. M., 1993, PASP, 105, 247

Peterson B. M., 1997, An Introduction to Active Galactic Nuclei. Cambridge University Press.

Peterson B. M., Wandel A., 1999, ApJ, 521, L95

Peterson B. M., et al., 2004, ApJ, 613, 682

Petrucci P. O., et al., 2000, ApJ, 540, 131

Petrucci P. O., Merloni A., Fabian A., Haardt F., Gallo E., 2001, MNRAS, 328, 501

Piconcelli E., Jimenez-Bailón E., Guainazzi M., Schartel N., Rodríguez-Pascual P. M., Santos-Lleó M., 2005, A&A, 432, 15

Pier E. A., Krolik J. H., 1992, ApJ, 399, L23

Pier E. A., Krolik J. H., 1993, ApJ, 418, 673

Ponti G., Miniutti G., Cappi M., Maraschi L., Fabian A. C., Iwasawa K., 2006, MNRAS, 368, 903

Ponti G., Papadakis I., Bianchi S., Guainazzi M., Matt G., Uttley P., Bonilla N. F., 2012, A&A, 542, A83

Pounds K., 2014a, Space Sci. Rev., 183, 339

Pounds K. A., 2014b, MNRAS, 437, 3221

Pounds K. A., Vaughan S., 2011a, MNRAS, 413, 1251

Pounds K. A., Vaughan S., 2011b, MNRAS, 415, 2379

Pounds K. A., Vaughan S., 2012, MNRAS, 423, 165

Pounds K. A., Reeves J. N., King A. R., Page K. L., O'Brien P. T., Turner M. J. L., 2003a, MNRAS, 345, 705

Pounds K. A., King A. R., Page K. L., O'Brien P. T., 2003b, MNRAS, 346, 1025

Pozdniakov L. A., Sobol I. M., Siuniaev R. A., 1976, Soviet Astronomy Letters, 2, 55

Pradhan A. K., Nahar S. N., 2015, Atomic Astrophysics and Spectroscopy. Cambridge University Press.

Predehl P., et al., 2010, in Space Telescopes and Instrumentation 2010: Ultraviolet to Gamma Ray. p. 77320U (arXiv:1001.2502), doi:10.1117/12.856577

Press W. H., Flannery B. P., Teukolsky S. A., 1986, Numerical recipes. The art of scientific computing. Cambridge University Press.

Reeves J. N., Porquet D., Braito V., Gofford J., Nardini E., Turner T. J., Crenshaw D. M., Kraemer S. B., 2013, ApJ, 776, 99

Reeves J. N., Braito V., Nardini E., Behar E., O'Brien P. T., Tombesi F., Turner T. J., Costa M. T., 2016, ApJ, 824, 20

Reynolds C. S., Di Matteo T., Fabian A. C., Hwang U., Canizares C. R., 1996, MNRAS, 283, L111

Reynolds C., et al., 2014, preprint, (arXiv:1412.1177)

Risaliti G., Elvis M., 2004, in Barger A. J., ed., Astrophysics and Space Science Library Vol. 308, Supermassive Black Holes in the Distant Universe. p. 187 (arXiv:astro-ph/0403618), doi:10.1007/978-1-4020-2471-9˙6

Risaliti G., Nardini E., Salvati M., Elvis M., Fabbiano G., Maiolino R., Pietrini P., Torricelli-Ciamponi G., 2011, MNRAS, 410, 1027

Romano P., Mathur S., Pogge R. W., Peterson B. M., Kuraszkiewicz J., 2002, ApJ, 578, 64

Rosen S. R., et al., 2016, A&A, 590, A1

Różańska A., Czerny B., Życki P. T., Pojmański G., 1999, MNRAS, 305, 481

Ryden B., 2016, Introduction to Cosmology. Cambridge University Press.

Schmidt M., 1963, Nature, 197, 1040

Schmidt M., et al., 1998, Astronomische Nachrichten, 319, 72

Schmitt H. R., Donley J. L., Antonucci R. R. J., Hutchings J. B., Kinney A. L., Pringle J. E., 2003, ApJ, 597, 768

Schneider D. P., et al., 2010, AJ, 139, 2360

Serafinelli R., Vagnetti F., Middei R., 2016, in Journal of Physics Conference Series. p. 012007 (arXiv:1601.05947), doi:10.1088/1742-6596/689/1/012007

Serafinelli R., Vagnetti F., Chiaraluce E., Middei R., 2017a, Frontiers in Astronomy and Space Sciences, 4, 21

Serafinelli R., Vagnetti F., Middei R., 2017b, A&A, 600, A101

Serafinelli R., Vagnetti F., Tombesi F., Tortosa A., 2018a, in preparation

Serafinelli R., Tombesi F., Vagnetti F., Piconcelli E., Saturni F. G., 2018b, in preparation

Seyfert C. K., 1943, ApJ, 97, 28

Shakura N. I., Sunyaev R. A., 1973, A&A, 24, 337

Shapiro S. L., Lightman A. P., Eardley D. M., 1976, ApJ, 204, 187

Shemmer O., et al., 2001, ApJ, 561, 162

Shemmer O., et al., 2014, ApJ, 783, 116

Shemmer O., Brandt W. N., Paolillo M., Kaspi S., Vignali C., Lira P., Schneider D. P., 2017, ApJ, 848, 46

Shen Y., et al., 2011, ApJS, 194, 45

Shields G. A., 1999, PASP, 111, 661

Shih D. C., Iwasawa K., Fabian A. C., 2002, MNRAS, 333, 687

Silk J., Rees M. J., 1998, A&A, 331, L1

Simonetti J. H., Cordes J. M., Spangler S. R., 1984, ApJ, 284, 126

Simonetti J. H., Cordes J. M., Heeschen D. S., 1985, ApJ, 296, 46

Sincell M. W., Krolik J. H., 1998, ApJ, 496, 737

Sobolewska M. A., Papadakis I. E., 2009, MNRAS, 399, 1597

Sobolewska M. A., Gierliński M., Siemiginowska A., 2009, MNRAS, 394, 1640

Soldi S., et al., 2014, A&A, 563, A57

Stoughton C., et al., 2002, AJ, 123, 485

Strüder L., et al., 2001, A&A, 365, L18

Sunyaev R. A., Titarchuk L. G., 1980, A&A, 86, 121

Swartz D. A., Ghosh K. K., McCollough M. L., Pannuti T. G., Tennant A. F., Wu K., 2003, ApJS, 144, 213

Takahashi T., et al., 2014, in Space Telescopes and Instrumentation 2014: Ultraviolet to Gamma Ray. p. 914425 (arXiv:1412.1356), doi:10.1117/12.2055681

Taylor R. D., Uttley P., McHardy I. M., 2003, MNRAS, 342, L31

Tombesi F., Cappi M., Reeves J. N., Palumbo G. G. C., Yaqoob T., Braito V., Dadina M., 2010a, A&A, 521, A57

Tombesi F., Sambruna R. M., Reeves J. N., Braito V., Ballo L., Gofford J., Cappi M., Mushotzky R. F., 2010b, ApJ, 719, 700

Tombesi F., Cappi M., Reeves J. N., Palumbo G. G. C., Braito V., Dadina M., 2011, ApJ, 742, 44

Tombesi F., Cappi M., Reeves J. N., Nemmen R. S., Braito V., Gaspari M., Reynolds C. S., 2013, MNRAS, 430, 1102

Tombesi F., Tazaki F., Mushotzky R. F., Ueda Y., Cappi M., Gofford J., Reeves J. N., Guainazzi M., 2014, MNRAS, 443, 2154

Tombesi F., Meléndez M., Veilleux S., Reeves J. N., González-Alfonso E., Reynolds C. S., 2015, Nature, 519, 436

Tortosa A., et al., 2017, MNRAS, 466, 4193

Trèvese D., Vagnetti F., 2002, ApJ, 564, 624

Turner T. J., Miller L., 2009, A&A Rev., 17, 47

Turner T. J., Pounds K. A., 1989, MNRAS, 240, 833

Turner T. J., George I. M., Nandra K., Turcan D., 1999, ApJ, 524, 667

Turner M. J. L., et al., 2001, A&A, 365, L27

Turner T. J., Miller L., Reeves J. N., Kraemer S. B., 2007, A&A, 475, 121

Turner T. J., Reeves J. N., Kraemer S. B., Miller L., 2008, A&A, 483, 161

Turnshek D. A., Grillmair C. J., Foltz C. B., Weymann R. J., 1988, ApJ, 325, 651

Urry C. M., Padovani P., 1995, PASP, 107, 803

Ursini F., et al., 2016, MNRAS, 463, 382

Uttley P., McHardy I. M., 2005, MNRAS, 363, 586

Uttley P., McHardy I. M., Papadakis I. E., 2002, MNRAS, 332, 231

Vagnetti F., Trevese D., Nesci R., 2003, ApJ, 590, 123

Vagnetti F., Turriziani S., Trevese D., Antonucci M., 2010, A&A, 519, A17

Vagnetti F., Turriziani S., Trevese D., 2011, A&A, 536, A84

Vagnetti F., Middei R., Antonucci M., Paolillo M., Serafinelli R., 2016, A&A, 593, A55

Vagnetti F., Serafinelli R., Chiaraluce E., Middei R., 2018, in preparation

Vanden Berk D. E., et al., 2001, AJ, 122, 549

Vanden Berk D. E., et al., 2004, ApJ, 601, 692

Vasudevan R. V., Fabian A. C., Gandhi P., Winter L. M., Mushotzky R. F., 2010, MNRAS, 402, 1081

Vaughan S., Fabian A. C., 2003, MNRAS, 341, 496

Vaughan S., Fabian A. C., 2004, MNRAS, 348, 1415

Vermeulen R. C., Cohen M. H., 1994, ApJ, 430, 467

Vignali C., Alexander D. M., Gilli R., Pozzi F., 2010, MNRAS, 404, 48

Vignali C., et al., 2015, A&A, 583, A141

Wagner A. Y., Umemura M., Bicknell G. V., 2013, ApJ, 763, L18

Watson M. G., et al., 2009, A&A, 493, 339

Webb W., Malkan M., 2000, ApJ, 540, 652

Weymann R. J., Foltz C. B., 1983, ApJ, 272, L1

Winkler H., 1997, MNRAS, 292, 273

Winter L. M., Veilleux S., McKernan B., Kallman T. R., 2012, ApJ, 745, 107

Woltjer L., 1959, ApJ, 130, 38

Woo J.-H., Urry C. M., 2002, ApJ, 579, 530

Worrall D. M., Tananbaum H., Giommi P., Zamorani G., 1987, ApJ, 313, 596

Xu Y.-D., 2011, ApJ, 739, 64

York D. G., et al., 2000, AJ, 120, 1579

Zdziarski A. A., Lubiński P., Gilfanov M., Revnivtsev M., 2003, MNRAS, 342, 355

Zheng X. C., et al., 2017, ApJ, 849, 127

Zu Y., Kochanek C. S., Kozłowski S., Udalski A., 2013, ApJ, 765, 106

Zubovas K., King A., 2012, ApJ, 745, L34

Acknowledgements

The writing of this dissertation, as well as the fulfilment of the Ph.D., would not have been possible without the help and advice of many people during these long and hard three years spent at University of Rome "Tor Vergata".
The first and foremost acknowledgement must go to my parents. They have always supported and encouraged their crazy kid with his even crazier dream, ever since he almost scared them to death when, aged 6, they found him reading an Astronomy encyclopedia in the middle of the night.
I am greatly thankful to my supervisor, Prof. Fausto Vagnetti, who had the patience to take in a student with very little knowledge of AGN physics and teach him how to become a researcher in the field. I am honored to have been one of his students.
The collaboration and teachings of Dr. Francesco Tombesi and Dr. Enrico Piconcelli were crucial for the developing of Chapter 5 and especially Chapter 6. I am deeply grateful to them for getting me interested in the topic of AGN winds and feedback, as well as for giving me plenty of advice and useful hacks on X-ray data reduction and spectral fitting, without which it would have taken me years to master those skills by myself.
A very special thanks is due to one of my best friends, former classmate, future co-author and fellow Ph.D. student, Alessia Tortosa. She encouraged me to apply for the program and helped me through many obstacles along the way. Even though we did our Ph.D. programs in two different institutions, I like to think we were in this together.
I also acknowledge the two referees of this thesis, Prof. Christian Vignali and Prof. Fabio La Franca, for very useful notes and suggestions that significantly improved the quality of this dissertation.
Last but not least, many fellow Ph.D. students and young researchers must be thanked for both scientific and moral support during these three years. Strictly in alphabetical order by last name, my gratitude goes to Filippo Ambrosino, Stefano Ascenzi, Claudio Casentini, Elia Chiaraluce, Emiliano De Santis, Alessandro Di Marco, Andrea Guerrieri, Simone Lotti, Riccardo Middei, Ilaria Nardecchia, Ornella Juliana Piccinni, Luis Diego Pinto, Fulvia Pucci, Maria Concetta Tringali, Alessandro Ursi and Giustina Vietri.